Delft University of Technology | Universitas Diponegoro

Wave-Driven Set-Up of Fluid Mud

Demak, Indonesia

R. M. Borsje

TU Delft

FAKULTAS
PERIKANAN DAN ILMU KELAUTAN
UNIVERSITAS DIPONEGORO

Wave-Driven Set-Up of Fluid Mud

Demak, Indonesia

by

Ruben Maarten Borsje

to obtain the degree of Master of Science at Delft University of Technology,
in collaboration with Universitas Diponegoro,
to be defended publicly on Tuesday July 25, 2019 at 16:00.

Date:	16-07-2019			
Student number:	4294726			
Thesis committee:	Prof. dr. ir.	A. J. H. M. Reniers,	TU Delft,	chair
	Prof. dr. ir.	J. C. Winterwerp,	TU Delft	
	Dr.	D. S. van Maren,	TU Delft,	supervisor
	Dr. ir.	M. A. de Schipper,	TU Delft	
	Ir.	S. A. J. Tas,	TU Delft,	supervisor

TU Delft

UNIVERSITAS DIPONEGORO SEMARANG

FAKULTAS
PERIKANAN DAN ILMU KELAUTAN
UNIVERSITAS DIPONEGORO

... van ’t prachtig rijk van INSULINDE dat zich daar slingert om den evenaar,
als een gordel van smaragd ...

— *Multatuli, 1860*

Acknowledgements

The work in this thesis forms the end of my 6-year journey at Delft University of Technology. Ever since I was a young, I have been fascinated by the power of the sea. Whenever we were at the beach when I was a little boy, I could always be found on the edge of the water with my shovel, creating some form of 'Dutch heritage'. It is not a huge surprise that this little boy has grown up to be graduating as a coastal engineer.

During my years of study, I have had the opportunity to experience and see more of the world than I could have ever imagined when setting my first steps in the streets of Delft. I have travelled twice to Indonesia for research and spent 5 months in Nigeria for an internship. These experiences have taught me a lot about myself and the kind of person I want to be. I have also been lucky enough to be able to graduate on a topic that kept fascinating me during the time I was working on it. It wasn't only very challenging and encompassing various aspects of research (fieldwork to data analysis to numerical modelling), it was also societally engaged - I have been able to make a contribution to research that will hopefully increase the coastal safety along a large stretch of densely populated coastline in Asia. The process has not always been easy; finding out that a lot of data isn't usable is a bitter pill to swallow, especially after having worked so hard to collect it. However, I particularly liked the modelling work afterwards, as this enabled me to develop my own ideas about the problem and to make the research really my own.

It would not have been possible for me to complete this project without the help that so many people were kind enough to provide. I would like to thank Han Winterwerp for giving me the opportunity almost 2 years ago to travel to Indonesia for the first time and for inviting me back to the project last year, allowing me to travel to this beautiful country once more. I would also like to thank Bas van Maren for the great ideas following from our brainstorm sessions during the preparation for my field campaign, for the ever critical eye on my (written) work and for the amazing stories he had to tell. Furthermore, I owe huge thanks to Ad Reniers, who has spent literally hours working with me on some derivations and on the conceptional models, as ever with so much patience. I would like to thank Matthieu de Schipper for providing me with the echosounders and for being of so much help during my data analysis. I am also very grateful to Silke Tas. She has seen me on an almost daily basis during the period I was working on my thesis, either to spar about some strange anomaly in the data, a new step in my modelling work, or just because I was craving a cup of coffee. The hours of data processing, modelling and writing have been made so much more enjoyable by my office-mates Ascha, Said, Tolga, Lennard and Remy. The same goes for all the other colleagues on the 2nd floor and in the Waterlab.

The fieldwork in Indonesia is an experience I will never forget. I would like to thank Ibu Tita, vice dean of the Faculty of Fisheries and Marine Sciences of Universitas Diponegoro, who invited me to the university, took care of all official paperwork and essentially made it possible for me to travel to Indonesia. I would like to thank my fellow 'Mangrovers' Alejandra and Celine, who have made the whole Indonesian experience so much fun. They have been a true support in times during which things didn't go as planned and the fieldwork became a real challenge. So many other people have helped me to perform my research during the field campaign, but my most sincere gratitude goes to Pak Slamat and his family. Not once, but twice now, they have taken me into their home and cared for me like a son. I am glad to have made so many happy memories - from having a laugh about my clumsiness whilst climbing into the boats, to having Pak Slamat helping me to write down my data whilst I was submerged up to my shoulders, from receiving my own *sarung* (a classical piece of clothing for Javanese males) to joining the family in the blessing of their new-born kin. *Terima kasih*; you will be in my heart forever.

During the last 6 years, there have been friends who I could always depend on and who stayed at my side no matter how dark the tidings got. I can't possibly name all of you who have supported me in some little or less little way, but I want to say thank you nonetheless. Some people, however, deserve

a special mention. Christa, Michael and Jarl, if it weren't for you, I don't even know where I would be right now. My gratitude is beyond words. Tessa, you have shown me how large a heart can be and for that I am very thankful as well.

I couldn't be more grateful to my parents and sister, whose love is unconditional and who have always supported me, no matter what. You are amazing; thank so much for always being there for me. And last but not least Lisa, who has really pulled me through the last couple of months, cheered me on, and forced me to believe in myself every day again. Thanks for stepping up to me in that hostel in Chiang Mai and for becoming such a big part of my life.

R. M. Borsje
Delft, July 2019

Abstract

Demak is a regency within the province of Central Java, Indonesia, with a mud-mangrove coast bordering the Java Sea. The region is facing a rapid retreat of the coastline, at some places as high as 1.5 km, threatening the livelihood of a large part of the population. The main cause of the erosion is the deforestation of the green belt of mangroves for the purpose of building fishponds. This has disturbed the delicate sediment balance in the area drastically. This MSc thesis was carried out within BioManCO. This is a project of Delft University of Technology and Universitas Diponegoro and aims to develop a bio-morphodynamic model for mangrove-mud coasts. This will eventually be used to identify the conditions under which autonomous reforestation of a sustainable mangrove green belt will take place, restoring the natural coastal protection. Semi-permeable dams are already being implemented to restore the sediment balance in the area. In this approach, however, the existence of a fluid mud layer is neglected. The observation of relatively steep slopes of the interface between mud and water indicates potential mud transport within the mud layer. Such a transport would contribute to the shoreward flux of sediment and thus to the restoration of the coastal profile. If a hybrid dam is implemented, it will block the flow of sediment and might therefore defy its own purpose; attenuating flow and waves in order to capture sediment and restore the eroded coastal profile.

The objective of this thesis is to assess wave damping as a driving mechanism for set-up of the fluid mud layer at the coast of Demak and to identify under what conditions such a set-up can exist. From literature it is well known that significant attenuation of waves is achieved by viscous dissipation of wave energy in the mud layer. In wave direction, this leads to a negative gradient in radiation stresses. A set-up of the fluid mud interface is hypothesised to be balancing the wave force resulting from this gradient. To gain insight in the damping of waves and, more generally, in the dynamics of the coastal system of Demak, a field campaign has been carried out. Based on these measurements a SWAN-Mud model has been set up and has been coupled to an idealised model that calculates the equilibrium slope based on modelled wave-damping.

The field observations show that the interface level is indeed sloping upwards towards the coast. This slope, however, does not seem to change significantly during the field campaign, indicating that the occurring waves are not able to move the layer. The measured wave damping over the mud flat is in the order of 30%. A strong daily variation in wave height and period, dependent on the prevailing wind system, is observed. This thesis shows, that SWAN-Mud is able to reproduce these measurements convincingly, even with the simple schematisation used in this thesis. The damping of the waves is influenced by the water depth and the wave period, and to a lesser extent by the wave height. It is also strongly dependent on the thickness and viscosity of the mud layer. A thinner mud layer with a higher viscosity will yield a higher damping rate. The use of a fluid mud module to model the dissipation of waves at the coast of Demak is proven to be necessary. Using a simpler approach to model this attenuation, like an increased bottom friction coefficient, does not yield a convincing reproduction of the results of the field campaign.

Two conceptual models have been developed to assess the possibility of a wave-driven slope: A Simple Balance Model, assuming a balance between the radiation stress in the mud layer and a pressure gradient due to a set-up of the fluid mud interface, and a Two-Layer Model, adding the influence of the water layer above the fluid mud layer to this balance. The first model shows that waves are able to force positive slopes in shoreward direction. However, for the range of mud parameters, water depths and wave characteristics as measured in Demak, these calculated slopes are too mild in comparison with the observed slopes. The formulation of the second model shows that positive slopes are not possible when a set-up of the free surface level occurs. Therefore, they may only be present over limited longshore distances, allowing water to flow away transversely, hence a gradient in the free surface level will not occur.

The adopted approach neglects the yield stress in the fluid mud layer. This thesis, however, shows that the non-Newtonian character of mud needs to be taken into account. The yield strength prevents small waves from mobilising the layer. Also, slopes as observed in the field could possibly be sustained due to a balance between this yield strength and gravity. Furthermore, accelerated consolidation of the mud layer may occur. Wave action partially destroys the flocs of which the fluid mud layer consists, which facilitates a faster outflow of water, hence a faster consolidation. The yield stress may therefore increase over time. This leads to a stronger mud layer capable of maintaining the observed slopes. This could even lead to a build-up of sediment against the coast which could potentially be colonised by mangrove species. The accumulated sediment is thereby fixated as a build-out of the coastline.

The methods used in this thesis need more refining and need to be validated to an appropriate data set. The validation of the determination of the radiation stress within the fluid mud layer is of particular interest. It forms a crucial step in determining the set-up of the mud layer and not much research into this topic has been carried out as of yet. Also, more hydrodynamic data is needed to gain a better understanding in the processes governing the flow in these mud layers, as well as a better characterisation of the mud properties in the area. An interesting further development of SWAN-Mud could be to couple this wave model and its fluid mud module with Delft3D. In this way, the mud layer dynamics due to waves can be linked to flow and changes in morphology.

Nonetheless, this thesis shows a possible implication for the management of the coastal area of Demak. The hybrid dams might indeed be blocking a restoration mechanism of the mud coast which defies the original purpose of building these dams. A build-up of sediment may occur in front of the dams due to the wave-driven transport within the fluid mud layer, eventually blocking flow through the dams. The suggested flow patterns in front of and along the dams may be complicated and could even erode this accumulated sediment, effectively diminishing the restoration mechanism to a minimum.

Contents

1 Introduction

1.1. The eroding coast of Demak

Demak is a regency within the province of Central Java, Indonesia. It is located at the north coast of Java, bordering the Java Sea, (figure 1.1). The region is facing a rapid retreat of the coastline, threatening the livelihood of a large part of the population.

1.1.1. Mud Coast

The Java Sea is a narrow shelf sea, situated on the Sunda shelf. The tide is mainly diurnal, with a small semi-diurnal component (Smits, 2016; Winterwerp et al., 2014). It propagates counter-clockwise through the Java Sea (Smits, 2016). It is a micro-tidal coast, the tidal range varies from 0.4 to 0.6 m over the neap-spring cycle. The wind system is dominated by the monsoon; from May to September the south-eastern (SE) monsoon occurs, from October to April the north-western (NW), which is also referred as the storm season (Winterwerp et al., 2014). The wet season largely coincides with the NW monsoon and the run-off of the rivers is thus much larger. As the wind is directed towards land during this season, this fresh water of the rivers is pushed against the coast, causing gravitational circulations (Winterwerp et al., 2014). Another important wind system that plays a role locally is the sea breeze. This breeze forms in quiet atmospheric conditions during the day, when the air above land heats up faster than the air above the sea. This differential heating induces a horizontal pressure gradient from an area of high pressure above sea to a low pressure above land; the wind towards land that is generated because of this pressure gradient is called the sea breeze (Kimble, 1946). The wave climate is strongly related to the prevailing monsoon and according to Tas (priv. comm. 2018) this climate can be characterised as presented in table 1.1. These wave conditions are representative for average, day-to-day conditions. According to Tas (priv. comm. 2018), however, extreme conditions also play a significant role in the dynamics of the coastal system.

Figure 1.1: The island of Java, Indonesia, on which the coastal area of Demak is indicated with the cyan rectangle. Satellite images retrieved from Google (2017).

Wave parameter	Unit	NW Monsoon	SE Monsoon	Sea Breeze
Significant wave height	m	0.72	0.16	0.24
Peak wave period	s	5.7	1.6	2.7
Peak wave direction	°	317	133	351

Table 1.1: Average wave conditions for each climate. Data from Tas (priv. comm. 2018).

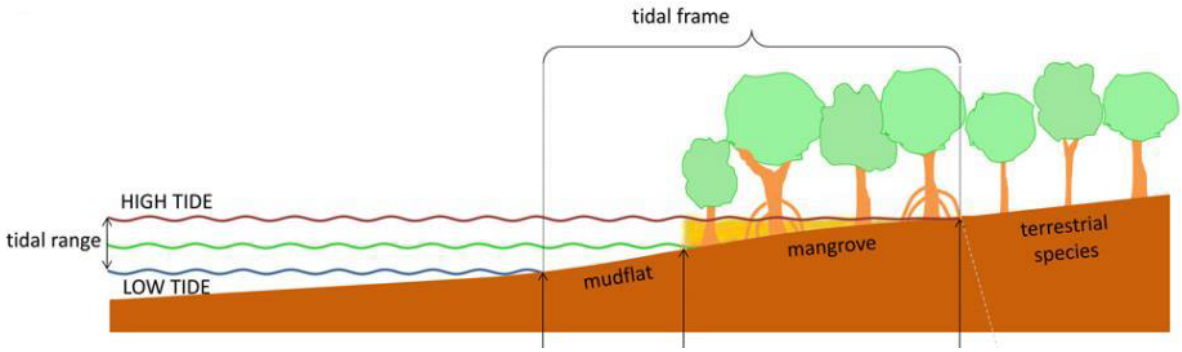

Figure 1.2: Simplified configuration of a typical mangrove forest. From Smits (2016).

The northern Javanese coast can be described as a mud coast. Due to the low energetic hydrodynamic conditions, fine sediment has been able to accumulate, forming very gentle slopes of about 1:1000 to 1:1500, shaped in a convex-up profile (Van Prooijen et al., 2017). Due to this very shallow foreshore, long-shore tidal currents are generally small, which means that tidal filling happens predominantly in a cross-shore direction. Also, due to the rheological properties of the mud (section 2.1.2), strong wave damping occurs by means of dissipation of wave energy in the viscous mud layer (Jaramillo et al., 2009; Kranenburg et al., 2011; Sheremet and Stone, 2003; Winterwerp et al., 2007, 2012). In combination with the coastal profile, this results in very little wave breaking. As wave breaking is almost absent, so is a long-shore wave driven current, resulting in a cross-shore directed path of the sediment particles in the water column (Van Prooijen et al., 2017; Smits, 2016). Furthermore, due to this long, shallow foreshore, waves have a lot of opportunity to refract. This reduces the possibility of a long-shore current, as occurrence and magnitude of this current is directly related to the angle of the waves with the shore-normal (Van Prooijen et al., 2017).

At many of these mud-coasts, mangrove ecosystems can be found. Mangroves mostly grow in the areas which are above mean sea level and are being flooded for about 30% of the time (Smits, 2016); the intertidal flats (figure 1.2). The level of salinity is key to the survival of the ecosystem. Although mangroves are better adapted to living in salty conditions than their competition and are thus out-competing them, salinity in itself is not favourable for their growth. Therefore, the fresh-water input from creeks and rivers is very important for the ecosystem, as this keeps the salinity at a tolerable level (Tonneijck et al., 2015).

A healthy mangrove-mud system is in dynamic equilibrium. This means that the system is naturally eroding or accreting, depending on waves and tidal action, and that the state of the system varies over the years. The nett effect of this erosion and accretion at a certain moment in time however, is in most systems stable (Winterwerp et al., 2014). The sources of incoming sediment are the rivers and the fine sediment that is eroded from the foreshore, mostly by larger waves. The fine sediment is transported to the coast by tidal flow. The outflux of sediment is also due to wave action. The waves stir up the sediment at the sea bed, after which it is mixed further into the water column and transported away by the dominant currents (Van Prooijen et al., 2017; Smits, 2016; Winterwerp et al., 2014) (upper panels of figure 1.3). The balance between inflow and outflow of sediment is very delicate. The nett effect is only a small difference between two large fluxes, hence a small disturbance in one of these fluxes can have a significant effect on the system (Van Prooijen et al., 2017). It is thought that the mangrove

ecosystem balances this inherently unstable system.

The mangroves contribute to this stability in a number of ways. Firstly, the mangroves reduce the hydrodynamic load on the system. The complex root systems and stems of the mangroves create drag on the flow, which means a reduction of wave energy and thus a reduction of wave impact (Smits, 2016). Secondly, the mangroves increase the resistance of the mud against erosion. The root systems, as well as dead roots that have remained in the soil, strengthen the mud; in other words, the critical bed shear stress is increased (Smits, 2016). Lastly, the mangroves enhance sedimentation of fine particles. Due to the wave attenuation, as well as the reduced flow velocities, the fine sediment is allowed to settle more easily. Furthermore, the growth of sub-surface roots causes the volume of the soil to increase, hence pushing up the surface level.

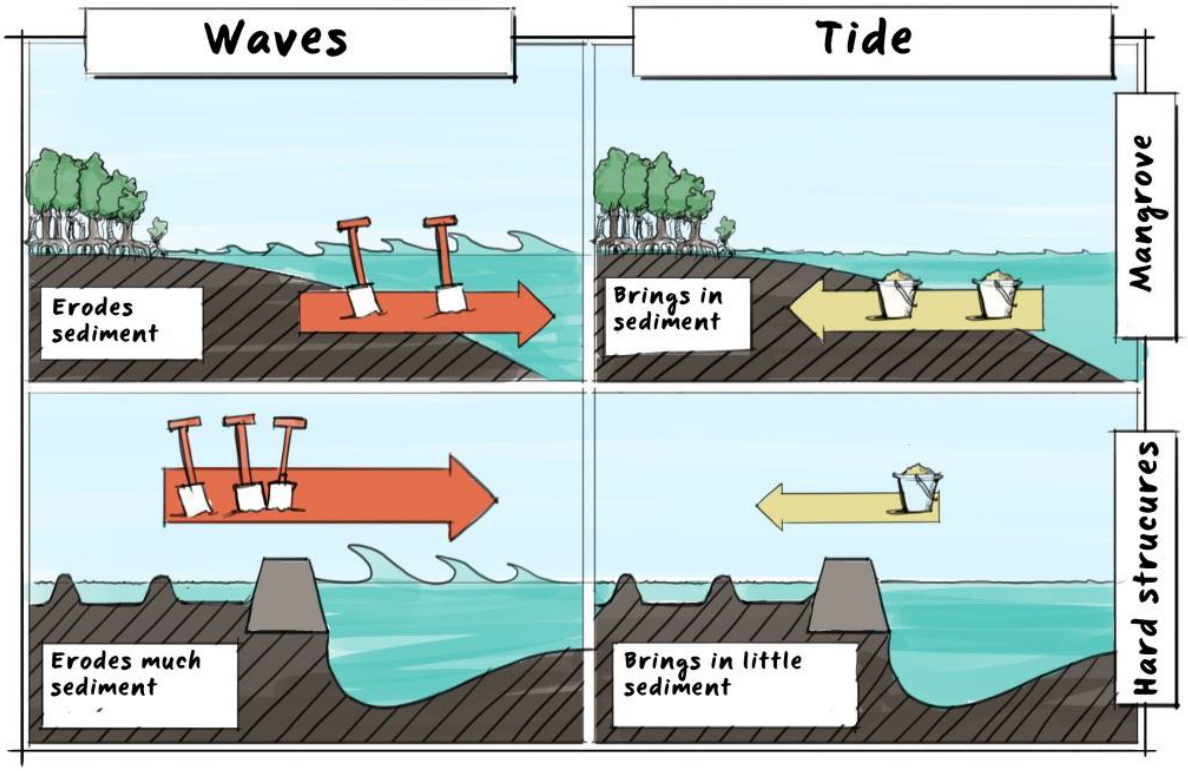

Figure 1.3: Illustration of the sedimentation and erosion processes in a mangrove-mud system. From Winterwerp et al. (2014)

1.1.2. Erosion

The erosion problems in the coastal area of Demak are severe. Between 2003 and 2012, the coastline retreated roughly 800 to 1500 m (figure 1.4) and from 2012 until 2019, these figures have only increased. The causes of this erosion are mainly anthropogenic. Until the 1960s, the coastal area was protected by a broad mangrove green belt. The prime driver of the economy of Demak at that time was agriculture. In the 60s, channels were dug and many natural creeks were straightened in order to extend and optimise the rice-farming in the area. When the demand for shrimp increased explosively in the 1980s and the price of rice on the world market decreased, many of the rice paddies were converted to fish ponds throughout the following two decades. These fish ponds, however, were not farmed sustainably and, in order to survive, farmers had to open new fish ponds in the mangrove green belt. This practice continues to date, reducing the mangrove ecosystem to a very narrow zone (if not entirely non-existent) along the coast (Tonneijck et al., 2015).

The large decrease in area of the forest means a decrease in the tidal prism of the mangrove forest as well (Winterwerp et al., 2013). As a reduced tidal prism also means reduced tidal velocities, the

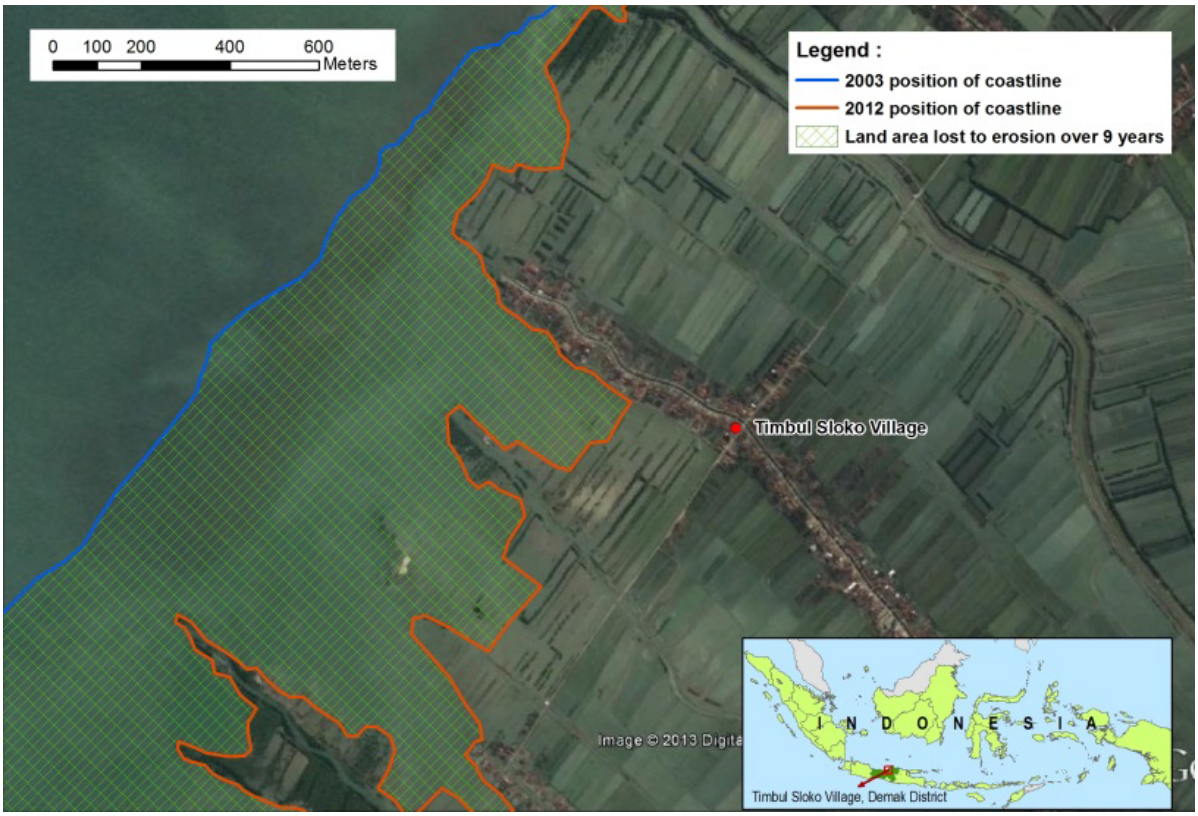

Figure 1.4: Example of coastal erosion in Demak district near Timbul Sloko village, illustrated through the coastline in 2003 (blue) and in 2012 (orange). From Tonneijck et al. (2015).

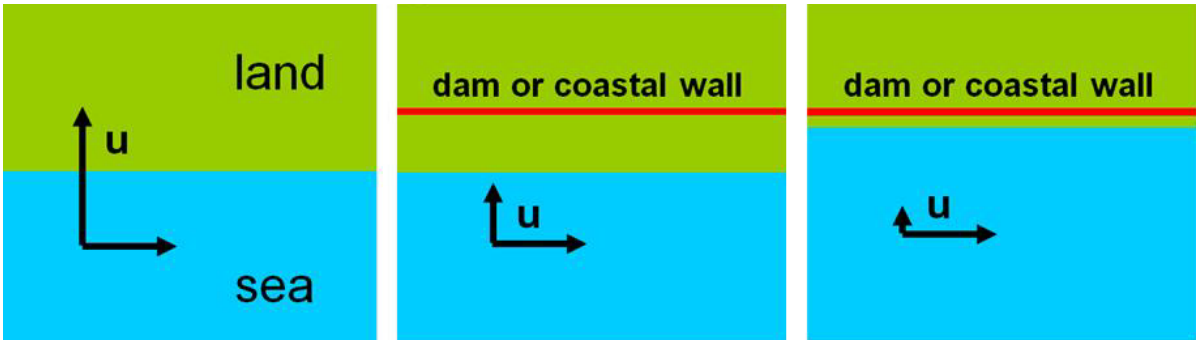

Figure 1.5: Due to the construction of fish ponds, the tidal prism decreases and therefore also the sediment flux into the forest, denoted in the figure by u. The length of the arrows suggests the magnitude of the flux. Adapted from Van Prooijen et al. (2017)

sediment transport capacity of the tide decreases due to the removal of forests and, with that, the sediment influx into the forest decreases as well (figure 1.5). Furthermore, due to the construction of the fish ponds and due to the aforementioned straightening of the creeks, many creeks have lost their connection to the floodplains. This reduces the sediment input into the system as well. Another effect stemming from this development is that some parts of the mangrove forests have become disconnected from their alluvial input. This increases the salinity levels in the mangrove habitat.

Another part of the problem is the bunds around the fish ponds and, more generally, any hard alongshore coastal protection. These structures reflect the incoming waves, which can result in a doubling of the significant wave height in front of the structures (Van Prooijen et al., 2017). As the forcing of the erosion scales quadratically with the significant wave height, this forcing increases drastically as well.

The combination of an increase in forcing and a decrease in sediment supply leads to a negative sediment balance, resulting in coastal retreat (figure 1.3). The initial convex-up profile of the foreshore reduces to a concave-up profile, which leads to even more mangrove habitat loss and to a decrease in the attenuation of waves, or, in other words, an increase in forcing (Van Prooijen et al., 2017; Winterwerp et al., 2013). The reflection of the waves and the reduction of sediment input also assists in the development of scour holes in front of the structures, which eventually leads to the structures toppling over and failing. This process is only made worse by the rheological properties of the mud; the muddy bottom does not have much strength and it liquefies quite easily (Van Prooijen et al., 2017). The failure of such a structure means the inundation of yet another large patch of land. It can thus be concluded that the reduction of the mangrove forest has lead to a self-accelerating erosion process (Winterwerp et al., 2013).

Another mayor contributor to the retreat of the Demak coastline is land subsidence (Winterwerp et al., 2014). This is predominantly caused by the groundwater withdrawal in and around Semarang for drinking water and for the industries. In combination with sea level rise, this will make the Demak coastal area increasingly more vulnerable to flooding in the future.

1.1.3. Solution

As mentioned in section 1.1.2, traditional hard engineering solutions have proven to not be very successful at the coast of Demak. Therefore, a 'hybrid engineering' solution is now being implemented. The most ideal solution would be the restoration of the mangrove green belt. In order for a healthy mangrove forest to grow and even autonomously re-colonise the area, the coastal profile should be shaped convex-up in the direction of the coast. The key to re-establishing a stable coast and thus such a profile, is the restoration of the sediment balance. Therefore, the loss of sediment by waves should be reduced, which can be achieved by placing semi-permeable structures parallel to the coastline at some distance from the shore. These 'hybrid dams' mimic the complex root system of the mangroves. They therefore do not reflect waves like hard structures and let water and sediment pass. During the transmission of waves through a hybrid dam such as this, the wave energy is reduced and so is the wave height behind the structure (Winterwerp et al., 2013) (figure 1.6). The additional effect is that behind the dams, a calm area is created in which the sediment brought in by the tide and rivers can settle more easily, making these areas re-colonisable for mangroves.

The effects of these interventions on the system, however, are poorly understood. The aim of the project of which this thesis is a part, BioManCO, is to develop a bio-morphodynamic model for mangrove-mud coasts, with input from laboratory and field work. BioManCO is a project of Delft University of Technology, in collaboration with Universitas Diponegoro, funded by NWO. The developed model will be used to assess the transition from a stable convex-up cross sectional profile towards an eroding concave-up profile as described in section 1.1.2 to gain more insight in the governing processes of the erosion. Next, the model will be used to identify the conditions under which restoration of the sediment balance may lead to the restoration of a sustainable mangrove green belt. The model will be utilised for developing generic design rules for coastal restoration. These rules will be tested by designing a Master Plan program in Demak, analysing a variety of alternative scenarios regarding biodiversity and connectivity to the hinterland.

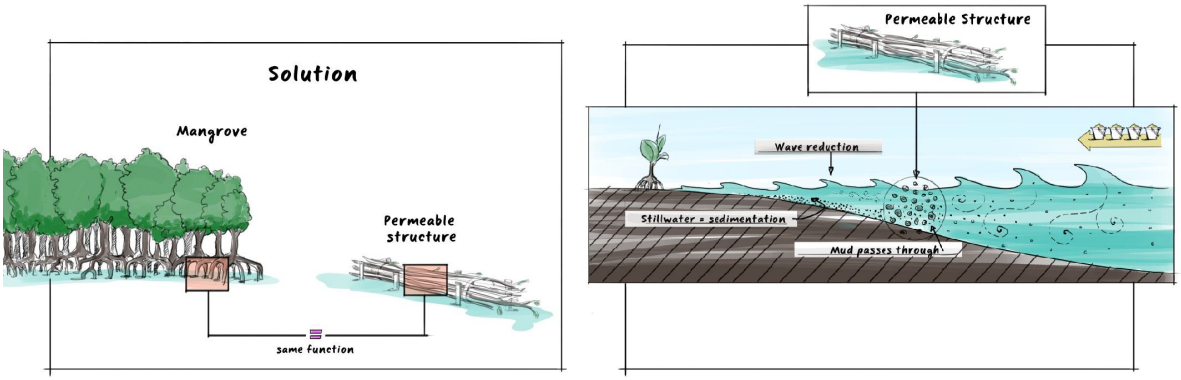

Figure 1.6: Cartoon which shows the basic principles of the hybrid engineering now implemented in the Demak coastal area. Adapted from Winterwerp et al. (2014).

Key to this project is the input of knowledge acquired in the field. Unfortunately, the coastal region of Demak is a very data-scarce area, which means that validating model results is difficult. As also follows from literature, not much is known yet about the interaction between the muddy substrate and the hydrodynamics in this area. Understanding this complicated behaviour is important for the project, as the proposed Master Plan is to provide for a long-term solution for the severe erosion.

1.1.4. Fluid Mud Layer

As stated in section 1.1.2, the coast of Northern Java is a mud coast. This means that the soil consists of clay and silt sized particles. A more elaborate description is given in chapter 2, but for the purpose of defining the research objective in section 1.2, some necessary information is presented here. The mud-water system can be characterised according to Mehta et al. (1994) as follows. The upper layer consists of a water-mud suspension. A lutocline (a sharp density gradient), separates this water layer from the layer of fluid mud. The fluid mud layer typically has concentrations in order of tens to hundreds of g/L and bulk densities between 1080 and 1200 kg/m^3. Settling of this high concentration suspension is hindered by the proximity of other fine sediment grains and flocs, however an interconnected matrix strong enough to eliminate movement has not yet been formed (McAnally et al., 2007). Under this layer of fluid mud, a consolidating/consolidated mud bed is present.

The thickness of the fluid mud layer at the coast of Demak has been observed by Winterwerp (priv. comm. 2018) to range from the order of centimetres to the order 1.5 m, depending on the location. Also, at some locations, the thickness of the mud layer seems to increase in landward direction. As the solid bed underneath the fluid mud only has a very mild slope, this increase in thickness is likely to indicate a slope in the water-mud interface in cross-shore direction, much like the well-known water level set-up at sandy coasts. The slope observed at the mud coast of Demak, however, is much larger, i.e. a change in thickness of about 1 m over a 200 m transect.

According to Rodriguez and Mehta (1998), this set-up of the mud layer can be linked to the dissipation of wave energy due to the transfer of momentum from water to mud layer. The viscous dissipation of wave energy under non-breaking waves causes a reduction in wave energy in the direction of the coast. As wave-induced radiation stress is proportional to wave energy, the radiation stress will decrease in cross-shore direction as well. This gradient in radiation stress is equivalent to a force in landward direction and can as such be an explanation of the measured set up of the mud-water interface. If, however, this set-up cannot occur, i.e. the shoreward flux in momentum is not balanced by a shore-supported hydraulic head, the mean forces must be balanced by a bottom shear stress, implying the presence of a mean current. Considering the high concentration of the mud layer, this could potentially mean a large sediment flux in shoreward direction, until the shore prevents further movement of the mud and a set-up will build in that direction (Rodriguez, 1997). It is unclear to what extent these effects are present at the Demak coast and how these vary with changing wave conditions.

As described in section 1.1.3, the proposed solution for the coastal erosion in the Demak area involves building hybrid dams that capture the fine sediment as described in section 1.1.2. However, this approach assumes that transport of fine sediment in suspension and settling of this sediment is the main driving mechanism for sedimentation of mud. The existence of a fluid mud layer is completely neglected in this approach. If the set-up in this layer is indeed driven by waves and thus a wave-mean current that transports mud towards the coast exists, a hybrid dam would work completely against the purpose for which it was build in the first place. To make well-informed decisions as to where and in what form to implement these dams, or even whether to implement them at all, more information on the potential mud transport within the fluid mud layer is needed. A major step forward in this decision-making process would be to be able to predict where this transport might occur on the basis of measurements of wave damping or slopes of the fluid mud layer interface. The time-scales on which these processes play a significant role are important as well for the design of these dams.

1.2. Research Objective and Research Questions

The objective of this thesis is to assess wave damping as a driving mechanism for set-up of the fluid mud layer at the coast of Demak and to identify under what conditions such a set-up can exist. The following research question can be associated with the research objective of this thesis;

Can wave action generate a cross-shore gradient in the interface between water and fluid mud?

To be able to provide an answer for this question, several sub-questions have been formulated;

- *What are the characteristic hydrodynamics on a timescale of days/weeks?*
- *What is the effect of the fluid mud layer on the waves?*
- *What are the dynamics of the fluid mud on a timescale of days/weeks?*
- *What are the long-term wave effects on fluid mud dynamics on a timescale of months/years?*

1.3. Approach

To this end, a field campaign will be carried out in the coastal area of Demak to measure the dynamics of the system, especially the wave damping over the fluid mud layer. Consecutively, based on these measurements, a SWAN-Mud model will be set up and will be coupled to an idealised model that calculates the slope of the interface between the fluid mud layer and the water layer, based on the modelled wave-damping.

2

Literature Study

The research objective and research questions (section 1.2) touch on a variety of subjects, both directly and indirectly. As the range is quite large, it is important to establish a basic understanding of all of these topics, which is why this chapter elaborates on the most important of them. Section 2.1 presents some characteristics of mud and, more specifically, of fluid mud as well as the known effect of mud on the damping of waves. Section 2.2 describes how this damping has been modelled up until now. This process of damping initiates other effects on the system as well, which are described in section 2.3. Section 2.4 finally presents three hypotheses for the wave damping as driving mechanism behind the slope of the fluid mud interface.

2.1. Mud Characteristics

Mud is a mixture of water, soil and a most of the time, a significant amount of organic matter. Particles sizes are smaller than 63 μm, which is the upper limit for 'silt', and a significant part of these particles is smaller than 2 μm, which is the upper limit for 'clay'. Mud has certain cohesive properties, which can be attributed to the clay particles, as these exert electro-chemical forces in an aqueous environment (De Wit, 1995). When collision brings particles close enough for the attractive forces between the particles to overcome the repulsive forces, the particles bond and form so-called flocs. This process is called aggregation. Fluid mud, for example, consists of a dense suspension of these flocs (McAnally et al., 2007). The formation of flocs also has an influence on the settling of the sediment; in the first stages, it increases the settling velocity. At a certain point, however, when the concentration of the mud-water suspension has become too high, the settling of particles and flocs is hindered by the proximity of other flocs and particles. For these concentrations, the settling velocity decreases (figure 2.1). The interface between the hindered settling zone and the water column above is often marked by a steep increase in density. This is called a lutocline (Van Prooijen et al., 2017).
When this highly dense suspension is left at rest, consolidation will take place. The suspension will form a gel in which the water bears the load. During the consolidation, water will slowly drain out from between the particles. Therefore, when the bed further consolidates, the mud skeleton will start to bear the load and a bed will form (Van Prooijen et al., 2017).

2.1.1. Rheology

The rheology of mud describes the deformation of mud and the flow of matter forced by external loading. This behaviour is complex and not fully understood. Foda et al. (1993) argue that these cohesive muds show non-linear behaviour and that their rheological properties, when forced by waves, are a function of the applied strain. Foda et al. (1993) furthermore state that clay muds behave like elastic solids at low oscillatory strains and like viscous fluids at high strains. They propose the following classification of behaviour, which can be explained further based on the interactions between the clay particles according to De Wit (1995);

Elastic When the strain amplitude is smaller than a certain critical strain amplitude γ_e, the mud can be completely described as an elastic solid. The strain is not enough at this point to break the links between the particles, hence the structure merely deforms.

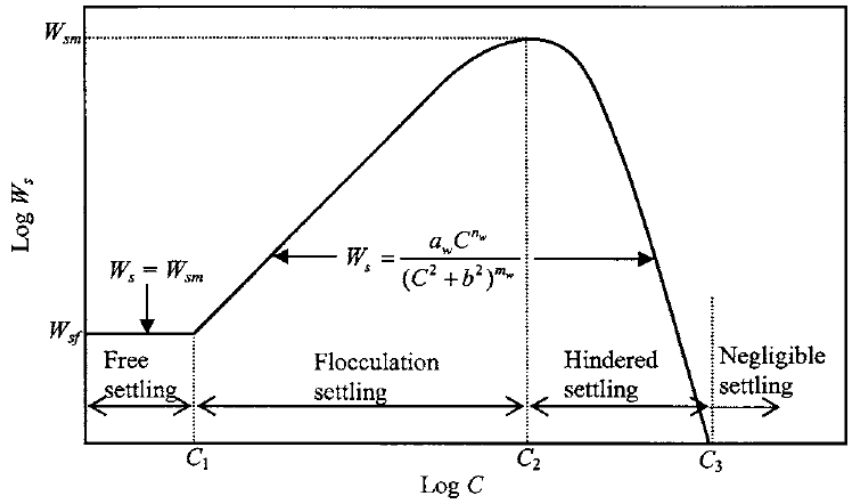

Figure 2.1: Schematic overview of average suspension settling velocity, w_s, versus concentration, c. From McAnally et al. (2007).

Viscoelastic For intermediate strain amplitudes, some bonds between the particles will break, starting with the weakest. The mud therefore shows both viscous and elastic behaviour.

Viscous At the highest strain amplitudes, the sediment can be modelled like a purely viscous fluid. Most particle bonds have been broken up at that level of strain.

The shear modulus of a material is defined as the ratio between the shear stress and the shear strain within a material, $G = \tau/\gamma_s$, and thus describes the material's response to shear stress. If there is a phase-shift between the shear strain applied to the material, γ_s, and the resulting shear stress, τ, then the shear modulus of that material is complex; $G = G' - iG''$. The real part of the shear modulus, G', represents the elastic shear storage modulus and the imaginary part, $-G''$, the viscous shear loss modulus. For purely elastic behaviour, $G'' = 0$ and there is no phase-shift between strain and shear stress. A completely viscous response is achieved when the phase shift is $\pi/2$ and in that case, $G' = 0$. Equivalently, this can be described using a complex viscosity; $\nu = \tau/(\rho\dot{\gamma_s}) = (G'' + iG')/\rho\omega$ (with $\dot{\gamma}$ the shear rate, ω the wave angular frequency and ρ the density).

As the rheological behaviour of mud changes depending on the level of strain, it can thus be characterised on the basis of the shear storage modulus and the shear loss modulus (figure 2.2). For low levels of strain, the shear loss modulus is zero and the behaviour is elastic. For intermediate levels of strain, the both shear storage and loss modulus are non-zero, hence the behaviour is visco-elastic. For even higher levels of strain, the shear storage modulus goes to zero, so the behaviour becomes purely viscous. The transition from elastic to visco-elastic behaviour is dependent on the solid concentration and occurs for a higher critical strain amplitude γ_e if the solid concentration in the mud suspension is higher (Foda et al., 1993; De Wit, 1995). McAnally et al. (2007) states that this behaviour is also dependent on the frequency of the applied oscillatory strain.

A purely Newtonian fluid is characterised by shear stresses that are linearly proportional to the applied strain. Furthermore, the viscosity is independent of stresses in the fluid. Both these conditions do not hold for mud. For example, under some circumstances a finite initial stress is required to initiate movement of mud, a yield stress τ_y. This behaviour can be described with a visco-plastic model like the Bingham model (equivalent to the Herschel-Bulkley model in equation (2.1) with $n = 1$). McAnally et al. (2007) however argue that for fluid muds, a shear-thinning or pseudo-plastic model would be more appropriate. Due to the breaking of the bonds between the mud particles at higher shear strains, a lower amount of shear stress can be sustained; the viscosity decreases under increasing shear strain. This behaviour is Non-Newtonian as it deviates from the linear proportionality between stress and strain (in the case of shear thinning; $n < 1$ in equation (2.1)).

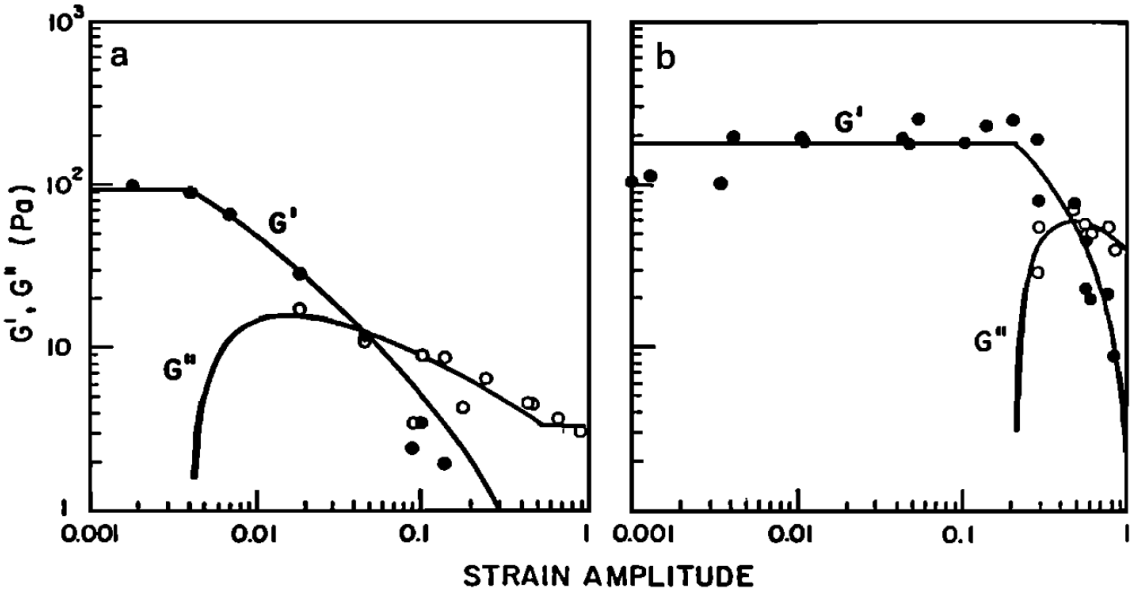

Figure 2.2: Storage Modulus G' and Loss Modulus G'' versus strain amplitude $|\gamma|$ (solid and open dots respectively). The left panel shows a clay with a 20% lower solids content than the right panel. From Foda et al. (1993).

$$\begin{cases} \dot{\gamma} = 0 & \text{for } 0 < \tau < \tau_y \\ \tau = \tau_y + K\dot{\gamma}_s{}^n & \text{for } \tau \geq \tau_y \end{cases} \tag{2.1}$$

Although the Bingham model works well for quasi-steady rotational shearing, these are not field conditions (De Wit, 1995); in the field the flow is oscillatory and therefore the visco-elastic description of the response by Foda et al. (1993) is more applicable when looking at actual field conditions.

2.1.2. Fluid mud

As the main concern of this thesis is the interaction between waves and fluid mud, in this section a more detailed description will be given of what was already mentioned in section 1.1.4.

Characteristics

A wide range of definitions for fluid mud can be found in literature. According to Winterwerp et al. (2019), 'fluid mud is a suspension or mixture of cohesive sediment at a concentration around (or a bit larger than) the gelling point'. This concentration is generally in the order of several 10 to 100 g/L. The effective stresses in the fluid mud are small or even negligible. The fluid mud exhibits highly non-Newtonian behaviour and is either stationary or mobile. It can only be stable when an external energy source is present, such as waves, horizontal pressure gradients or liquefaction by pumping water into the pores. If such an external source of energy is not present, the fluid mud will consolidate over time. Therefore, the properties of the fluid mud, such as the dry density and the viscosity, vary over the thickness of the fluid mud layer and as well as over time. Figure 2.3 shows a typical concentration profile for a high sediment load environment in which fluid mud is able to develop. According to Ross and Mehta (1989) there is a 4 to 5 order of magnitude range in concentration between the water surface and the cohesive bed. Further to Ross and Mehta (1989) and also Mehta et al. (1994), the vertical concentration profile can be defined with three characteristic regions;

Upper column mobile suspension layer: This is typically the largest layer. The layer is relatively well-mixed and is sustained by turbulent pressure gradient driven flow. Concentrations can be less than 1 g/L but may exceed 2-3 g/L in case of extreme events.

Fluid mud layer: The transition between the upper layer and the fluid mud layer is marked by a sharp lutocline. This near-bed layer has high sediment concentrations and can effectively dampen turbulent velocity fluctuations, which causes a transition towards more viscous shear flows. This

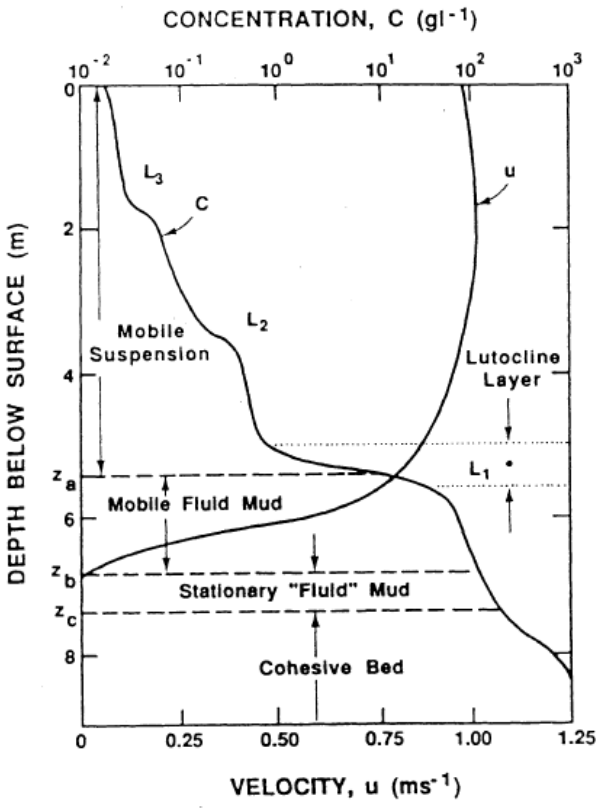

Figure 2.3: Typical concentration and velocity profile in a high concentration environment. From Ross and Mehta (1989).

relatively high damping of turbulence is due to the high viscosities in this layer; 10-100 times that of clear water.

Cohesive sediment bed: At this level, the mud starts to show porous solid properties; the concentration of sediment particles becomes sufficiently high for soil structural development.

Formation

According to Winterwerp et al. (2019), fluid mud can be formed by deposition of sediment from the water column and/or liquefaction/fluidisation of the sediment bed. Liquefaction is the collapse of the floc structure by external stresses at a constant water content. Fluidisation occurs when water is pumped into the soil.

The classical view on the formation of fluid mud (formation by liquefaction) is summarised by McAnally et al. (2007) as follows. Waves can induce pore pressure gradients in the cohesive bed, which cause flow of the pore fluid. As the wave-averaged water pore pressure increases with time, the wave-averaged effective normal stress in the soil decreases. When this is zero, the sediment bottom is fluidised; the aggregates are separated and the sediment has become fluid-supported instead of grain-supported. The soil matrix has been destroyed by the excess pore pressure. The initial response of the bed is fully elastic; the deformation is reversible. In time, however, the soil may yield, which is plastic behaviour. The soil is in that case not capable of returning to its original state any more.

Fluid mud can be formed by deposition if the sediments' consolidation rate is smaller than its deposition rate. Whether the fluid mud is actually formed is dependent on the local hydrodynamic conditions. If these are too energetic, flocs are not able to settle on the bed or will be picked up immediately after settling. Fluid mud formation by sedimentation is a common feature in habour basins, because the velocities are relatively a lot smaller than in the surrounding open waters. This mechanism, however, has also been observed in open water (Winterwerp et al., 2012). In that case, the shear flow caused

by the orbital motion of waves starts to erode mud on the seabed. At a certain point, the amount of sediment in the water column exceeds the saturation conditions. Fluid mud is then formed upon deposition of the sediment. Furthermore, due to this soft mud layer, the interface turbulence is damped, therefore the carrying capacity of the water column decreases even further. The measurements of Rogers and Holland (2009) at Cassino Beach, Brazil, as well as the detailed measurements of Jaramillo et al. (2009), Sheremet et al. (2012) and Traykovski et al. (2015) at Louisiana, United States, support this theory. The time-scales of forcing and damping do not facilitate the occurrence of liquefaction, as the time-scales of liquefaction are much to short too match the observations. Traykovski et al. (2015) also report an increase in the damping coefficient after the storm events and attributes this to the settling of the fluid mud layer.

Mud-Wave interaction

Several field experiments (Jaramillo et al., 2009; Rogers and Holland, 2009; Sheremet and Stone, 2003; Sheremet et al., 2012; Traykovski et al., 2015; Winterwerp et al., 2007, 2012)have shown that, at locations where fluid mud is present, significant wave damping also occurs.Part of the wave energy is transferred to the fluid mud layer. This generates an internal wave on the interface, whilst also inducing viscous energy dissipation within the mud layer due to the high viscosity. This results in the damping of the surface waves. Over about 3.5 km, this damping can reduce the wave height by up to 50% (Winterwerp et al., 2007) and some authors report even more. Although the effect on the wave-height is quite easy to measure, the movement of the interface between mud and water is not. Jaramillo et al. (2009) and Traykovski et al. (2015) manage to measure this lutocline, as well as the hydrodynamic bed, using acoustic backscatter. The latter also measured the velocities inside the fluid mud layer. Traykovski et al. (2015) report internal waves with an amplitude in the order of 1-10 cm. Orbital velocities of the order of 10 cm/s are reported inside the mud layer as well. Traykovski et al. (2015) also state that viscous models (some of which will be described in section 2.2.2) hold reasonably well for laminar flow of the mud layer. Most observed damping occurs after high wave events, when the fluid mud starts to settle, as hypothesised by Winterwerp et al. (2012). The decay scale of the amplitude of the surface waves then shortens drastically.

2.2. Modelling Mud-Wave interaction

Since Gade (1958), numerous authors have tried to model the mud-wave interaction as described in section 2.1.2. Most models consist of two layers; a layer of water (either inviscid or with a small viscosity) on top of a fluid mud layer. The largest differences between these models can be found in the way the rheology of the latter layer is incorporated. Some authors consider multiple layers of mud with varying rheological properties per layer to include the variability of the mud characteristic over depth as well.

2.2.1. Types of Models

According to De Wit (1995) the models describing the interaction between a muddy bed and waves can be divided into five groups, based on the implemented rheology of the mud layer;

1. Ideal elastic models
2. Poro-elastic models
3. Viscous models
4. Visco-plastic models
5. Visco-elastic models

The first two groups consider an ideal elastic bed, so no viscous behaviour is taken into account. In models in the second group, the effect of the pore water on the elastic bed has also been incorporated. As viscous effects are not considered in these models, dissipation of wave energy by the mud layer cannot be calculated and thus attenuation of the waves does not occur. The applicability of the elastic models is limited to non-fluid, highly consolidated cohesive beds, although the poro-elastic models can also be applied to relatively thin layers of unconsolidated mud.

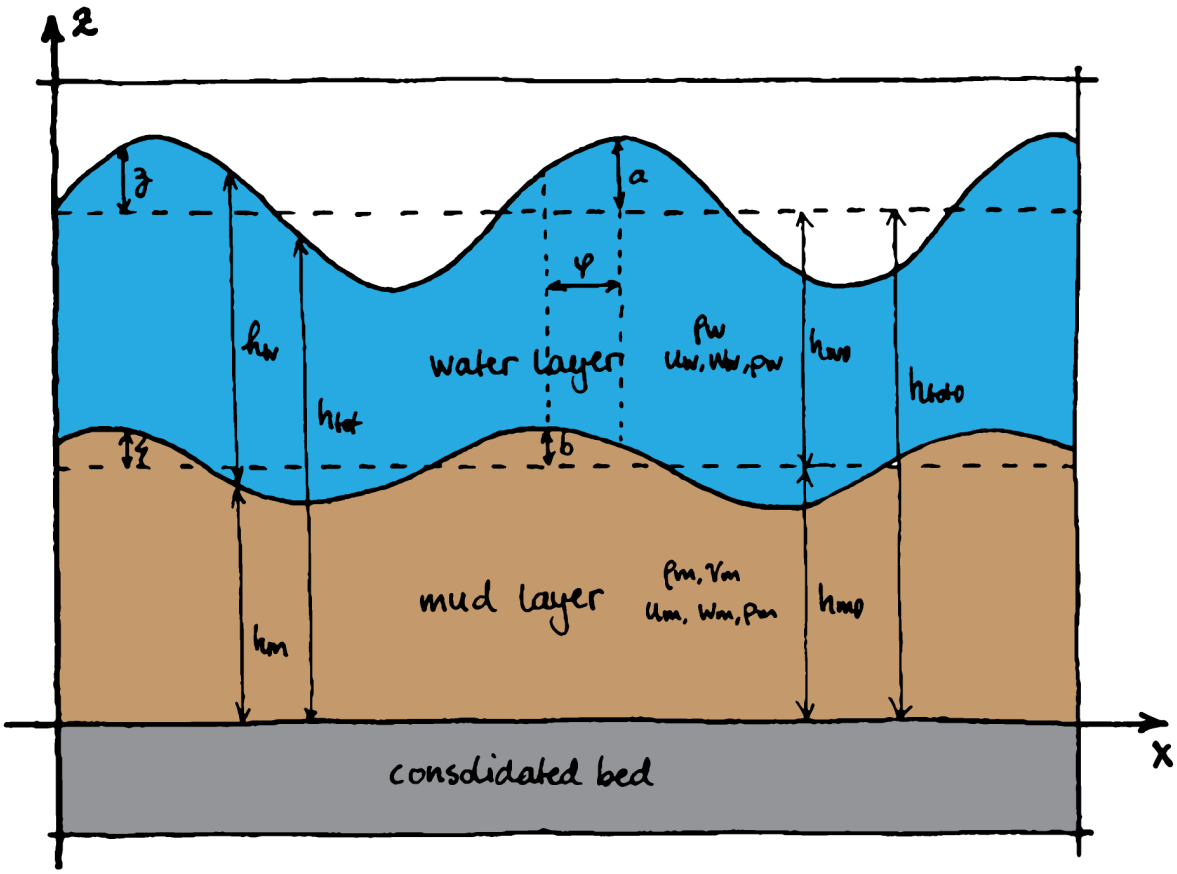

Figure 2.4: Schematic representation of the two-layer viscous fluid mud system adopted for the models described in this thesis. Adapted from Gade (1958) and Kranenburg et al. (2011).

As described in section 2.1.1, fluid mud (for which wave damping does occur) has viscous, viscoelastic and viscoplastic properties. With regard to the viscoplastic models, De Wit (1995) argues that these are not representative of the response of fluid mud to the oscillatory forcing of waves as observed in the field. That response is shown to be visco-elastic, which leads to the conclusion that it will most likely be better to represent the mechanical properties of mud with a visco-elastic model. Using this approach, however, is rather complex due to the non-linear dependency of the visco-elastic properties on depth, oscillatory strain amplitude, consolidation time and the method used to measure these properties (De Wit, 1995).

The rheological properties of the mud are only represented partly by the viscous models, as the mud is assumed to be a highly viscous Newtonian fluid. They can, however, still be used to estimate wave damping and wave-induced velocities in the mud layer. De Wit (1995) shows that for large strain amplitudes, it is acceptable to model fluid mud as a viscous fluid. The value of the storage modulus decreases faster than the loss modulus for the particular type of mud used in that specific research, and therefore the mud shows a much more viscous behaviour. An added benefit is that the viscous models are rather easy to implement.

2.2.2. Two-layer viscous fluid model

The viscous models described in the previous section are all two-layer models. The upper layer is a non- or low-viscous water layer and the lower layer consists of fluid mud. The lower layer characteristically has a much higher viscosity than the upper layer, as well as a higher density. Two viscous versions are presented in this section, one by derived by Gade (1958) and one by Kranenburg (2008), which was later implemented in the wave model SWAN, forming SWAN-Mud (Kranenburg et al., 2011).

Gade

The first attempt to model the response of a fluid mud layer under wave forcing was made by Gade (1958). A slightly modified version of the schematic representation used is given in figure 2.4. The assumptions made in deriving the mathematical model have been summarised by Kranenburg (2008) as follows;

- The wave is of sinusoidal form;
- The disturbance of the upper fluid is not associated with any driving or dissipating shearing forces;
- Motions of both fluids are considered divergence-free;
- Only plane waves are considered;
- Variations of the surface pressure are neglected;
- The mean current is assumed to be zero;
- The wave amplitude is considered to be small compared with depth;
- Fluid layers are considered to be of infinite horizontal extent;
- Effects of the rotation of the earth are neglected;
- Vertical accelerations are neglected; the pressure in both layers is hydrostatic;
- Viscosity and density are assumed to be constant over a layer;
- The fluid in both layers is assumed to be incompressible;
- The interface is assumed to be stable, which means no mixing between the layers is present;
- The lower layer is assumed to rest on a rigid horizontal bed at which level no motion exists;
- The horizontal velocity in the upper layer is assumed to be independent of depth.

Based on the mentioned assumptions, the continuity equation and momentum equation for the upper layer can be expressed as shown in equations (2.2) and (2.3) and for the fluid mud layer as equation (2.4) and equation (2.5).

Upper layer:

$$\frac{\partial u_w}{\partial t} + g\frac{\partial (h_m + h_w)}{\partial x} = 0 \tag{2.2}$$

$$\frac{\partial h_w}{\partial t} + h_{w0}\frac{\partial u_w}{\partial x} = 0 \tag{2.3}$$

Lower layer:

$$\frac{\partial u_m}{\partial t} + \gamma g\frac{\partial h}{\partial x} + (1-\gamma)g\frac{\partial (h_w + h_m)}{\partial x} = \nu\frac{\partial^2 u_m}{\partial z^2} \tag{2.4}$$

$$\int_0^{h_m} \frac{\partial u_m}{\partial x} dz + \frac{\partial h_m}{\partial t} = 0 \tag{2.5}$$

Boundary conditions as stated by Gade (1958):

$$h_{tot} = h_{tot0} + a\cos\omega t \qquad \text{at x = 0} \tag{2.6}$$
$$u_m = 0 \qquad \text{at z = 0} \tag{2.7}$$
$$\partial u_m/\partial z = 0 \qquad \text{at z = } h_{m0} \tag{2.8}$$

By assuming harmonic solutions that are separable in time and x-direction for each variable, a dispersion relation can be derived which is explicit (equation (2.9)).

$$k = \pm\omega \frac{(h_{w0} + \Gamma h_{m0}) \pm \sqrt{(h_{w0} + \Gamma h_{m0})^2 - 4\gamma\Gamma h_{w0} h_{m0}}}{2\gamma g h_{w0}\Gamma h_{m0}} \tag{2.9}$$
$$\Gamma = 1 - \frac{\tanh mh_{m0}}{mh_{m0}} \tag{2.10}$$
$$m = (1-i)\sqrt{\omega/(2\nu_m)} \tag{2.11}$$

This relation gives 4 solutions. According to Kranenburg (2008) the most relevant solution is, in analogy with a two-layer system of fluids with the same viscosity, the external wave travelling in positive direction. This results in a complex wave number $k = k_r + ik_i$, of which the imaginary part represents the wave attenuation. Gade (1958) finds that the decay of the wave energy over the mud layer is exponential in x-direction as long as k_i is constant. Also, most damping occurs if the mud layer thickness h_{m0} is approximately equal to 1.2 times the Stokes boundary layer thickness ($h_{m0} = 1.2\sqrt{2\nu_m/\omega}$). Gade (1958) also states that the internal wave will always lag behind the surface wave; hence there will always be transport of energy from the upper to the lower layer.

SWAN-Mud

The work of Gade (1958) is, of course not, complete. It neglects, for example, the viscosity of the water layer and the effects of elasticity, porosity and plasticity in the lower layer (Kranenburg et al., 2011). Several authors have since published improvements to the early work of Gade (1958) to include one or more of these effects or to link the two-layer systems to existing phase-resolving and phase-averaging 1D or 2D wave-models. The applicability of these models, however, is either too limited or the model formulations are too complicated for large-scale engineering purposes. Therefore, Kranenburg et al. (2011) presented a new dispersion relation called the Delft Dispersion Relation, in combination with an energy dissipation equation, based on the work of De Wit (1995). The relations are valid for deep-to-shallow water and for relatively thin mud layers compared to the wave length. The effects of elasticity and plasticity, however, are still neglected. The main difference with Gade (1958) is that the upper layer now also accounts for non-hydrostatic pressures (and thus vertical accelerations are accounted for in the momentum balance of the upper layer). Furthermore, these relations have not been implemented in the third generation, phase-averaged wave energy model SWAN, forming together SWAN-Mud. SWAN effectively solves the wave energy balance given in equation (2.12).

$$\frac{1}{E}\left(\frac{\partial E}{\partial t} + \frac{\partial c_{g,x}E}{\partial x} + \frac{\partial c_{g,y}E}{\partial y} + \frac{\partial c_\theta E}{\partial \theta}\right) = \frac{S_{tot}}{E} \tag{2.12}$$

The formulations of the continuity equation and momentum equations for each layer are given by (2.13) to (2.18), which follow the schematisation of the two-layer model as presented in figure 2.4.

Water Layer

$$\frac{\partial u_w}{\partial t} + \frac{1}{\rho_w}\frac{\partial p_w}{\partial x} = 0 \tag{2.13}$$
$$\frac{\partial w_w}{\partial t} + \frac{1}{\rho_w}\frac{\partial p_w}{\partial z} = -g \tag{2.14}$$
$$\frac{\partial u_w}{\partial x} + \frac{\partial w_w}{\partial z} = 0 \tag{2.15}$$

Mud Layer:

$$\frac{\partial u_m}{\partial t} + \frac{1}{\rho_m}\frac{\partial p_m}{\partial x} = \nu_m \frac{\partial^2 u_m}{\partial z^2} \tag{2.16}$$

$$\frac{1}{\rho_m}\frac{\partial p_m}{\partial z} = -g \tag{2.17}$$

$$\frac{\partial u_m}{\partial x} + \frac{\partial w_m}{\partial z} = 0 \tag{2.18}$$

The boundary conditions yield no slip at the rigid bed and no shear stresses at the interface. Harmonic solutions are assumed for the horizontal and vertical velocity and for the pressure. Small perturbations of the water level are assumed from the still water levels h_{tot0} and h_{m0}, with a phase lag ϕ between the free surface wave and the internal wave. Solving this system of equations iteratively leads to the DELFT dispersion relation (2.19) (with m as given in equation (2.11)).

$$\begin{aligned}
&\omega^4\left(\frac{\cosh(kh_{w0})\cosh(mh_{m0})}{k} - \frac{\rho_w}{\rho_m}\frac{\sinh(kh_{w0})\sinh(mh_{m0})}{m} + h_{m0}\frac{\rho_w}{\rho_m}\sinh(kh_{w0})\cosh(mh_{m0})\right)\\
&+\omega^3 2ik\nu_m\cosh(kh_{w0})(\cosh(mh_{m0})-1)\\
&+\omega^2 g\left(\frac{k}{m}\cosh(kh_{w0})\sinh(mh_{m0}) - kh_{m0}\cosh(kh_{w0})\cosh(mh_{m0}) - \sinh(kh_{w0})\cosh(mh_{m0})\right)\\
&+\omega 2igk^2\nu_m\sinh(kh_{w0})(1-\cosh(mh_{m0}))\\
&+g^2k^2\left(h_{m0}\frac{\rho_m-\rho_w}{\rho_m} - \sinh(kh_{w0})\cosh(mh_{m0}) - \frac{\rho_m-\rho_w}{\rho_m}\frac{\sinh(kh_{w0})\sinh(mh_{m0})}{m}\right)\\
&=0
\end{aligned} \tag{2.19}$$

The dissipation of wave energy by viscous dissipation in the fluid mud layer is implemented in SWAN through an additional contribution S_{mud} to the sink/source term S_{tot} in the energy balance (2.12). The wave-averaged work $\overline{P}$ done by the waves on the mud layer is, according to Gade (1958), equal to the energy transfer between the two layers and thus to the viscous dissipation within the fluid mud layer. Evaluating this interval for the system described in this equation (2.20) leads to the expression given by equation (2.21), with $\mathbb{R}\{\hat{p}_{w,z=h_{m0}}\}$ being the real part of the complex amplitude of the pressure in the water layer evaluated at the interface.

$$\overline{P} = -\frac{1}{T}\int_0^T p\frac{d\xi}{dt}dt \tag{2.20}$$

$$\frac{S_{\text{mud}}}{E} = \frac{\overline{P}}{E} = -\omega\frac{\mathbb{R}\{\hat{p}_{w,z=h_{m0}}\}}{\rho_w g a}\frac{b}{a}\sin\phi \tag{2.21}$$

The complex dispersion equation, as implemented in SWAN-Mud, is characterised by multimodal behaviour; multiple combinations of parameters can lead to the same damping characteristics. Kranenburg et al. (2011) notes, for example, that large and small viscosities, which characterise completely different situations, can still lead to the same wave damping. This leads to the conclusion that the wave height H_s and the spectral shape alone are not enough to arrive at a single viscosity value. Also, a spectral shape measure of the period is needed, for example T_{m01}. Mud layer thickness, mud layer density and mud layer viscosity are important parameters in the viscous model. According to Kranenburg et al. (2011), inverse modelling should also be possible. If enough information is available on the behaviour of the surface wave and the internal wave (and thus the damping rate), the external wave number and the mean wave period, T_{m01}, the thickness, density and viscosity of the mud layer can be retrieved from field data.

2.3. Effects of Wave Damping

Apart from energy, waves also transport momentum. The transport of momentum is dependent on, amongst other things, the amplitude of a wave. The transport of momentum through a vertical plane

by waves is called radiation stress (S_{xx}), which is defined by Longuet-Higgins and Stewart (1964) as 'the excess flow of momentum due to the presence of waves'. These radiation stresses can be represented by a shear stress, and horizontal variations in these stresses can be considered as forces on the water column. Therefore, these gradients may lead to a tilt in the water level or the generation of currents. Due to damping, the amplitude of the wave changes in a horizontal direction, and so does the momentum transport. This, in turn, will have consequences for flow and water levels. The interaction between waves and the water column via this change in momentum transport is quite well known for a single layer system (section 2.3.1). For a two-layer system, like the water-fluid mud systems described by Gade (1958) and Kranenburg et al. (2011), considerably less is known and it is therefore worth considering the response of the water-mud column to such a forcing (section 2.3.3).

2.3.1. Radiation Stress in a single layer system

In order to derive the radiation stress for a two-layer system, first the radiation stress in the case of a single layer is examined in more detail. In the following, the approach of Longuet-Higgins and Stewart (1964) is followed. Momentum is the product of mass and velocity. If expressed as a momentum density, the definition is ρu, in which u is a vector with magnitude and direction.

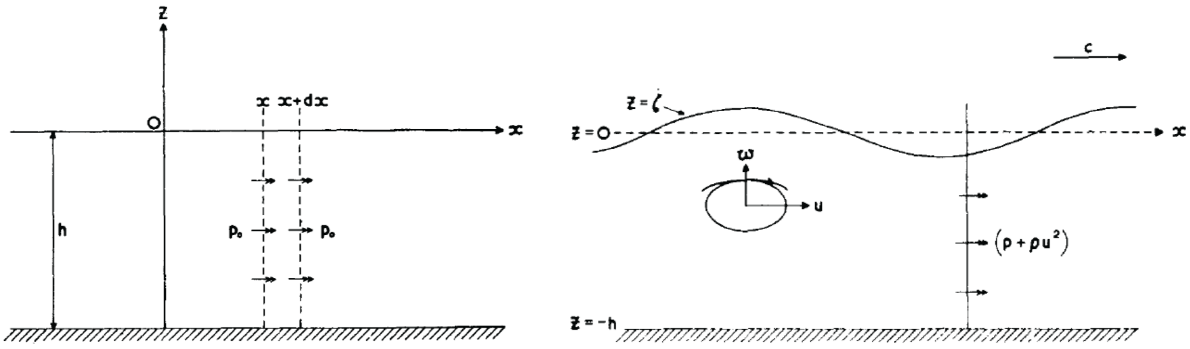

Figure 2.5: The momentum flux in a stationary fluid (left) and in a progressive wave (right). Adapted from Longuet-Higgins and Stewart (1964).

First consider an undisturbed body of water of uniform depth (figure 2.5). The pressure at any point is equal to the hydrostatic pressure p_0 and thus the total flux of momentum between the bottom and the free surface is $\int_{-h}^{0} p_0 dz$. Now, consider a simple progressive wave travelling in x-direction (figure 2.5). There are two contributions to the transport of momentum in x-direction through a window $\Delta z \Delta y$, ; the bodily transport of x-momentum ρu by a velocity u in x-direction and the momentum transferred by the pressure, p. The total transport through a vertical window $\Delta z \Delta y$ during a time interval Δt is therefore $(\rho u^2 + p)\Delta z \Delta y \Delta t$. The total amount of momentum transferred through this window per unit crest width, per unit time, is given by the first term in equation (2.22). The overbar denotes time-averaging over the wave period. Minus the second term, the mean flux of momentum in absence of waves, gives the normal component in x-direction of the radiation stress S_{xx}.

$$S_{xx} = \overline{\int_{-h}^{\eta} (\rho u^2 + p) dz} - \int_{-h}^{0} p_0 dz \tag{2.22}$$

$$= S_{xx}^{(1)} + S_{xx}^{(2)} + S_{xx}^{(3)} \tag{2.23}$$

in which:

$$S_{xx}^{(1)} = \overline{\int_{-h}^{\zeta} \rho u^2 dz} = \int_{-h}^{0} \rho \overline{u^2} dz \tag{2.24}$$

$$S_{xx}^{(2)} = \overline{\int_{-h}^{0} p - p_0 dz} = \int_{-h}^{0} \overline{p} - p_0 dz = \int_{-h}^{0} -\rho \overline{w^2} dz \tag{2.25}$$

$$S_{xx}^{(3)} = \overline{\int_{0}^{\zeta} p dz} = \frac{1}{2} \rho g \overline{\zeta^2} \tag{2.26}$$

The radiation stress can be subdivided into three components (equation (2.23)). The upper limit $z = \zeta$ of the first component, $S_{xx}^{(1)}$, may be replaced with the mean surface level $z = 0$ as the additional range only contributes to a third order term. Because the limit is now constant, the wave-average value can be transferred into the integrand. This contribution is then equal to the Reynolds stress ρu^2 integrated from the bottom to the surface. For the second component, $S_{xx}^{(2)}$, the mean value can be taken into the integrand as well (equation (2.24)). This term arises from the change in mean pressure within the fluid. The mean flux of vertical momentum across a horizontal plane, $\overline{p + \rho w^2}$ (with w the velocity in z-direction), should be of such magnitude that it supports the weight of the water above it. This is equal to the hydrostatic pressure at that level, p_0, which leads to the balance $\overline{p + \rho w^2} = p_0$ and thus $\overline{p} - p_0 = -\rho \overline{w^2}$ (equation (2.25)). $S_{xx}^{(1)}$ and $S_{xx}^{(2)}$ can then be combined to $\int_{-h}^{0} \rho(\overline{u^2 - w^2}) dz$. In deep water, the orbital motion of the water particles is a circle, hence the contribution of $S_{xx}^{(1)} + S_{xx}^{(2)}$ equals 0. In shallow water, the particle orbits are elongated horizontally, hence $u^2 >> w^2$. It can be shown (Longuet-Higgins and Stewart, 1964) that this component of the radiation stress is then equal to twice the kinetic energy of the waves; $2E$. The third component, $S_{xx}^{(3)}$, is equal to the pressure p integrated between the mean surface elevation and ζ, averaged over the wave period. Close to the free surface, the pressure is nearly equal to the hydrostatic pressure, $p = \rho g(\zeta - z)$. The pressure thus fluctuates in phase with the free surface elevation. Longuet-Higgins and Stewart (1964) show that, using linear wave theory, the expressions (2.24), (2.25) and (2.26) can be directly related to the wave energy $E = \frac{1}{2} \rho g a^2$ (equation (2.27)), with a the wave amplitude.

$$S_{xx} = E\left(\frac{2kh}{sinh(2kh)} + \frac{1}{2}\right) \tag{2.27}$$

2.3.2. Effect of radiation stress in a single layer system

When waves travel into shallow water and thus encounter the bottom, these waves will shorten, steepen and eventually break. After breaking, the waves will continue to travel towards the coast with a reduced wave height. These changes in wave height also imply changes in radiation stress and thus horizontal gradients. These gradients are equivalent to forces and should thus be included in the momentum balance (equation (2.28)). When stationary conditions are assumed and wind input ($\tau_{W,x}$) and bottom stress ($\tau_{B,x}$) are neglected, as well as variation in bathymetry and alongshore variation in wave condition, a balance between the radiation stress gradient and the wave average surface level remains (equation (2.29)). The gradient in radiation stress is negatively proportional to the gradient in mean surface level, hence a decrease in wave energy and thus radiation stress in shoreward direction, will lead to a setup in the mean water level.

$$\frac{\partial \overline{U}}{\partial t} + \overline{U} \frac{\partial \overline{U}}{\partial x} = g \frac{\partial \overline{\zeta}}{\partial x} - \frac{1}{\rho h} \frac{\partial S_{xx}}{\partial x} + \left. \frac{\tau_{w,x}}{\rho h} \right|_{z=0} - \left. \frac{\tau_{B,x}}{\rho h} \right|_{z=-h} \tag{2.28}$$

$$\frac{\partial \overline{\zeta}}{\partial x} = -\frac{1}{\rho g h} \frac{\partial S_{xx}}{\partial x} \tag{2.29}$$

The derivation presented above is only valid when a coastal boundary is present against which the water can be pushed up, forming the gradient in mean surface level. When such a coastal boundary is not present, the changes in radiation stress must be balanced by the bottom shear stress. For this shear

stress to exist, however, a wave-averaged flow should be present - a current. An example of this is the longshore current generated by waves approaching the shore under an angle, see Longuet-Higgins (1970).

2.3.3. Radiation stress in a two-layer system

For a system with a water layer on top of a fluid mud layer, the same assessment with regard to the transport of momentum can be made as for a single layer system (as in section 2.3.1). In the case of the two layer system, however, the density is not uniform over depth. Also, an internal wave will be forced on the interface of the two layers by the free surface wave. Both these differences can have an effect on the transport of momentum by waves and thus in this section a new expression is derived for the radiation stress in a two-layer system, based on Motohiko and Shintani (2006).

In contrast with Longuet-Higgins (1970) and Motohiko and Shintani (2006), the schematisation earlier used in this thesis (figure 2.4) is adopted. This means z is taken positive upwards and $z = 0$ denotes the bottom. The transport of momentum will in this case not be assessed for the total water column, but rather per layer. The transport through a vertical window $\Delta y \Delta z$ during a time interval Δt *per layer* is still equal to $(\rho u_i^2 + p_i)\Delta z \Delta y \Delta t$, in which $i = w$ denotes the upper water layer and $i = m$ denotes the lower fluid mud layer. The total amount of momentum transferred through this window (over the full water column per unit time per unit crest width, averaged over the wave period) is equal to the addition of the first and third term on the right hand side of equation (2.30). To get the mean transport of momentum by waves, the pressure contribution in the absence of waves in each layer (the second and the fourth term in equation (2.30)), has to be subtracted, after which the radiation stress is found. The first and second term form the radiation stress in the upper water layer, $S_{xx,w}$, the third and fourth term form the radiation stress in the lower layer, $S_{xx,m}$. In the following, the radiation stress terms for the different layers will be treated separately.

$$S_{xx} = \overline{\int_{h_{m0}+\xi}^{h_{toto}+\zeta} (\rho_w u_w^2 + p_w) dz} - \int_{h_{m0}}^{h_{toto}} p_0 dz + \overline{\int_0^{h_{m0}+\xi} (\rho_m u_m^2 + p_m) dz} - \int_0^{h_{m0}} p_0 dz \tag{2.30}$$

or separated per layer:

$$S_{xx,w} = \overline{\int_{h_{m0}+\xi}^{h_{toto}+\zeta} (\rho_w u_w^2 + p_w) dz} - \int_{h_{m0}}^{h_{toto}} p_0 dz$$

$$S_{xx,m} = \overline{\int_0^{h_{m0}+\xi} (\rho_m u_m^2 + p_m) dz} - \int_0^{h_{m0}} p_0 dz$$

Water Layer

The radiation stress for the water layer, $S_{xx,w}$ can be further subdivided in four terms (equation (2.32)). The first two terms, $S_{xx,w}^{(1)}$ and $S_{xx,w}^{(2)}$ are evaluated in the same manner as for the single layer system. It should be noted, that the contributions of both ζ and ξ in $S_{xx,w}^{(1)}$ are to the third order and are thus both neglected in the limits of this integrand. $S_{xx,w}^{(1)}$ and $S_{xx,w}^{(2)}$ can again be combined to $\int_{h_{m0}}^{h_{toto}} \rho_w \overline{u_w^2 - w_w^2} dz$. The third term, $S_{xx,w}^{(3)}$ (2.35), is equal to the pressure integrated between the mean surface level and ζ, averaged over the wave period and can be evaluated under the same assumption as the single layer case. The derivation of this term is shown in appendix A. The term $S_{xx,w}^{(4)}$ (2.36) describes the influence of the internal wave, as this perturbation from the equilibrium conditions changes the contribution of the pressure to the momentum transport. The internal wave is neglected, however, in the term $S_{xx,w}^{(2)}$ (2.34) (the lower limit is expanded from $h_{m0} + \xi$ to the equilibrium level h_{m0} and thus the effect of the internal wave is not included). This term is derived in appendix A.

$$S_{xx,w} = \overline{\int_{h_{m0}+\xi}^{h_{toto}+\zeta} (\rho_w u_w^2 + p_w) dz} - \int_{h_{toto}}^{h_{m0}} p_0 dz \tag{2.31}$$

$$= S_{xx,w}^{(1)} + S_{xx,w}^{(2)} + S_{xx,w}^{(3)} + S_{xx,w}^{(4)} \tag{2.32}$$

in which:

$$S_{xx,w}^{(1)} = \overline{\int_{h_{m0}+\xi}^{h_{toto}+\zeta} \rho_w u_w^2 dz} = \int_{h_{m0}}^{h_{w0}} \rho_w \overline{u_w^2} dz \tag{2.33}$$

$$S_{xx,w}^{(2)} = \overline{\int_{h_{m0}}^{h_{toto}} p - p_0 dz} = \int_{h_{m0}}^{h_{toto}} \overline{p} - p_0 dz = \int_{h_{m0}}^{h_{toto}} -\rho_w \overline{w_w^2} dz \tag{2.34}$$

$$S_{xx,w}^{(3)} = \overline{\int_{h_{toto}}^{h_{toto}+\zeta} p dz} = \frac{1}{2}\rho g \overline{\zeta^2} \tag{2.35}$$

$$S_{xx,w}^{(4)} = -\overline{\int_{h_{m0}}^{h_{m0}+\xi} p dz} = -\overline{p_{\text{wave}}\xi} - \frac{1}{2}\rho_w g \overline{\xi^2} \tag{2.36}$$

Mud Layer

The radiation stress for the mud layer can, like in the case of the radiation stress for a single layer system, be subdivided in three components (equation (2.38)). The first two terms, $S_{xx,m}^{(1)}$ and $S_{xx,m}^{(2)}$ can be evaluated in the same way as done for the water layer. The contribution of ξ in $S_{xx,w}^{(1)}$ is again neglected in the limit. $S_{xx,m}^{(1)}$ and $S_{xx,m}^{(2)}$ can then be combined to $\int_0^{h_{m0}} \rho_m \overline{u_m^2 - w_m^2} dz$, representing the transport of momentum over the mud layer due to the orbital motion of the mud particles induced by the waves. Again, the perturbation of the interface by the internal wave is ignored in these terms and needs to be corrected for. This leads to the term $S_{xx,m}^{(3)}$ (2.41), the derivation of which can be found in Appendix A.

$$S_{xx,m} = \overline{\int_{0}^{h_{m0}+\xi} (\rho_m u_m^2 + p_m) dz} - \int_{h_{m0}}^{0} p_0 dz \tag{2.37}$$

$$= S_{xx,m}^{(1)} + S_{xx,m}^{(2)} + S_{xx,m}^{(3)} \tag{2.38}$$

in which:

$$S_{xx,m}^{(1)} = \overline{\int_{0}^{h_{m0}+\xi} \rho_m u_m^2 dz} = \int_{0}^{h_{m0}} \rho_m \overline{u_m^2} dz \tag{2.39}$$

$$S_{xx,m}^{(2)} = \overline{\int_{h_0}^{H_{m0}} p - p_0 dz} = \int_{0}^{h_{m0}} \overline{p} - p_0 dz = \int_{h_0}^{h_{m0}} -\rho_m \overline{w_m^2} dz \tag{2.40}$$

$$S_{xx,m}^{(3)} = \overline{\int_{h_{m0}}^{h_{m0}+\xi} p dz} = \overline{p_{\text{wave}}\xi} + \frac{1}{2}\rho_m g \overline{\xi^2} \tag{2.41}$$

2.3.4. Effect of radiation stress on a two-layer system

Due to damping of waves by fluid mud as described in previous sections, the radiation stress in both layers will decrease in shoreward direction. In analogy with the single-layer system (section 2.3.2), a set-up of the free surface level and the interface is expected in case a coastal boundary is present. This would potentially mean a large amount of sediment transport towards the coast.

$$\frac{\partial \overline{U_w}}{\partial t} + \overline{U_w}\frac{\partial \overline{U_w}}{\partial x} = -g\frac{\partial \overline{\zeta}}{\partial x} - \frac{1}{\rho_w H_{w0}}\frac{\partial S_{xx,w}}{\partial x} + \frac{\tau_{W,x}}{\rho_w h_{w0}}\bigg|_{z=h_{tot0}} - \frac{\tau_{i,x}}{\rho h_{w0}}\bigg|_{z=h_{m0}} \tag{2.42}$$

$$\frac{\partial \overline{U_m}}{\partial t} + \overline{U_m}\frac{\partial \overline{U_m}}{\partial x} = -g\frac{\partial \overline{\zeta}}{\partial x} - \frac{g\Delta\rho}{\rho_m}\frac{\partial}{\partial x}(\overline{\xi} - \overline{\zeta}) - \nu_m\frac{\partial^2 \overline{U_m}}{\partial x^2} - \frac{1}{\rho_m h_{m0}}\frac{\partial S_{xx,m}}{\partial x} + \frac{\tau_{i,x}}{\rho_m h_{m0}}\bigg|_{z=h_{m0}} - \frac{\tau_{B,x}}{\rho_m h_{m0}}\bigg|_{z=0} \tag{2.43}$$

In analogy with the single-layer system, a depth-averaged momentum balance can be defined for both layers (equations (2.42) and (2.43), see also Winterwerp et al. (2019)). Assuming stationary conditions, all terms $\frac{\partial}{\partial t}$ may be dropped from the equations. Here, it is also assumed there is a coastal boundary, which means that the depth averaged velocities $\overline{U_w}$ and $\overline{U_m}$ must be 0 to be able to reach equilibrium. Wind ($\tau_{W,x}$) is not taken into account, and neither is bottom shear stress ($\tau_{B,x}$) A horizontal pressure gradient will then balance any change in radiation stress. This pressure gradient is formed by a combination of the slope of the surface level and the slope of the interface level. Equations (2.44) and (2.45) are the remaining balances under these assumptions.

$$\frac{\partial \overline{\zeta}}{\partial x} = -\frac{1}{g\rho_w h_{w0}}\frac{\partial S_{xx,w}}{\partial x} \tag{2.44}$$

$$\frac{\partial \overline{\xi}}{\partial x} = (1 - \frac{\rho_m}{\Delta\rho})\frac{\partial \overline{\zeta}}{\partial x} - \frac{1}{g\rho_m h_{m0}}\frac{\partial S_{xx,m}}{\partial x} \tag{2.45}$$

The set-up/set-down of both the surface and interface level can now be quantified using the expressions for the radiation stress for the water layer $S_{xx,w}$, and for the mud layer, $S_{xx,m}$, as presented in section 2.3.3.

2.4. Observed Set-up: Hypotheses

As mentioned in section 1.1.4, sloping fluid mud interfaces have been observed in the field. The driving mechanism behind these gradients is poorly understood, but may well be related to the wave forcing and the associated wave set-up. Not much research has been done so far into this phenomenon, neither in the laboratory or in the field. Therefore, several hypotheses are posed in this section to provide an explanation for these observations.

2.4.1. Hypothesis 1: Viscous mud layer

The driving force behind the measured set-up is assumed to be the damping of the waves by the fluid mud layer. As reasoned in section 2.3.4, the system is in equilibrium and there is a balance between the radiation stress gradients, the gradient in the surface level elevation and the gradient in the elevation of the fluid mud interface. This hypothesis will be explored further in this thesis. The assumed equilibrium implies, that the gradient in the fluid mud layer interface follows a change in hydrodynamic conditions without a significant time lag. For an inviscid fluid, this would be true. Fluid mud, however, is a viscous fluid and thus a time lag can be expected in the response of the layer to forcing. Furthermore, in section 2.1.1 it is stated that the behaviour of mud resembles the behaviour of a Bingham fluid. It can thus be expected that there is a certain yield stress within the mud that needs to be overcome before the fluid will move. Hence, only higher hydrodynamic loads will be able to move the layer. This is not taken into account in this hypothesis.

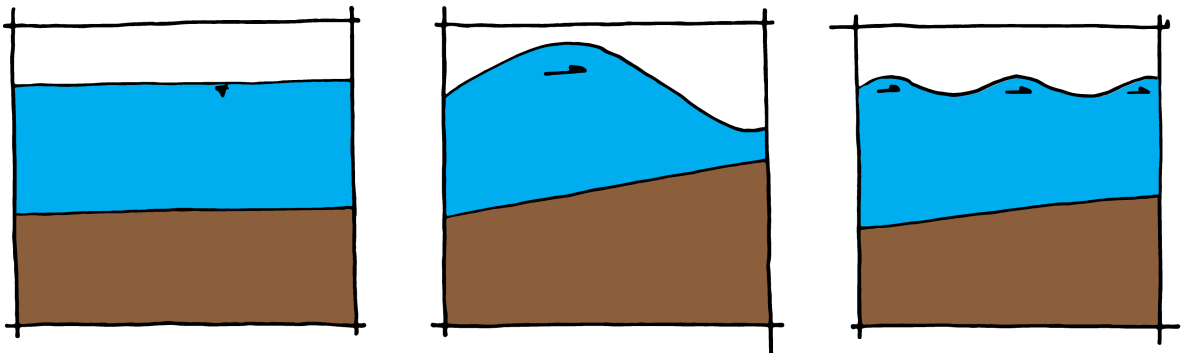

Figure 2.6: Hypothesis 1. There is a balance between the horizontal gradient in radiation stress and the set-up of the fluid mud interface. More damping occurs for larger waves, hence larger waves will cause a larger set-up of the mud layer. The mud layer is able to follow the hydrodynamics without lag. When the wave force diminishes, so will the gradient of the interface.

2.4.2. Hypothesis 2: Plasto-viscous mud layer

If it is assumed that the fluid mud layer will respond like a non-Newtonian fluid (section 2.1.1), then the flow needs to overcome a certain threshold of shear stress in the mud layer to be able to initiate movement of the layer. After this initiation of movement, the layer will respond as described for Hypothesis 1 - a slope will be formed at the interface, which will be sustained as long as the hydrodynamic forcing is large enough. When the forcing diminishes, the gradient in the mud layer interface will reduce to a degree that can be sustained by the yield stress of the layer, τ_y. This would provide an explanation for the observations of relatively large slopes even in calm conditions.

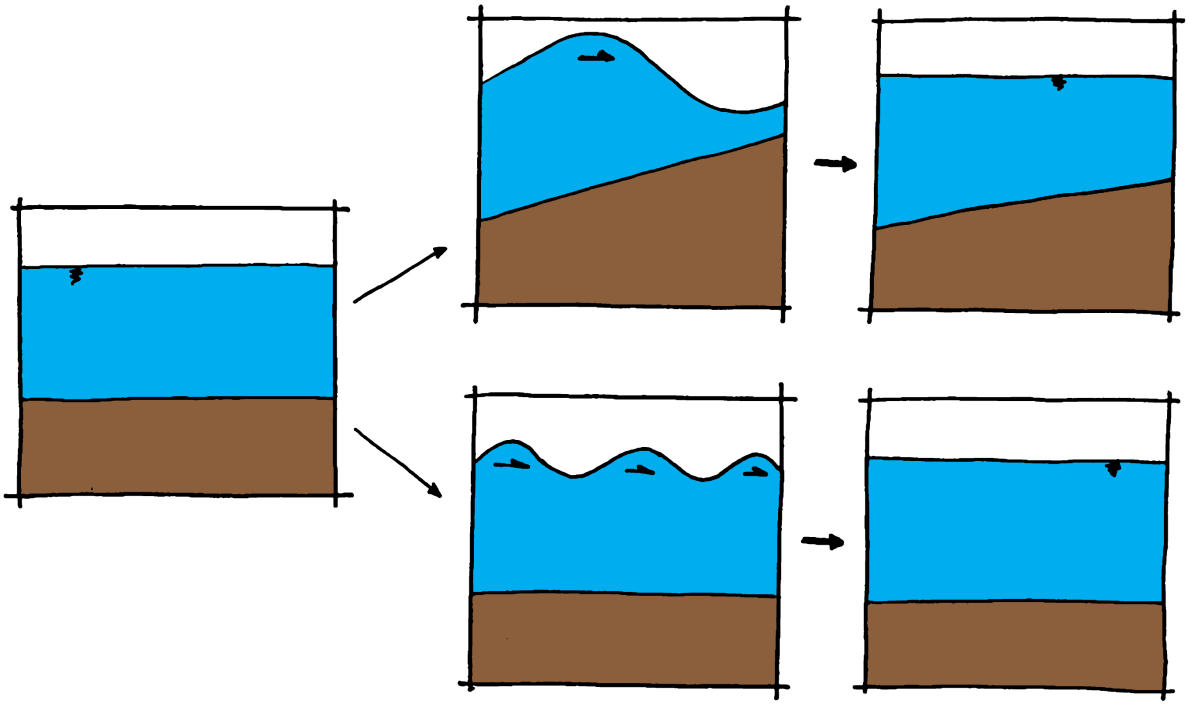

Figure 2.7: Hypothesis 2. The mud behaves like a Bingham fluid and has a certain yield strength. Therefore, only the largest part of the waves is able to set the layer to motion and cause a gradient in the interface level. In case the mud layer is mobilised, when the wave force diminishes the mud layer will adopt a new equilibrium and a slope will remain that can be sustained by the yield strength of the mud.

2.4.3. Hypothesis 3: Plasto-viscous mud layer and strength development

The strength of a mud layer is not uniform in time nor depth. The strength further down in the mud layer will be higher. This is because more consolidation will have taken place deeper in the mud layer; the load on the mud deeper in the layer is larger as more mud is weighing down on it from above. Therefore, higher waves will be able to mobilise a larger part of the mud layer than smaller waves. Furthermore, when shear occurs within the layer due to the wave forcing, the flocs within the mud layer will break and the water will be able to flow out of the layer more easily. This accelerates the initial consolidation of the bed (priv. comm. Winterwerp, 2018). A more consolidated bed has a higher bulk density and a higher volumetric concentration. As the viscosity is positively related to the volumetric concentration (Kranenburg, 1994), the viscosity will increase during consolidation as well, leading to a higher amount of damping of the waves. After a storm, flocs will reform and, as the bed is now more consolidated, the mud has a higher strength than before the storm. Therefore, the yield strength of the mud is expected to become larger in time. Therefore, at the end of a storm season, the mud layer will be stronger than at the beginning, meaning it can sustain larger slopes at the end of a season.

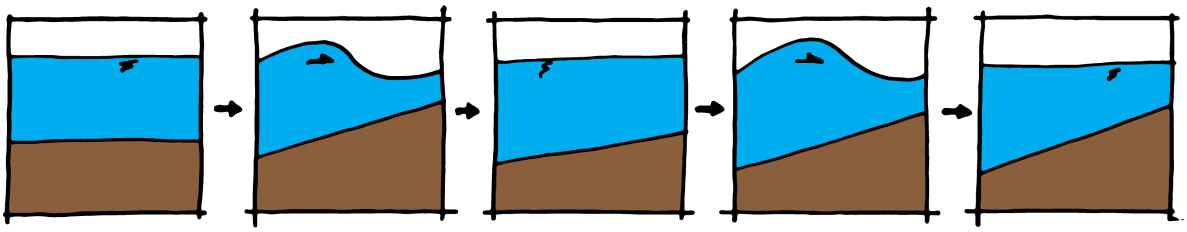

Figure 2.8: Hypothesis 3. The mud layer strengthens over the season; the yield strength increases. Therefore, the slopes that can be sustained by the yield stress will become larger over time.

3

Measurement Campaign

To assess the fluid mud layer's response to forcing, a combination of a field campaign and modelling work has been used. This campaign took place between the 5th of November and 11th of December 2018. The choice for these dates was based on the expected time of occurrence of the NW monsoon. As the movement and possible set-up of the fluid mud layer is thought to be highly dependent on storm conditions (which occur during the NW monsoon), the field campaign was set up to gain information on the response of the system to such conditions. Furthermore, the results of the field campaign will be used to validate a SWAN-Mud model, which can thereafter be used to assess the response of the system to other characteristic events in this area (chapter 4). In this chapter, the measurement campaign will be described and the results will be evaluated.

The choice of location of the measurements is elaborated upon in section 3.2. In section 3.1, the actual measurements that have been performed are described. In section 3.3, the results of these measurements have been presented.

3.1. Measurement Locations

Not all locations along the coast of Demak are suitable for the type of measurements described in the following sections. Locations were selected that fulfilled the following requirements;

1. The location needs to have a fluid mud layer.

2. The mud layer needs to have a sufficient thickness. Based on Gade (1958) a first indication can be made when assuming that most wave damping is expected when the thickness of the mud layer is approximately equal to 1.2 times the thickness of the Stokes boundary layer ($h_m = 1.2\sqrt{2\nu_m/\omega}$, with ν_m the viscosity of the mud-layer and ω the wave frequency). This results in a preferred thickness of 0.3 to 0.5 m.

3. The location needs to be under forcing by waves.

4. Preferably, but not necessarily, the mud layer interface needs to have a cross-shore gradient.

5. The mud layer must stay submerged 100% of the time and enough water depth must be available to be able to mount wave gauges and for the sensors of wave gauges to be submerged during most of the tidal cycle.

Ultimately, 2 locations were selected. Neither of the locations satisfied the fifth requirement; in order to have a large enough horizontal distance between 2 measurement stations at a certain location, this requirement was deemed too stringent. During low tide, the instruments closest to the coast were not submerged.

Figure 3.1: Overview of the two locations chosen for the measurement campaign. In the upper left panel, the location close to Bedono Bay (in the lower panel denoted by 'Bedono 1') and in the upper right panel, the location close to Surodadi. The hybrid dams adjacent to this measurement location has been denoted in green.

Surodadi

The first location was chosen close to the village of Surodadi (figure 3.1). It is located next to two hybrid dams, which were expected not to influence the waves at the measurement locations. The thickness of the mudlayer was notably larger closer to shore than sea, indicating a possible gradient. The mudlayer extends about 250 to 300 m from the coast, where it transitions into a submerged chenier. It was observed that sufficient waves reach the measurement location.

Bedono Bay

The second location is located close to Bedono Bay (figure 3.1). It is a little bay, through which waves are able to propagate without disturbance. The thickness of the mud layer is again larger near the shore, transitioning into a sandy bottom near the end of the bay. This is also noticeable in the observed sediment composition; the sediment gets more sandy near the end of the bay.

3.2. Layout Field Experiments

At both locations described in section 3.1, the same combination of instruments was applied. A measurement transect was set out in the approximately dominant wave direction. On both ends of this transect, a measurement pole was placed. With the instruments attached to those two poles, the changes in hydrodynamics could be assessed over the length of the transect. To each pole, the following instruments were attached (figure 3.2);

- Wave Gauge (section 3.2.1)
- Echosounder (section 3.2.2)
- ADV (section 3.2.3)

Furthermore, in the vicinity of these poles, mud floaters were deployed (section 3.2.4). Along the transects, regular bathymetric surveys were taken (section 3.2.5).

3.2.1. Wave Gauge

Two wave gauges (Ocean Sensor Systems, Inc.; OSSI-010-003C) were used to measure pressure at both of the measurement poles. One, mounted to a pole at the beginning of the transect, was used to

(a) From left to right; echologger, wave gauge, ADV

(b) Close-up of attachment wave gauge (left) and echologger (right).

Figure 3.2: Measurement pole during the last stage of the measurement campaign at Surodadi.

measure the water level variations due to the incoming waves, and the other, mounted to a pole at the end of the transect, to measure the outgoing waves. Together, these measurements give an indication of the wave transformation over the transect. The wave gauges were measuring continuously over each deployment at a sampling frequency of 10 Hz and were mounted approximately 15 cm above the mud-water interface.

3.2.2. Echosounders

Two echosounders were deployed to monitor the mud-water interface and possibly identify internal waves. Two types of echosounders were used, both manufactured by EchoLogger; a type EA400 and a type AA400. The former instrument is more advanced than the latter and was preferred. Unfortunately only one instrument of this type was available at the time of the field campaign; the EA400 has a larger memory and battery capacity and saves the full backscatter profile. The AA400 is much more limited; it saves only the interface level, which is determined internally based on predefined user settings.

The detection of this interface by the echosounders is not very straightforward and depends largely on the applied user settings. The level of the interface is determined from the amount of backscatter of the acoustic beam returned to the sensor. The interface is considered to be the level where this backscatter exceeds a certain user-defined level. The problem here is that the definition of this interface is vague; in this case (water-fluid mud), it is rather a strong gradient in the concentration of sediment instead of a transition from a fluid (water), to a solid (for example sandy) bottom . Furthermore, the acoustic signal can saturate inside the top part of the mud layer. This can be corrected for in case of the EA400 by reducing the gain of the instrument, but not in case of the AA400. Because of these reasons, the EA400 has the edge over the AA400, as the interface level can be determined by the user from the backscatter readings afterwards. During the course of the fieldwork, several different configurations of the user settings were tested. The final settings have been displayed in table 3.1.

	Interval [s]	Series [#]	Frequency [Hz]	Threshold [%]	Gain [dB]	Blanking Distance [mm]	Range [mm]	Sound speed [m/s]
EA400	10	100	10	15	-6	150	1000	1540
AA400	1	5	10	15	N/A	200	1000	1540

Table 3.1: Settings used for the echosounders during the final deployment 2018-12-04 at Surodadi.

Both instruments were installed approximately 30 cm above the mud-water interface. Both instruments have a minimum blanking distance of 15 to 20 cm. This means that the instrument will not measure the backscatter within this distance from its sensor and thus the distance to the fluid mud interface should be at least larger than that. The applied distance was considered to be sufficient, as an accretion of more than 10 cm was not within the expected range. To avoid measuring the possible scour holes around the poles, the echosounders were placed about 20 cm away from the main pole on a cross-bar (figure 3.2b).

3.2.3. ADV

Two ADVs (Nortek; Vector) were used to characterise the near-interface velocity. The measurement volume of the ADV was located 5 cm above the interface; in this way, the instrument was placed close enough to the mud-water interface to have an indication of the velocities at the interface, but far away enough to avoid the measurement volume of the instrument getting buried. The ADVs were mounted on crossbars attached to the measurement poles. To reduce the influence of the poles on the measured flow pattern, the ADVs were mounted at about 30 cm distance from the poles. The measurements of the ADVs and wave gauges can be directly linked, as the instruments are measuring at the same location.

As the availability of the ADVs was limited, they were only deployed for 1.5 days, during which the instruments were measuring continuously at a sampling frequency of 32 Hz.

3.2.4. Mud Floaters

To obtain an indication of the horizontal movement of the mud layer, 'mud floaters' have been applied in this layer. These mud floaters act like drifters; they have about the same density as mud and will therefore be displaced along with the mud if transport occurs within the layer. It is important that the floaters stay at approximately the same height in the mud layer, as the horizontal velocity in the layer is dependent on the depth within the layer. Also, the floater should be displaced at the same pace as the mud.

Requirements

In order for the floaters to function as envisaged, their design should fulfils the following requirements:

1. The floater should be small enough relative to the thickness of the mud layer, which is, according to section 3.1, in the order of decimetres.

2. The floater should stay at the same vertical level in the mud and should move at the same pace as the mud. It follows, then, that the floater should have the same density as mud.

3. The floater should not be influenced by any other forces than the driving force of the motion of the mud.

4. The floater should be constructed from locally available parts. As the measurement locations are remote, repairing or replacing high-tech parts or elements will be difficult.

Design

For the floater design, coloured plastic balls with a diameter of about 5 cm were used. This diameter was hypothesised to be small enough with regard to depth of the mud layer. These balls were filled with mud that was collected close to the location of deployment (not *at* the location of deployment, as this would have disturbed the mud layer before the start of the measurements). To be able to locate the floaters after deployment, they were connected to a pole using fishing wire. By using this type of wire, additional drag on the balls by the rope due to the flowing water was prevented as much as possible. Another option considered for localisation of the balls was a small buoy on the water surface. It was, however, feared that this floater would pull the ball through the mud. Therefore, a fixed pole with sufficient length of free wire was used.

Deployment

In principle, the measurement poles were used for the installation of the mud floaters. Whenever this was not possible for any kind of practical reason, different poles were placed in the vicinity of the measurement poles, so wave events could be linked to the results of the mud floaters. Several mud floaters per pole were deployed at two different depths; 10 cm and 30 cm under the mud-water interface. In the final deployments, four floaters were used for each level (figure 3.3). The position of the mud floaters was checked at deployment and at retrieval. The observed movement is therefore an integrated measure for the movement of the mud layer over the period of time the mud floaters were deployed. The measurements were taken by placing a small pipe on top of the mud floater (about 1.5 cm diameter), from which the distance towards the pole could be measured. The poles to which the floaters were attached form a non-moving reference point, as they were driven 2 meters into the consolidated bottom. By measuring several mud floaters at the same depth, the quality of the measurement was thought to be enhanced. Due to practical considerations, the data collection method could not be executed as non-destructive. It has therefore only been applied at the deployment and retrieval of the mud floaters, as the mud layer surrounding the mud floaters would have been severely disturbed during the measurements. The downside of this measurement technique is that it introduces a measurement error which is relatively large compared to the quantities measured. In order to limit this measurement error, the pipe would need to have been positioned in the middle of the mud floater. Also, the pipe ideally should have been kept perpendicular the water level during the measurements. Both requirements are hard to achieve, introducing a measurement error in the order of centimetres.

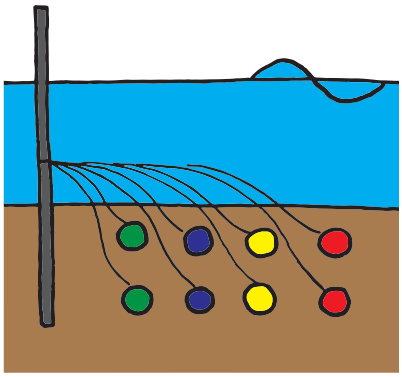

Figure 3.3: Schematisation of the mud floater deployment.

3.2.5. Level of the Mud-Water Interface and the Bottom

To have an indication of changes in the mud layer thickness over time and the response of this layer to wave driven events, regular bathymetric surveys were conducted along the transect between the two instrument poles. A metal rod (about 2 m length and 2 cm by 5 cm in diameter) with measurement tape attached to it was pushed through the mud by hand until it couldn't be pushed further. This depth was taken as the level of the consolidated bottom. The distance between the water surface and the interface has been determined using a separate measurement tape. These measurements were collected multiple times throughout the study There were approximately 20-25 data collection points along the transect between the 2 poles, and GPS co-ordinates were taken at each one of these points in order to be able to construct a bathymetry along the transect.

3.2.6. Mud characteristics

As the behaviour of the fluid mud layer is strongly dependent on the properties of the mud, samples were taken in the vicinity of the measurement area. The density of the samples was in the range of 1200-1250 kg/m^3. Deltares has determined flow curves (figure 3.4) to characterise the rheology of the fluid mud. Based on these flow curves, the viscosity is estimated at $(1.29 \pm 0.0525) \times 10^{-3}$ m^2/s. To determine the yield stress of the mud, τ_y, a visco-plastic model (see equation 2.1, which describes the Herschel-Buckley model) has been fitted to the data. This yields τ_y =3.31 N/m^2. The fluid mud closely resembles a Bingham fluid ($n \approx 1$).

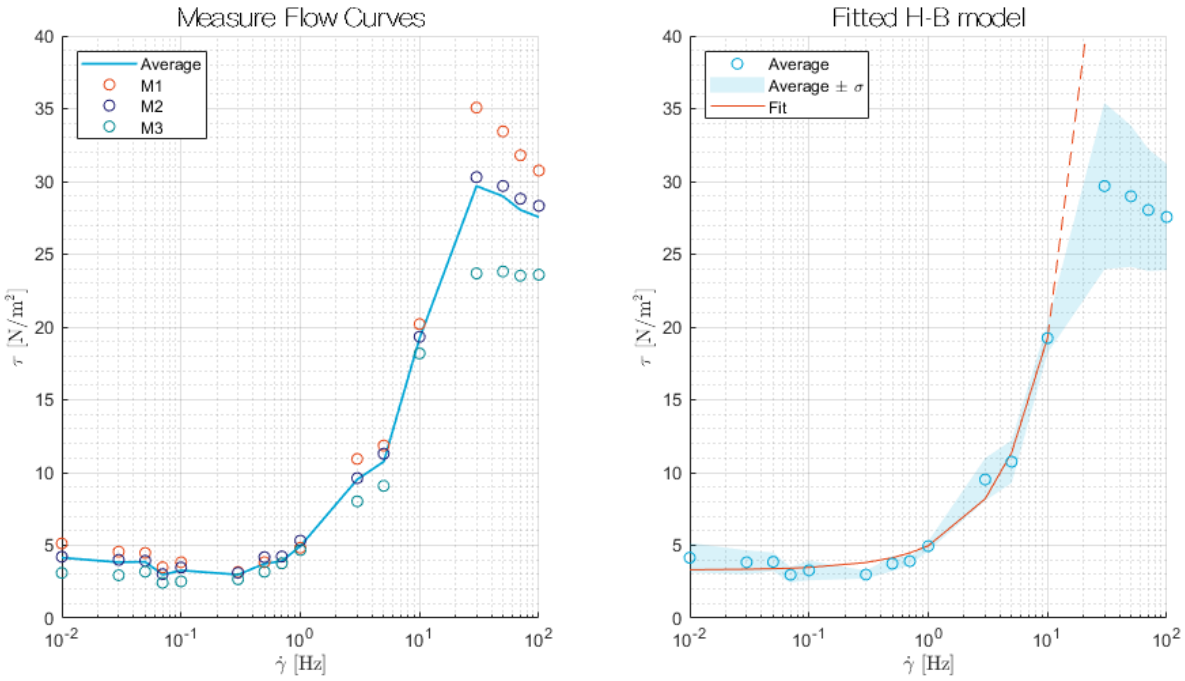

Figure 3.4: Flow curves as measured by Deltares. The left panel shows the measurements (M1,2,3) and the average. M1 is the original sample, M2 and M3 are diluted. The right panel shows the fit of the Herschel-Bulkley model (see equation 2.1, with τ_y = 3.31 N/m^2, K =1.66 Ns$^{0.98}$ and n =0.98. The shaded area shows the standard deviation from the mean of the measurements in the left panel.

3.3. Results

The analysis of the field data has only been performed for the deployment 2019-12-04 at Surodadi (a more elaborate overview of all deployments and the allocation of instruments is given in appendix B). This was the longest deployment during which all instruments were measuring at the same time. The results of the echosounders and the ADVs will not be presented in this chapter. Appendix D will elaborate on the echosounders in further detail. The results from the ADVs were used during the calibration of the wave gauges, presented in appendix C.

3.3.1. Transect Layout

The length of the deployed transect at Surodadi, L, is 150 m. As previously stated, the transect was placed in the dominant wave direction. This direction was estimated based on visual observations. The orientation of the transect is 310° (nautical convention), which is perpendicular to the local coastline (figure 3.5). On a regional scale, the normal to the coastline is orientated 295°.

3.3.2. Wind data

Data on wind velocities and directions during the field campaign was acquired from a measurement station in Semarang (retrieved from Badan Meteorologi Klimatologi Dan Geofisika 2018). This is several kilometres away from the measurement location near Surodadi, which means that the data can only be used as an indication of the velocity and direction of the wind at Surodadi.

In the wind data, a daily pattern can be observed (figure 3.6); in the morning the wind direction is predominantly south-eastern and, around midday, this changes to a northerly direction. When comparing these measurements to the results in table 1.1 (chapter 1, page 2), it is clear that during the morning, the SE monsoon is still dominant. During the afternoon, the sea breeze takes over. This means that, although the field campaign was planned to take place during the NW monsoon, this was not been the case. In general, the velocity of this sea breeze is generally higher than the velocity of the south-eastern monsoon. The direction of the sea breeze is generally between 310° and 320° (figure 3.5), and the direction of the SE monsoon winds is between 130° and 145° (figure 3.5). This means

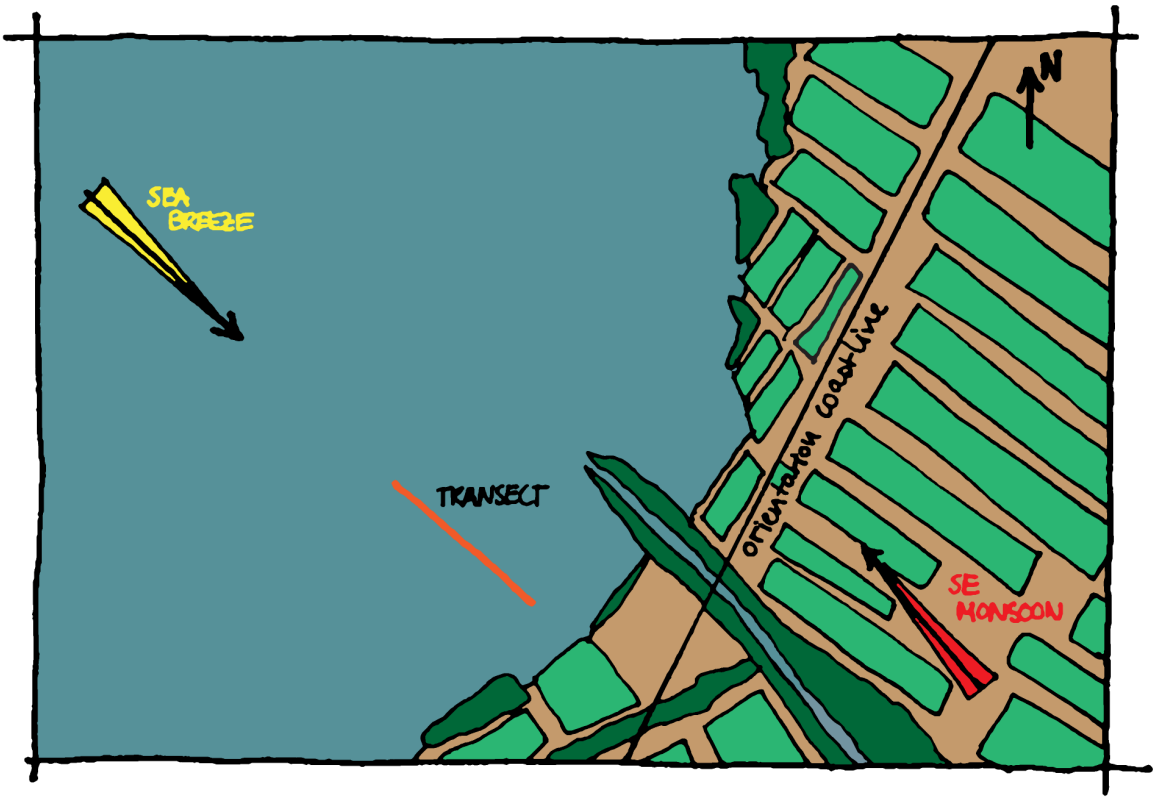

Figure 3.5: Overview of the layout of the measurement transect (orange). The transect is orientated perpendicular to the local coastline, which is 310°. On a more regional scale, the normal to the coastline is 295°. This regional coastline is indicated by the black line. The direction of the wind during the south-eastern monsoon is indicated by the red arrow; the direction of the sea breeze with the yellow arrow. The width of the arrow is an indication of the spread in the direction of the wind.

that the sea breeze is generally in the same direction as the transect or else at a slight angle with the transect. Therefore, wind waves generated by the sea breeze are expected to travel in the direction of the transect as well. For the waves generated by the monsoon winds, the opposite holds; these are expected to travel at a slight angle with the transect in the opposite direction.

3.3.3. Wave parameters

Wave parameters were determined from the data of the wave gauges for every 2048 s (approximately 35 min) of the deployment. For more details on the implemented method, see Appendix C. The wave gauge placed on the seaward pole will be denoted **S**ea**W**ard (SW); the instrument placed on the landward pole **L**and**W**ard (LW). This analysis results in a time series of significant wave heights (H_{m0}), mean wave periods (T_{m01}) and water depths (h_w). To this end, the variance density of the wave amplitude has been determined (figure 3.8), from which the wave parameters can be calculated (appendix C). Due to shoaling, the wave energy and thus the wave height increases over the transect. If this is not taken into account and the damping is directly based on the measured wave height (or energy) at SW, the damping over the transect will be underestimated. A shoaling correction has therefore been applied to the wave data of SW (appendix C), giving $\mathbf{SW_{sc}}$. The difference between the wave height as determined for SW_{sc} and the wave height at LW is assumed to be the wave height dissipated by the viscous fluid mud layer.

The wave height and, more clearly, the wave period, show a daily temporal variability. Comparing this to the daily variability of the wind (figure 3.7), a clear distinction can be made between waves during the sea breeze and waves during the south-east monsoon winds. The waves during the (stronger) sea breeze are generally higher and directed from sea, whereas the south-eastern monsoon winds are directed from land. A fast increase in wave height can be observed after the change to sea breeze,

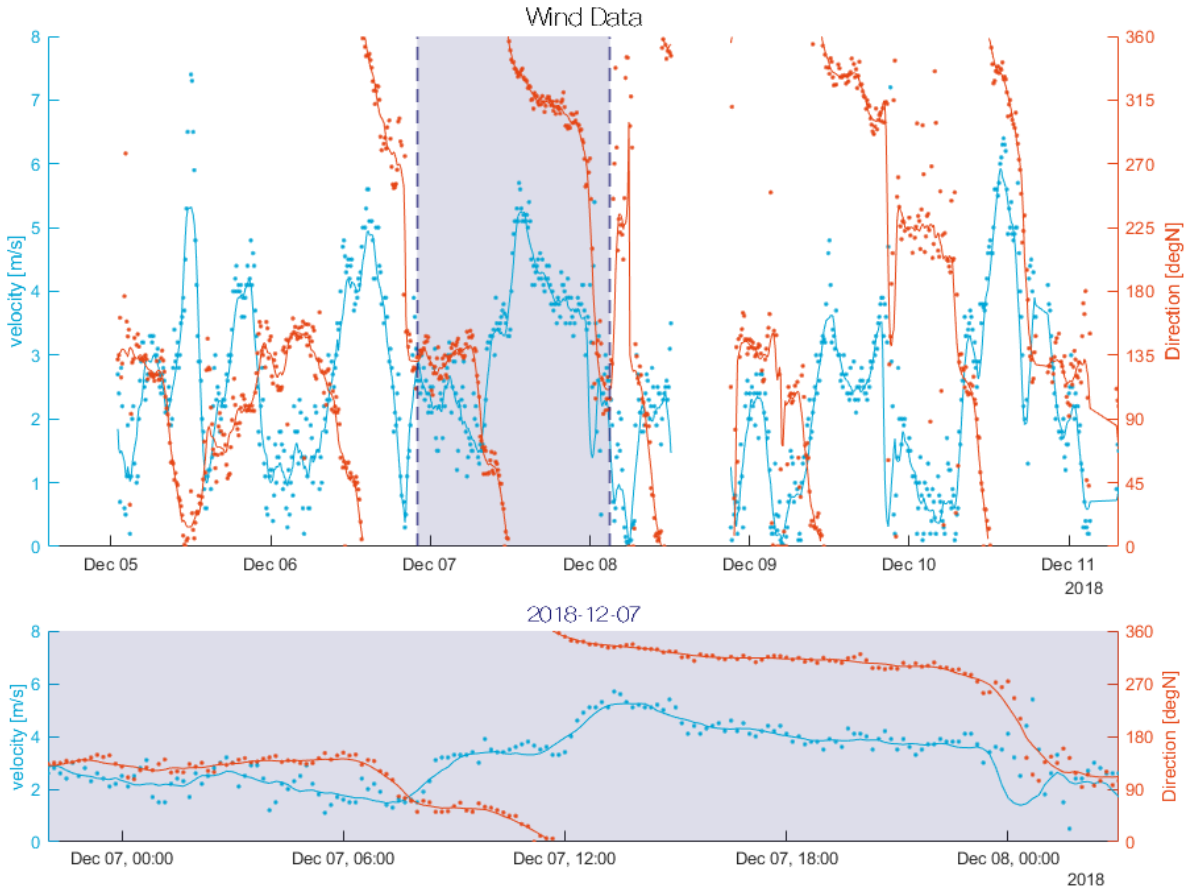

Figure 3.6: Wind data acquired from weather station near Semarang. The upper panel shows the wind velocity and direction during the full 2018-12-04 deployment at Surodadi; the lower panel shows a close-up of this data on 2018-12-07. The wind velocity, shown on the left cyan axis, and the wind direction, shown on the right orange axis, were sampled every 10 mins. Data retrieved from Badan Meteorologi Klimatologi Dan Geofisika (2018).

followed by a more gradual decay when the wind switches back to monsoon winds. Also, the period of the waves during the sea breeze is generally shorter than the period of the waves during the monsoon winds; the first 1-2 s, the latter 3-4 s. As the wave height measured at SW remains larger than the wave measured at LW, it means that waves are still travelling towards the shore although the dominant wind direction is now offshore directed. This is confirmed by the ADV measurements. As the SE monsoon winds originate from land and the transect is located relatively close to shore, the fetch of the wind is too short to generate waves with a significantly large wave height to really impact the analysis. This means that the waves measured during these periods of time originate from a different source than the monsoon winds. The average damping of the waves over the transect is approximately 30%.

The dependency of the hydrodynamics on the prevailing wind is also apparent in the variance density of the surface elevation (figure 3.8). Most energy input occurs during the sea breeze over a large range of frequencies (f =0-1 Hz). The peak frequency decreases over time (or equivalently, the wave period increases). This is characteristic for locally generated wind waves; the longer waves need more time to develop (left panel of figure 3.9). When the wind transitions into the SE monsoon, a double band of approximately equally high variance density can be observed (left panel of figure 3.9). One band around the same frequency as during the sea breeze and one band at a lower frequency. The peak frequency of this lower band increases in time (or equivalently the wave period becomes smaller), rather than the decrease in peak frequency observed during the sea breeze. This double band supports the hypothesis that waves observed during the SE monsoon are not locally generated by these winds. It is more likely that waves that have been generated further offshore by the sea breeze are still propagating into the transect. The waves in the lower frequency band have typical frequencies of offshore generated

swell. Longer waves (with a smaller frequency) travel faster than shorter waves, hence the increase in frequency in this band; the long waves arrive at the transect first, followed by the short waves. It follows from this analysis, that waves generated by the offshore directed monsoon wind are too small to be noticeable in the performed analysis in comparison with the waves generated by the sea breeze and in comparison with the incoming swell. The absolute dissipation of the surface waves (figure 3.10), which is defined as (SW_{sc} - LW), varies largely with frequency. The most absolute dissipation of wave energy occurs for the peak frequencies. The relative damping (figure 3.11), however, shows large dependence on the water depth. A lower water depth leads to a more effective damping. As low water coincides with the sea breeze (and thus the largest input of energy into the system by wind), these waves are damped more effectively than the longer waves travelling into the transect during the SE monsoon winds.

For waves propagating over a fluid mud layer, it can be assumed that their damping can be estimated according to equation (3.1) (Gade, 1958). The parameter k_i, which is the imaginary part of the wave number k, is a measure for the rate of damping per meter travelled (figure 3.7) and L is the length of the transect. When the water depth is constant and the mud layer is horizontally homogeneous, this parameter is constant over the length of the transect. At the location of the measurements, however, the water depth is not constant and thus the first assumption does not hold. The value calculated here is therefore an indicator for the average damping over the length of the transect. It can be seen that, for lower water depths, this damping coefficient becomes larger, which means that the damping in the viscous mud layer is more effective.

$$H_{LW} = H_{SW_{sc}} e^{-k_i L} \tag{3.1}$$

3.3.4. Mud floaters

The results of the measurements using mud floaters were analysed for the period 2018-12-01 until 2018-12-11 at Surodadi. The displacement of the mudfloaters is in the order of a few centimetres (table 3.2). As stated in section 3.2.4, the measurement error was expected to be close to the measured quantities. The actual measurements show that this is indeed the case. It is therefore assumed that there was no measurable transport of mud within the fluid mud layer during the relatively mild wave conditions in the measurement campaign.

location	depth [cm]	Floater 1 [cm]	Floater 2 [cm]	Floater 3 [cm]	Floater 4 [cm]	Average [cm]
LW	10	0	0	1	14	4.5
LW	30	1	0	1	2	1.3
SW	10	3	0	4	0	3.5
SW	30	1	1	1	1	0

Table 3.2: Absolute displacements of mud floaters at landward (LW) and seaward measurement pole (SW) over a period of 10 days. The direction of movement has not been taken into account due to the large measurement error. The result of the measurement displayed in cyan is considered an outlier.

3.3.5. Level of the Mud-Water Interface and the Bottom

Figure 3.12 shows the bathymetry along the transect at two moments during the deployment at Surodadi. As the water level during the two measurements was different, the bathymetries in figure 3.12 have been corrected for this by matching the water levels at LW. On the basis of both measurements and the experiences in the field, it is estimated that, averaged over the transect, the fluid mud layer is approximately 0.5 m thick. The slope of the fluid mud interface is crudely estimated from these measurements to be 1.83×10^{-3} [m/m].

The level defined as 'bottom' in section 3.2.5 is ambiguous. The form of the consolidated bottom is in both bathymetries recognisable; the exact levels, however, differ. This is due to the measurement method; the same force can never be exerted by hand during every measurement. Furthermore, the

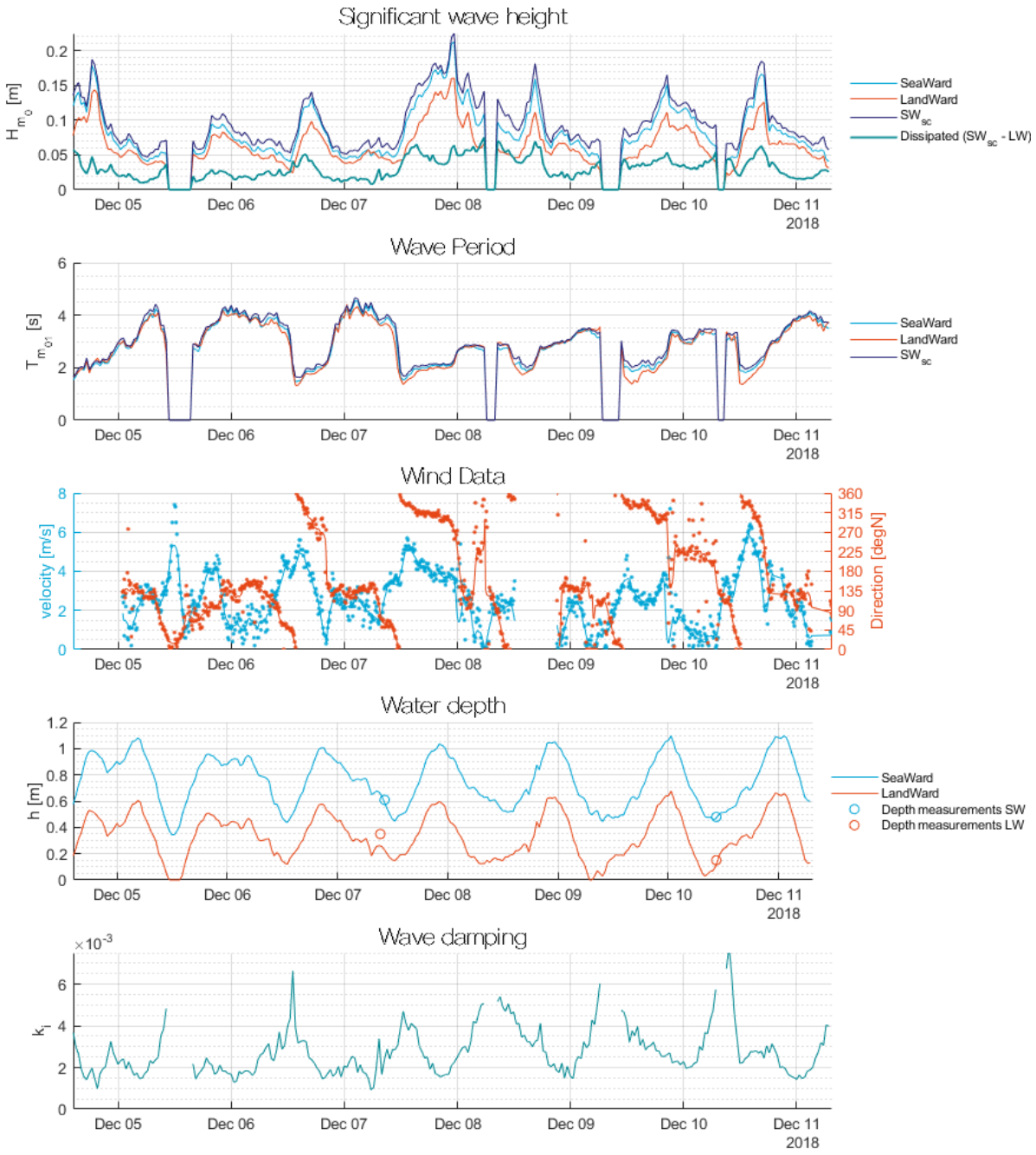

Figure 3.7: Wave parameters determined from spectral analysis. The top panel shows the significant wave height H_{m_0}. The second panel shows the wave period $T_{m_{01}}$. The third panel shows the wind data (velocity on left axis, direction on right axis). The fourth panel shows the water level during the deployment. The lower panel shows the relative damping k_i. SW denotes the wave gauge at the seaward measurement pole, SW$_{sc}$ the same measurements after correction for shoaling. LW denotes the wave gauge at the landward measurement pole. In the top panel, the difference between SW$_{sc}$ and LW is assumed to be the dissipated wave height by the viscous fluid mud layer. The gaps in the data are either caused by a water level under sensor elevation at LW or by too large a ratio between wave height and water depth, indicating wave breaking might have occurred.

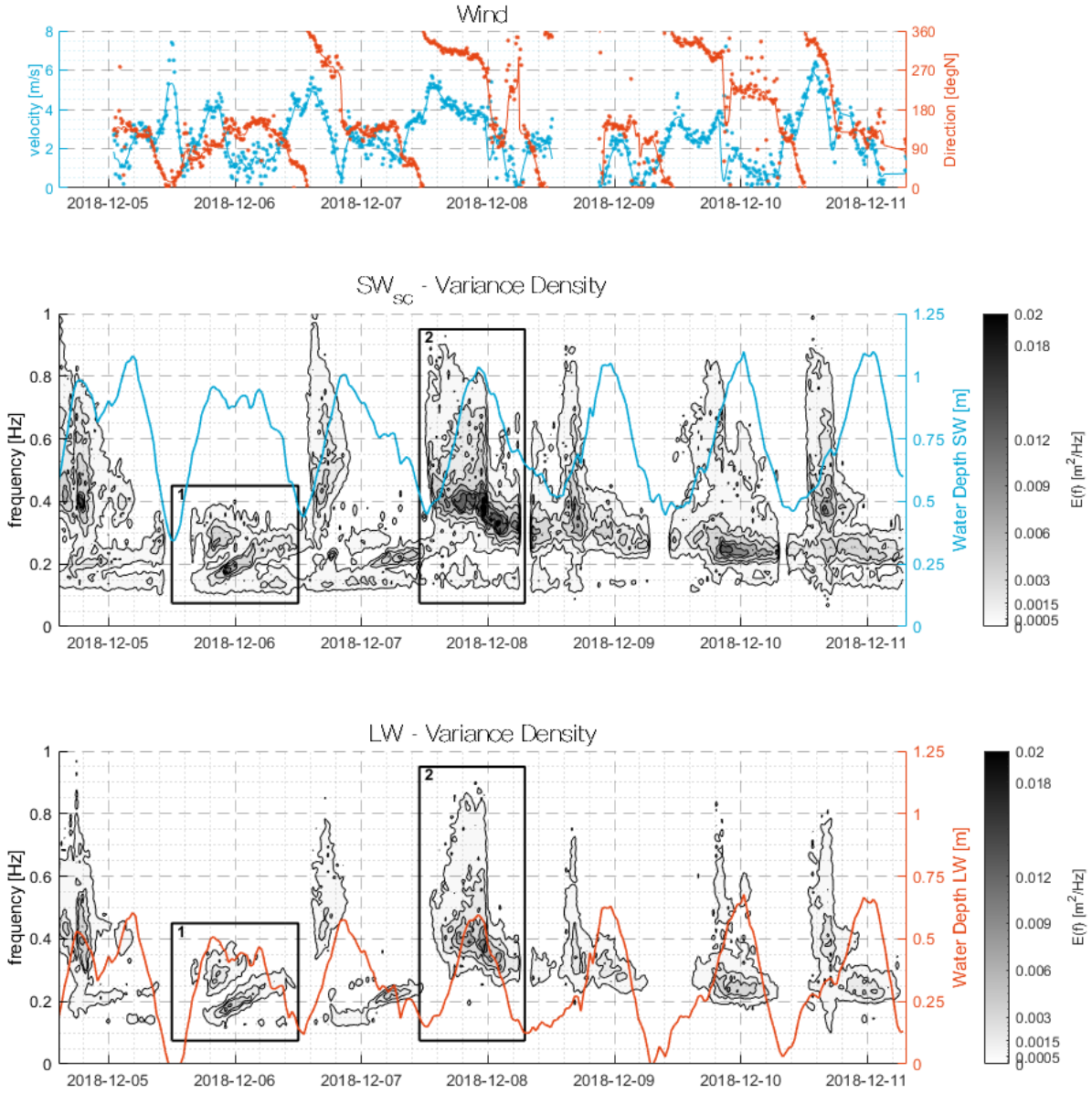

Figure 3.8: Wave spectra obtained by spectral analysis. The upper panel shows the wind data obtained from the station at Semarang (velocity on left axis, direction on right axis). The middle panel shows the evolution of the variance density per frequency over time at SW, the lower panel at LW. The lines in these panels indicate the water depth at these particular measurement poles (right axis). The parts of the time series indicated by frames 1 and 2 have been displayed in more detail in figure 3.9. The ticks on the colourbars correspond to the values of the isolines in the figure.

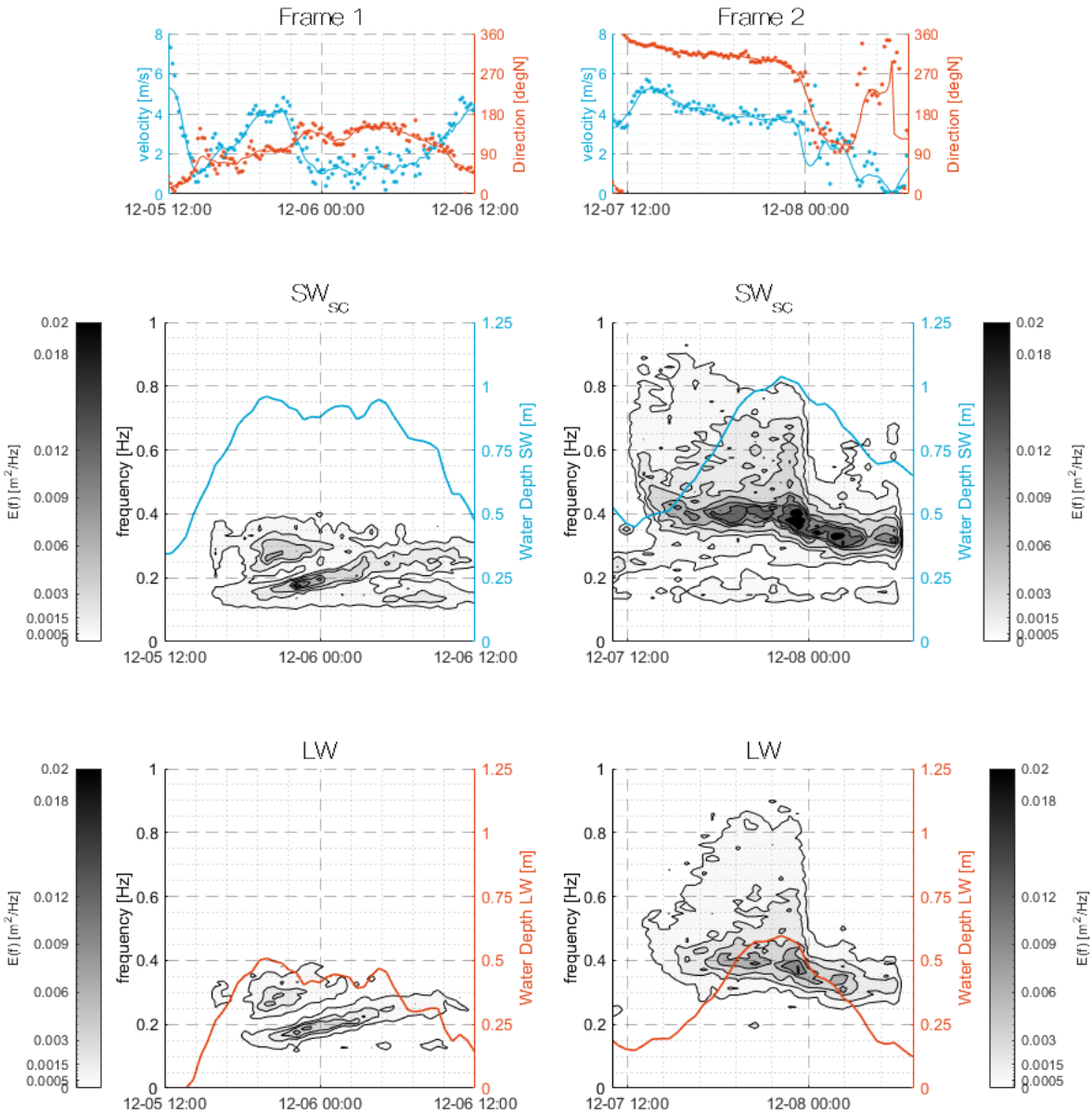

Figure 3.9: Detailed display of frames 1 and 2 indicated in figure 3.8, in the left and right column respectively. The upper panel shows the wind data obtained from the station at Semarang (velocity on left axis, direction on right axis). The middle panels show the evolution of the variance density per frequency over time at SW and the lower panels at LW. The ticks on the colourbars correspond to the values of the isolines in the figure.

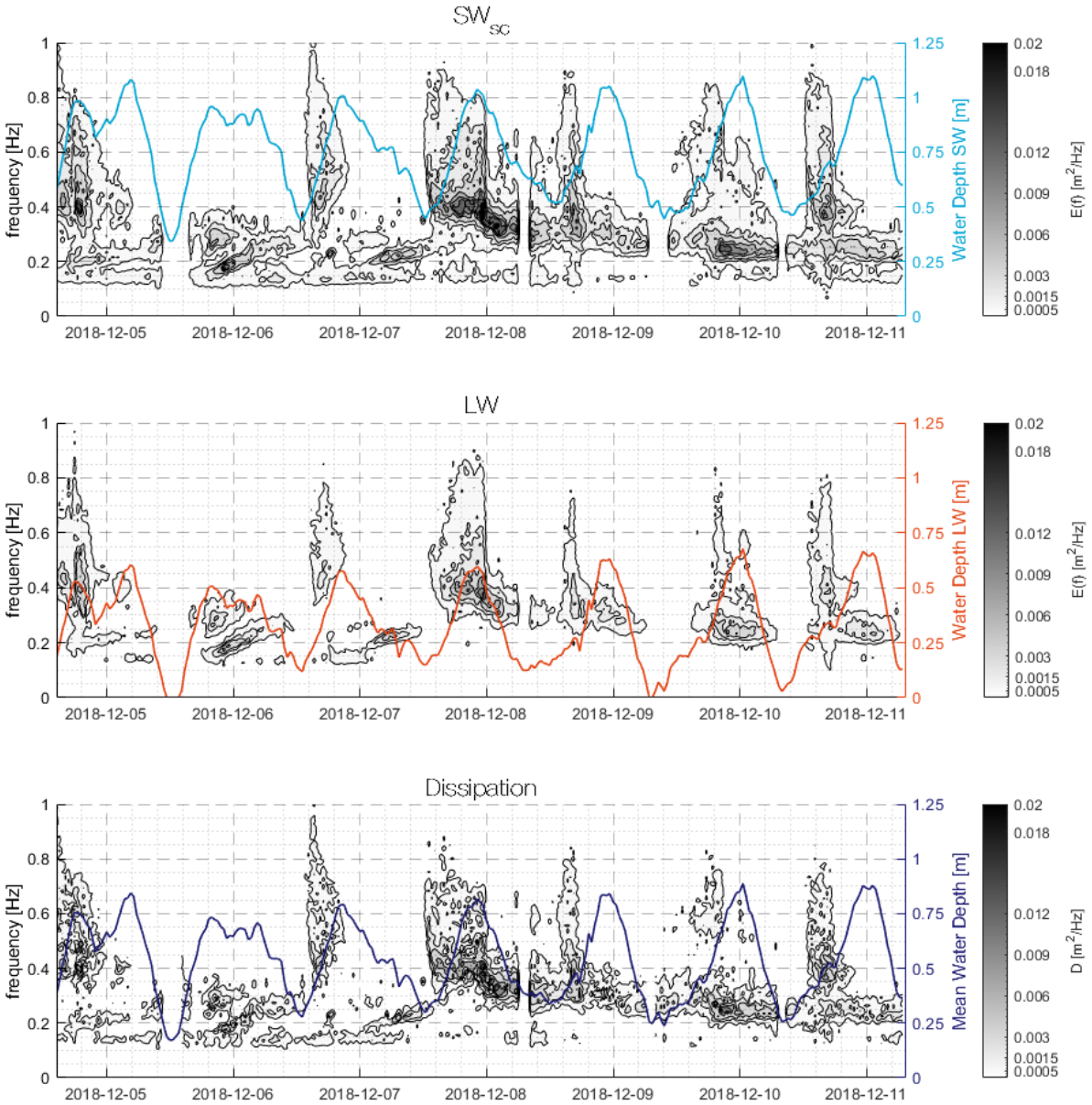

Figure 3.10: Evolution of the variance density per frequency over time during deployment 2018-12-04 at Surodadi. The two upper panels show the evolution of the variance density of the surface elevation over time for SW_{sc} and LW. The lower panel shows the evolution of the dissipation. The lines in the upper two panels indicate the water depth at these particular measurement poles (right axis); the line in the lower panel indicates the mean water depth over the transect. The ticks on the colourbars correspond to values of the isolines in the figure.

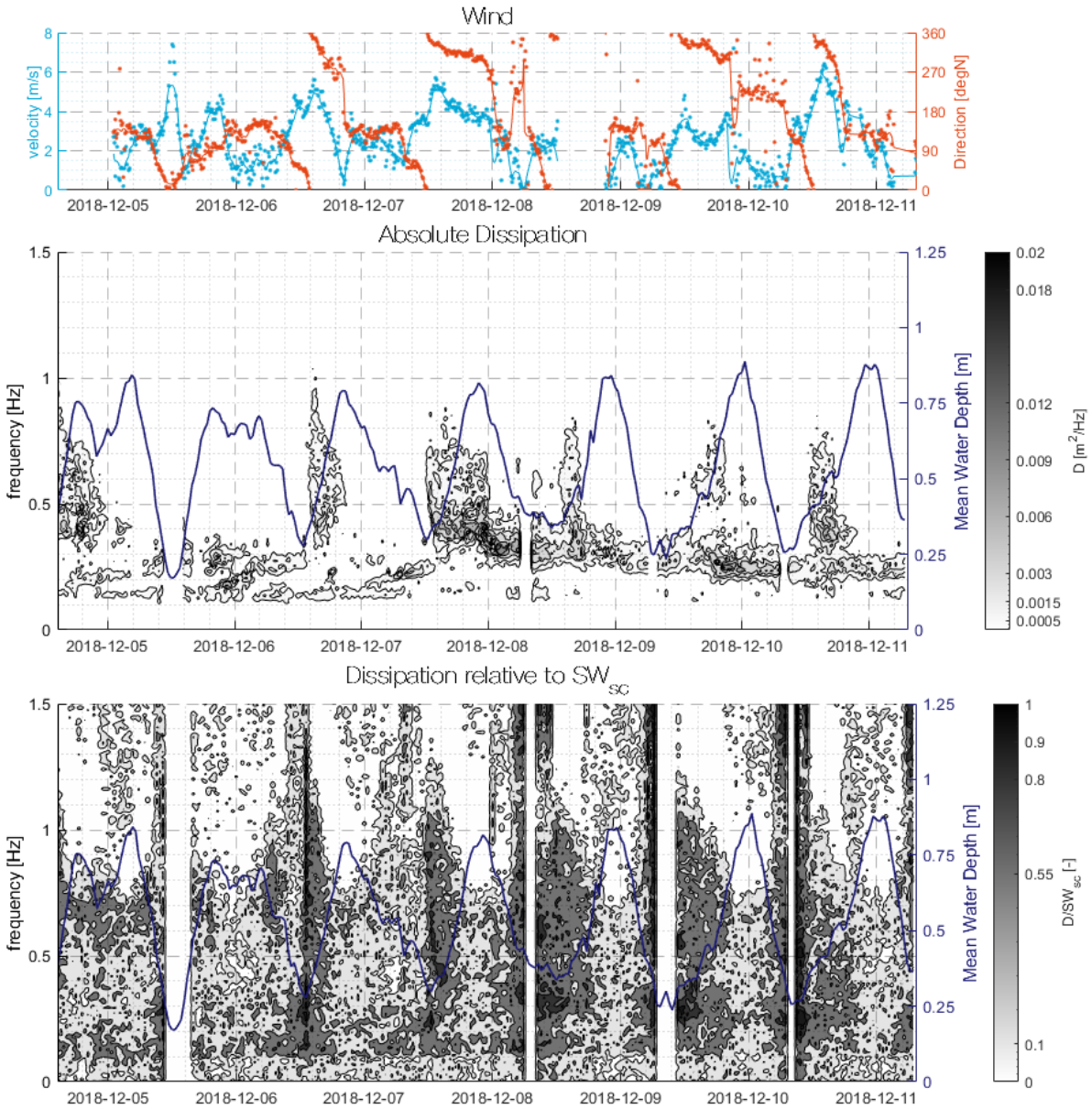

Figure 3.11: Evolution of the dissipation over time during deployment 2018-12-04 at Surodadi, expressed in terms of the variance density per frequency. The upper panel shows the wind data obtained from the station at Semarang (velocity on left axis, direction on right axis). The two lower panels show the evolution of the absolute dissipation and dissipation relative to the shoaling corrected energy at SW. The lines in the lower panels indicate the mean water depth over the transect. The ticks on the colourbars correspond to the values of the isolines in the figure.

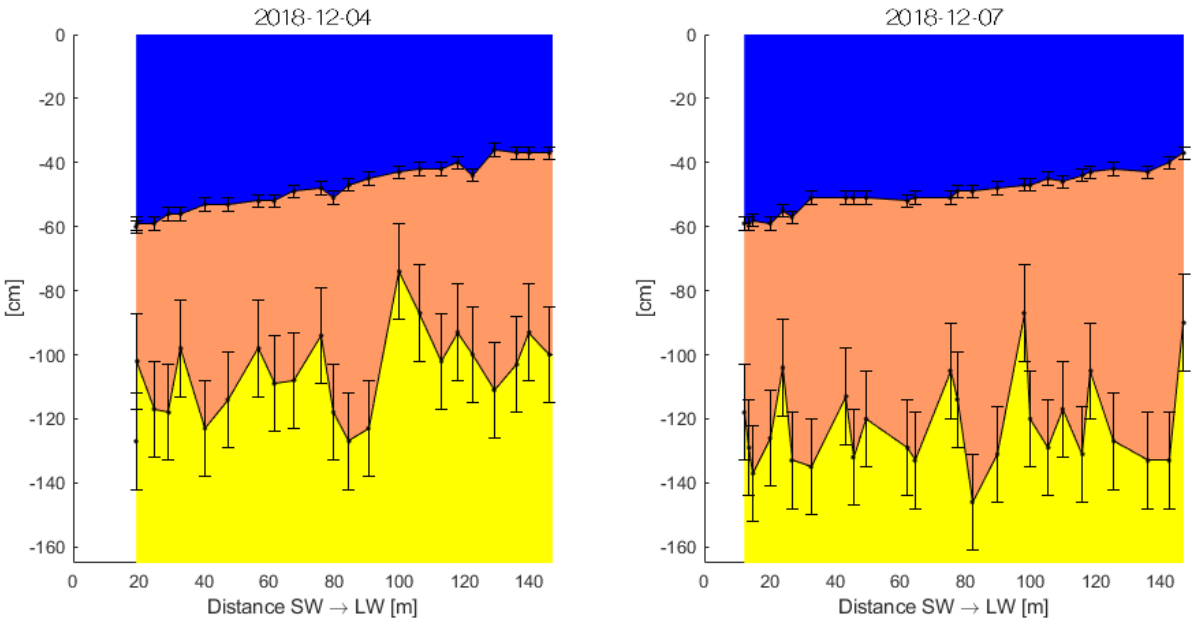

Figure 3.12: Bathymetry along the transect at 2018-12-04 and 2018-12-07. Blue denotes water, brown fluid mud and yellow is the consolidated bottom. x = 0 denotes the location of SW, x = 147 denotes the location of LW. Not enough data was available to determine the bathymetry in the first seaward meters. The error bars indicate the estimated error in the measurements.

mud characteristics are not homogeneously distributed horizontally and vertically and therefore the resistance is different at every measurement point. As the measurements were not taken at the exact same locations in the different bathymetries (and the measurement error in the GPS was in the order of 2 metres), the measurements points have been projected onto the transect. The measured level of this interface, therefore, contains a large uncertainty. Also, the mud near this bottom is already consolidating beyond the range in which it can be called fluid mud. The mud-water interface was measured with significantly less uncertainty and shows the same trend and gradient in both bathymetries.

3.4. Conclusion

The observations suggest a slope of the fluid mud interface of 1.83×10^{-3}. At the same time, a reduction in the energy of the waves travelling over the fluid mud is observed without the actual breaking of waves as a possible dissipation mechanism. This indicates that the damping of waves by fluid mud is indeed a feature of this coastal system.

In the wind data as well as the wave data (predominantly the wave periods), a strong daily pattern can be observed, connected to the south-eastern monsoon winds and the sea breeze. The waves during the sea breeze are locally generated waves and are therefore shorter. The dominant waves during the south-eastern monsoon are generally swell waves generated offshore. More energy input into the system occurs during the sea breeze. The absolute dissipation varies largely with frequency, while the relative dissipation also shows dependence on the water depth. For shallower water depths, the relative dissipation increases. During these relatively calm conditions, no measurable transport of mud towards the coast has occurred in the transect. The deviation of both the measured slopes from the mean value is small and as the bathymetries were taken a few days apart, the slope of the mud layer is not expected to differ significantly over time.

4

Modelling wave-mud interaction

As stated in chapter 3, the purpose of the SWAN-Mud model is to be able to assess the response of fluid mud to characteristic events at the coast of Demak. The model set-up is based on the conditions of the measurement campaign as described in chapter 3 and the results of these measurements will be used to validate the model. In order to predict whether mud streaming might be of importance and under what conditions this may be, the results of the SWAN-Mud model will be used to calculate the potential set-up of the mud-water interface, for the field conditions and hypothetical extreme conditions.

In section 4.1, the model schematisation and set up is presented. This model schematisation is calibrated with the data measured during the field campaign in section 4.2, after which this calibration is validated. In section 4.3, an algorithm is presented to provide an indication of the slope that can be sustained by the wave damping calculated by SWAN-Mud. The calibrated model is then used in combination with this algorithm to make a predication for storm conditions in section 4.4.

4.1. Schematisation and Model Set-Up

As the measurements (described in chapter 3) have been done in a single transect orientated in approximately the mean wave direction, it is chosen to approach the schematisation from a one-dimensional perspective (figure 4.1). The modelled transect has a length of 150 m and contains 150 grid cells, hence Δx =1 m. The first gridpoint is therefore assumed to represent SW and the last gridpoint LW (see chapter 3). The free surface level is assumed to be horizontal. As measurements show that the water depth reduces towards the coast, this has been implemented in the model by means of a gradient in the mud-water interface. The thickness of the mud layer, h_m, is assumed to be constant over the transect (based on the results presented in section 3.3.5). Unless stated otherwise, other nearshore processes than the wave damping by fluid mud have been switched off, as well as the option for bottom friction. The dispersion relation used to model the damping by the fluid mud is the relation implemented by Kranenburg et al. (2011). The density of water is assumed to be ρ_w =1020 kg/m^3, the density of mud is assumed to be ρ_m =1200 kg/m^3 based on the measurements by Deltares (section 3.2.6), unless stated otherwise. All other parameters have been set to default.

4.2. Model Validation

To validate the model and to gain insight into the sensitivity of the model to changes in the mud layer thickness, h_m, the viscosity, ν_m, and density, ρ_m, a multi-step approach has been adopted. Rogers and Holland (2009), as well as Kranenburg et al. (2011), already note that uncertainty in the first two of these parameters is of particular importance for the outcome of the model.

The wave input of the model is based on the results from the measurement campaign as presented in chapter 3. The choice has been made to take hydrodynamic parameters as determined at 2018-12-07 23:19:28 (local time; UTC+7) as a reference. At this point in time during the field campaign, the highest significant wave height was measured and this case is assumed to be representative for the Sea

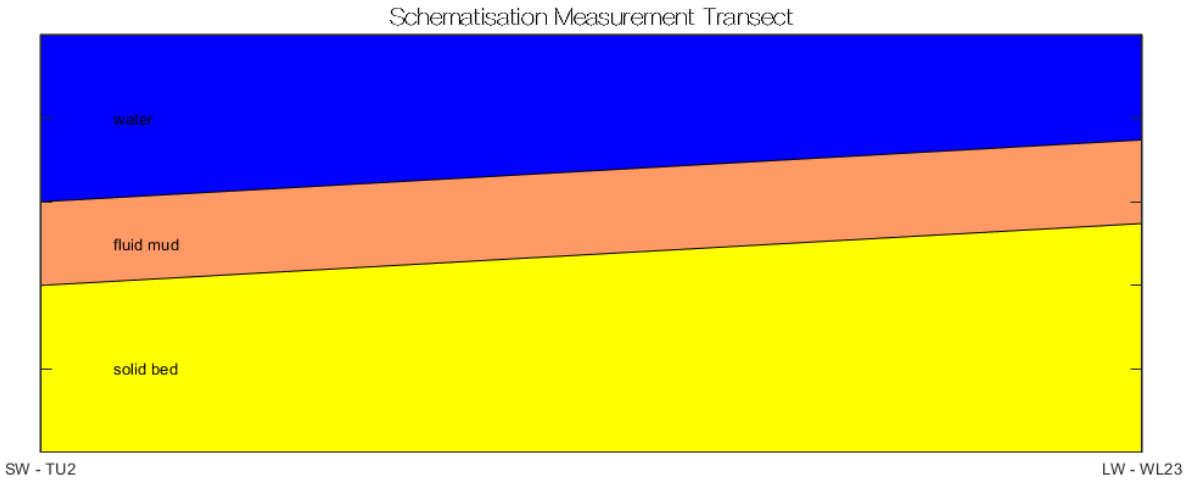

Figure 4.1: Schematisation of the measurement transect in SWAN-Mud.

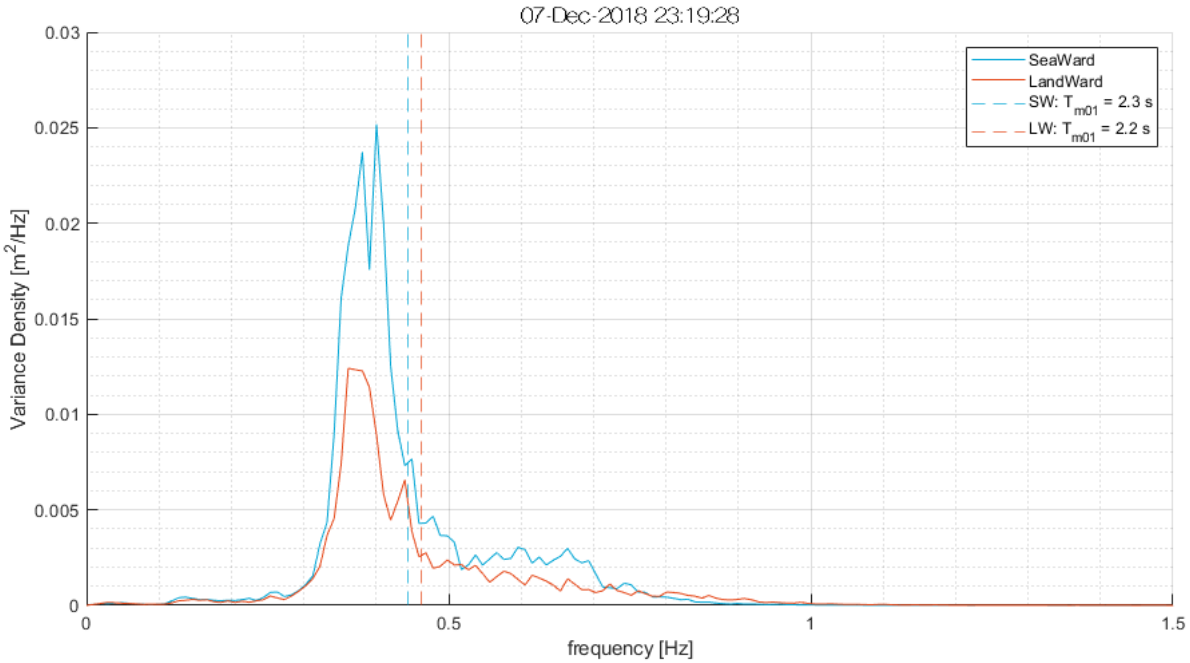

Figure 4.2: Variance density spectrum at 2018-12-07 23:19:28 (UTC+7). SW will be used as wave input to the SWAN-Mud model. The outcome of the model will be compared to LW.

Breeze wave regime (figure 4.2). The corresponding significant wave height is $H_{m0} = 0.21$ m and the wave period $T_{m01} = 2.3$ s. Because the viscous dissipation by mud is also highly dependent on the water depth (see for example Rogers and Holland (2009)), the implemented water depth is equal to water depth measured at the same time as the wave characteristics; hence 1.01 m at SW and 0.56 m at LW.

The validation of the model has been performed as follows;

Step 1 First, simulations have been run without any fluid mud. This was to verify that bottom friction is unable to reproduce the observed damping of waves. The standard formulation in SWAN-Mud for bottom friction has been used; the JONSWAP bottom friction formulation.

Step 2 The model is calibrated to achieve the same wave damping as observed in the field, using a monochromatic wave with the characteristics of the reference case. The main calibration parameters are the thickness of the mud layer, h_m, and the viscosity of the mud, ν_m.

Step 3 The sensitivity of the damping to changes in the mud layer thickness h_m, the viscosity ν_m, the density ρ_m and the water depth h_w is assessed, using a monochromatic wave with the characteristics of the reference case.

Step 4 As shown by Kranenburg et al. (2011), wave damping is also spectrally distributed and dependent on frequency. Therefore, instead of using a monochromatic wave, the model is forced using the measured variance density spectrum of the reference case (figure 4.2). With these results, the validity of a monochromatic wave is assessed as forcing of the model.

Step 5 The calibrated model will be validated with a time-series of wave conditions - both using monochromatic waves and variance density spectra as wave input.

4.2.1. Step 1: No Mud

Two simulations have been done without the mud damping to verify that normal bottom friction is unable to reproduce the observed damping of waves. The first simulation uses the default JONSWAP bottom friction coefficient $C_b = 0.038$ m^2/s^{-3} (Vledder et al., 2011). For the second simulation, this friction coefficient has been calibrated to give the same damping as measured during the field campaign.

The wave height measured at LW is $H_{m0} = 0.195$ m in the case of the standard friction coefficient (figure 4.3). The damping by the bottom friction is clearly smaller than the observed damping. To achieve the same reduction in wave height, a friction coefficient of $C_b = 0.0963$ m^2/s^{-3} needs to be used. This is contradictory to expectation. The standard value of $C_b = 0.038$ m^2/s^{-3} is calibrated as a best fit with measurements of various different sources. In some of these sources, larger bedforms play a role, like ripples or (anti)dunes. These induce more drag on the flow and hence increase the friction factor C_b. In case of a muddy bed, these bed forms are absent. Therefore, C_b is expected to be lower than the standard value. Furthermore, Vledder et al. (2011) found that the standard value of 0.038 m^2/s^{-3} is applicable to a wide range of bottom materials as well as to both wind waves and swell. The bottom friction coefficient, which is needed to reproduce the observed damping, deviates strongly from this standard value. This indicates that a different mechanism is responsible for the dissipation of wave energy at the coast of Demak. It is therefore unlikely that the damping of the waves measured during the field campaign was caused by bottom friction.

4.2.2. Step 2: Calibration

The viscosity determined from the samples by Deltares was 1.29×10^{-3} m^2/s, the density 1200 kg/m^3(section 3.2.6). To achieve the same damping as measured in the field, a fluid mud layer of 0.93 m is required. Based on the measured bathymetry (see section 3.3.5) and other observations during the field campaign, this number seems to be rather high. A mud layer thickness of 0.5 m seems more applicable and is therefore used in conjunction with a density of 1200 kg/m^3. The required viscosity to achieve the measured damping is 5.47×10^{-4} m^2/s. This combination of parameters will be referred to as the reference case.

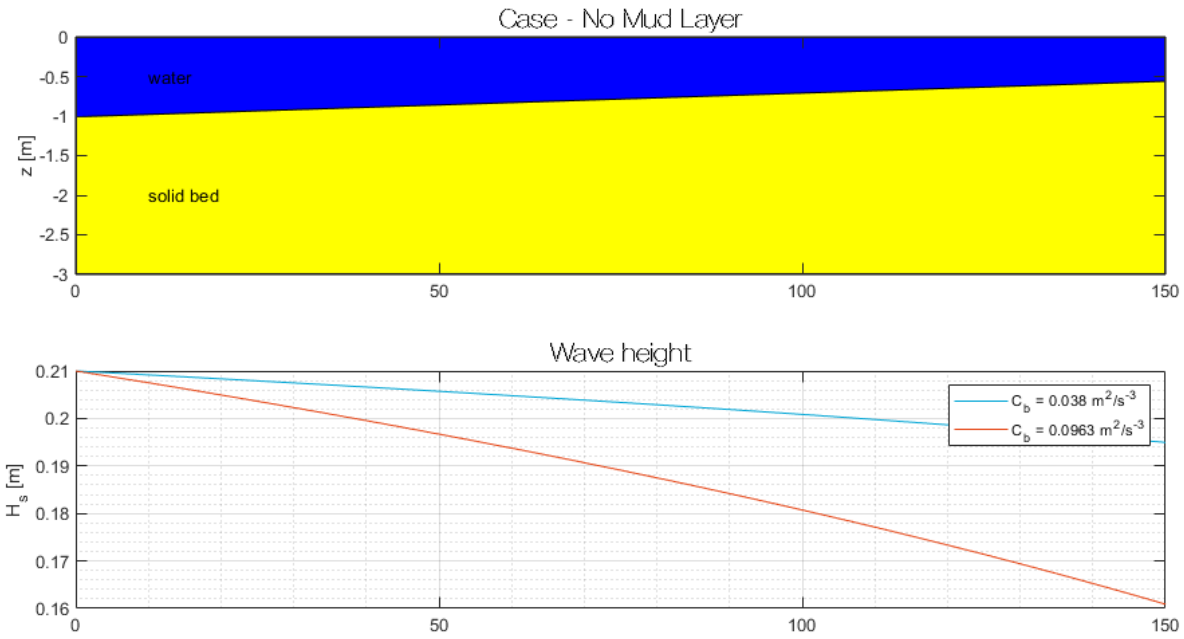

Figure 4.3: Results using the JONSWAP bottom friction formulation in the absence of a fluid mud layer. The top panel shows the used schematisation, the bottom panel the development of the wave height over the transect for C_b = 0.038 m^2/s^{-3} (cyan) and C_b =0.0963 m^2/s^{-3} (orange).

The imaginary part of the wave number, k_i, increases towards the shore (figure 4.4). This is related to the negative gradient in water depth in the direction of the shore. A larger depth results in smaller velocities at the interface between mud and water, hence less energy can be transferred to the viscous mud layer. This means less energy damping can take place. An estimate of the average damping coefficient is made using equation (3.1), which results in $k_i = 2.12\times10^{-3}$. As mentioned in section 3.3.3, for the calculation of k_i the shoaling corrected wave height at SW is used.

4.2.3. Step 3: Sensitivity of Parameters

To assess the sensitivity of the model, SWAN-Mud was run for a range of combinations of layer thicknesses and viscosities for the chosen density ρ_m = 1200 kg/m^3. The layer thickness, h_m, was varied from 0.01 m to 1.0 m linearly in 100 equal steps. The viscosity ν_m was varied logarithmically from 1×10^{-5} m^2/s to 1×10^{-1} m^2/s in 100 steps as well. This gives 10,000 combinations.

From this set of results, the damping for each combination of parameters was determined. It is expected that multiple sets of parameters can be found that lead to the same amount of damping of the surface wave. This is confirmed by the results of the simulations. For the full range of mud layer thicknesses, a combination with a certain viscosity could be found such that the model gives the same amount of damping as observed in the field (figure 4.5). These viscosities are within the range of 1.1×10^{-4} m^2/s to 1.5×10^{-3} m^2/s, which are lower values than expected based on the viscosity determined from the mud samples. In general, a larger viscosity will give more damping, as will a thinner mud layer. This means that if the mud layer is assumed to be thinner, a smaller viscosity needs to be chosen to achieve the same amount of damping.

Varying mud layer thickness and viscosity

To simplify the analysis, four cases have been selected that deviate from the reference case in either the mud layer thickness or the viscosities. These combinations have been summarised in table 4.1 (case 1 to 4). The sensitivity to a deviation in thickness from the reference case is largest in the range of $\nu_m = 5.0\times10^{-4}$ m^2/s to $\nu_m = 5.0\times10^{-3}$ m^2/s (figure 4.6, middle row, left panel). The relative response of the model to a change in viscosity is of the same order of magnitude for all considered mud layer thicknesses (figure 4.6, middle row, right panel). The response to a change in viscosity or mud layer

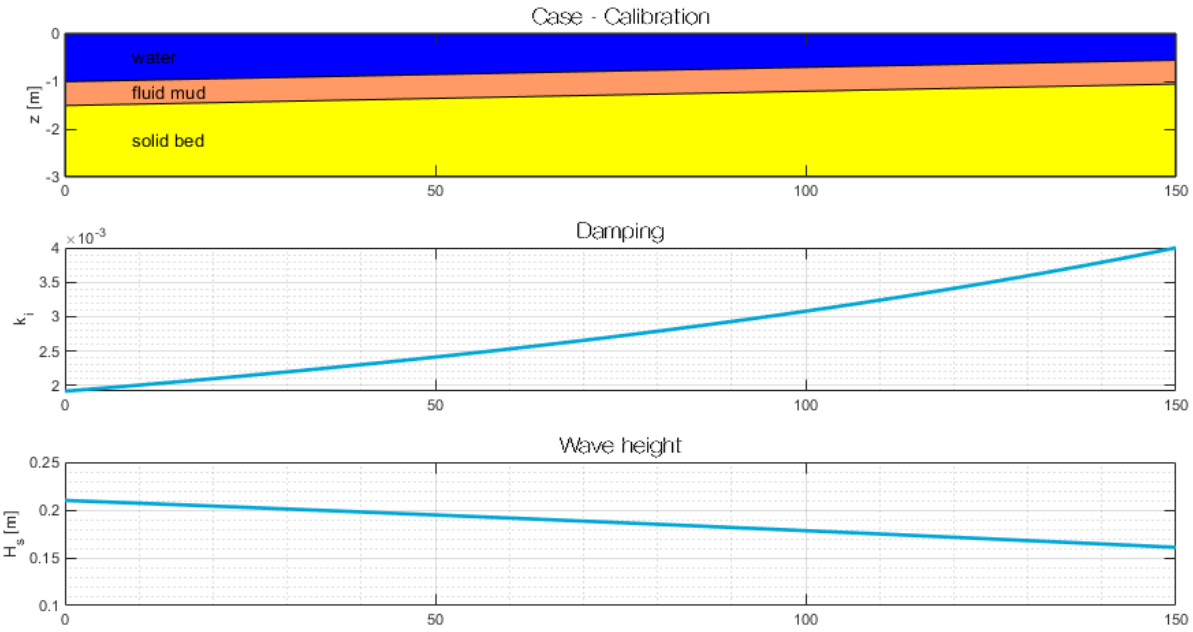

Figure 4.4: Result of the calibration of the SWAN-Mud model, based on a mud thickness of h_m = 0.5 m. The top panel shows the used schematisation, the middle panel the development of the imaginary part of the wave number over the transect and the bottom panel the development of the wave height over the transect.

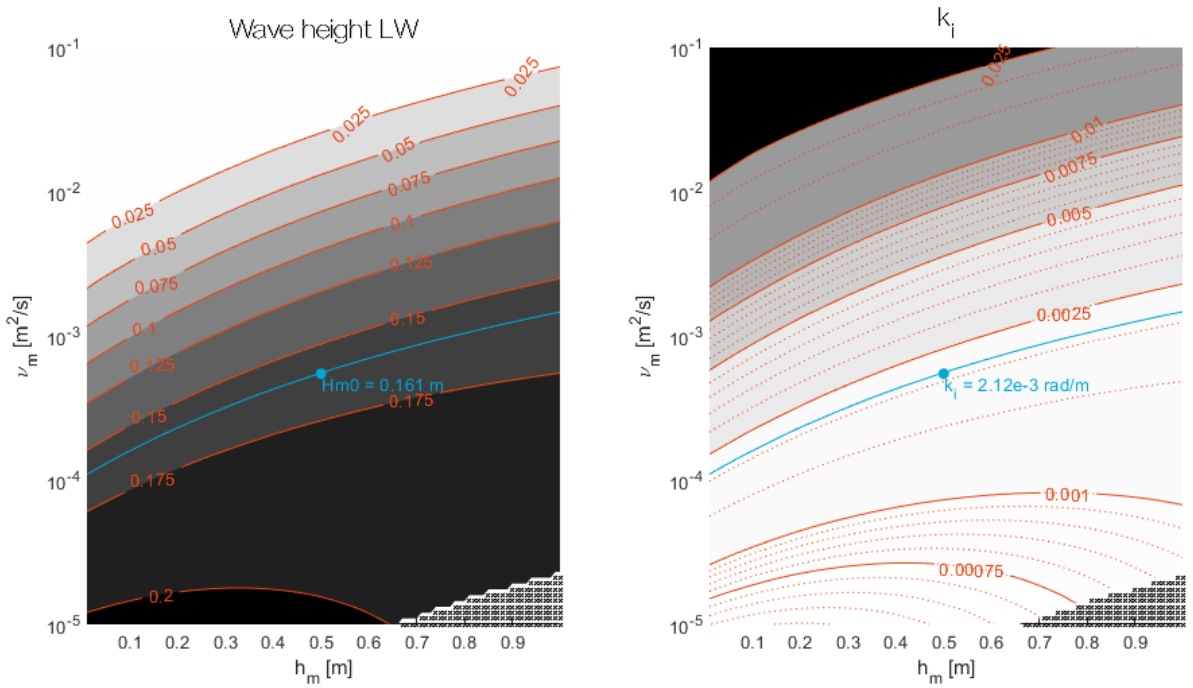

Figure 4.5: Result of the sensitivity runs of the SWAN-Mud model, for ρ_m = 1200 kg/m^3. The left panel shows the wave height at LW, the right panel shows the imaginary part of the wave number k_i. In both plots the cyan line denotes all possible combinations of h_m and ν_m that give H_{m0} = 0.161 m and k_i = 2.12×10^{-3} respectively. The dot indicates the reference case. Crosses denote combinations where SWAN-Mud would not give a physically sound outcome.

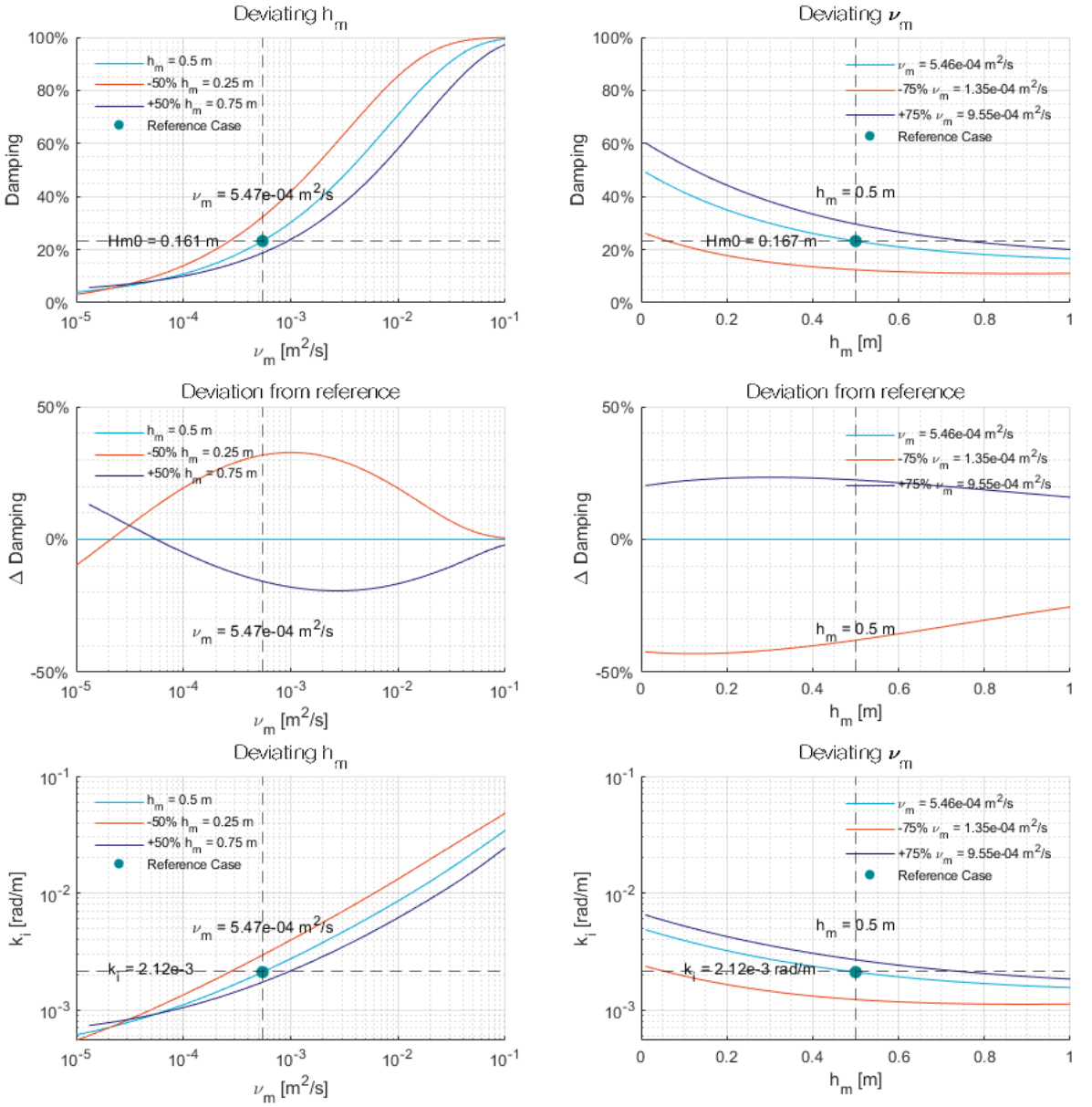

Figure 4.6: Results for the sensitivity analysis on Case 1 to 4. The upper two panels show the percentage of wave height damped for various values of h_m (left) and ν_s (right). The middle two panels show the relative deviation of these cases from the reference case. The lower two panels show the imaginary part of the wave number k_i.

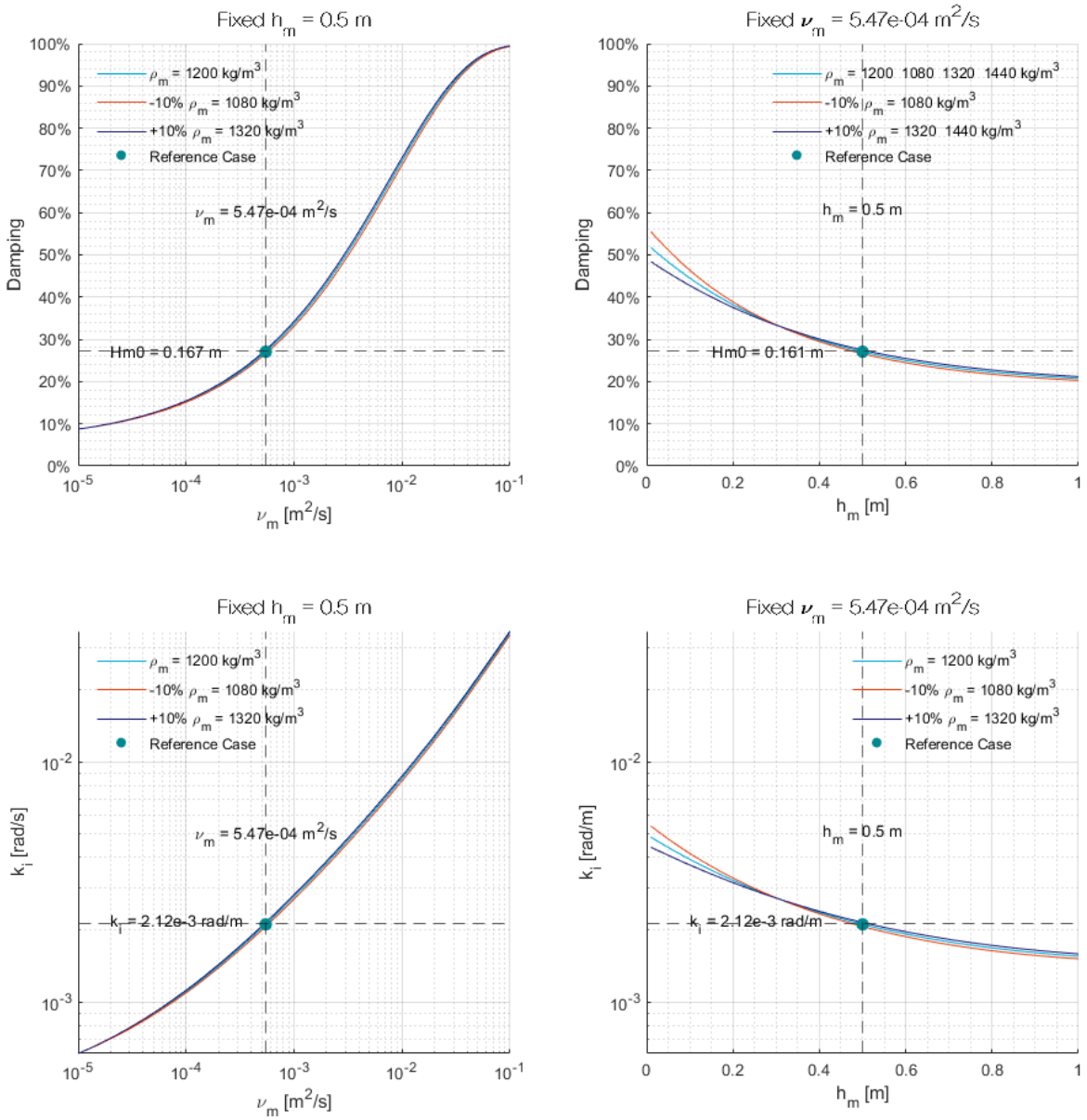

Figure 4.7: Results for the sensitivity analysis on Case 5 and 6 (variation in density). The upper right panel shows the percentage of wave height damped for a fixed h_m and a varying ν_m. The upper right panel shows the same, however h_m is varying and ν_m is fixed. The lower two panels show the imaginary part of the wave number against the same parameters respectively.

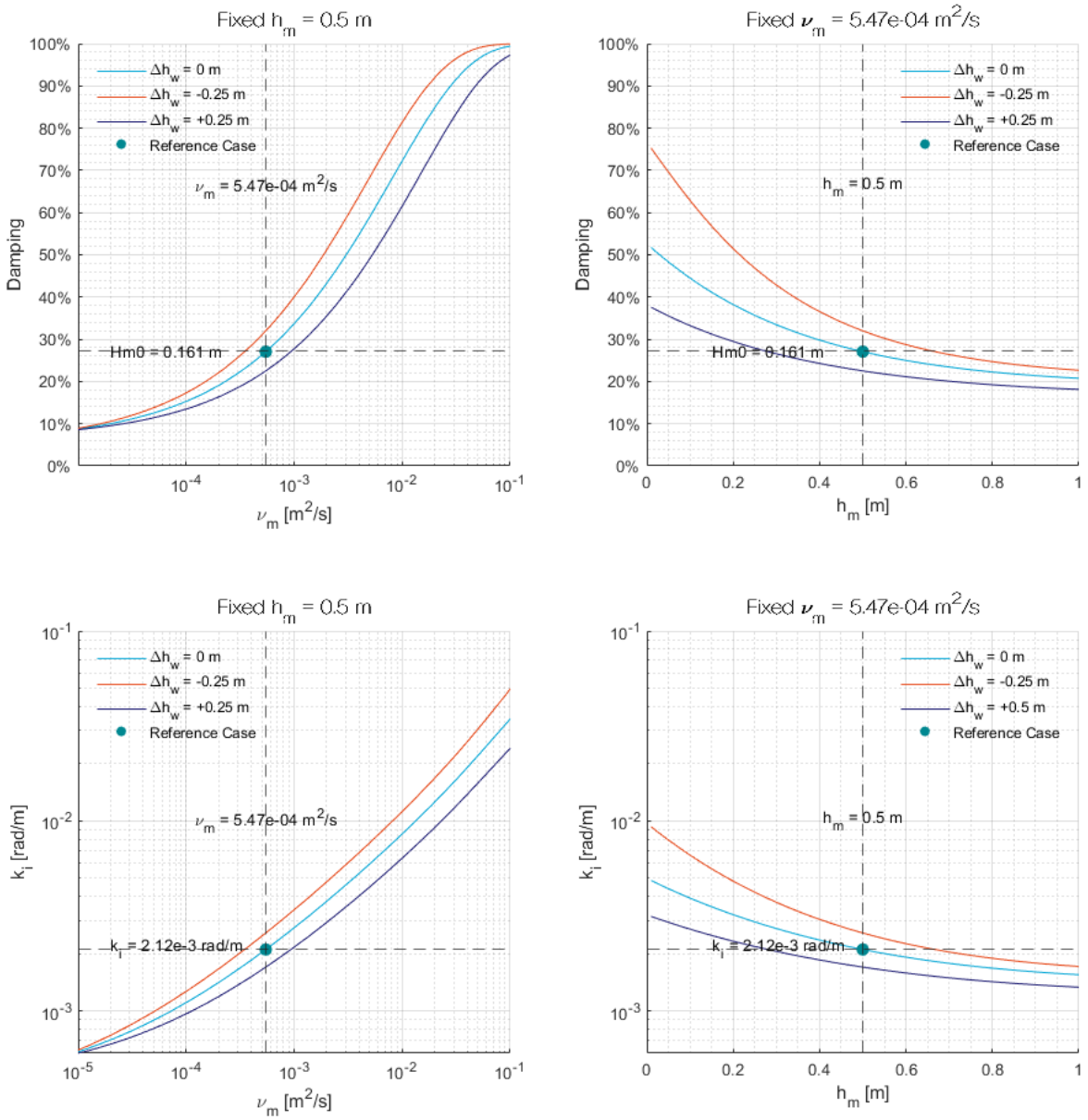

Figure 4.8: Results for the sensitivity analysis on Case 7 and 8 (variation in water depth). The upper right panel shows the percentage of wave height damped for a fixed h_m and a varying ν_m. The upper right panel shows the same, however h_m is varying and ν_m is fixed. The lower two panels show the imaginary part of the wave number against the same parameters respectively.

thickness is in both cases strongly non-linear. A reduction in viscosity gives a larger change in damping than an increase in viscosity. A reduction of the mud layer thickness shows a larger change in damping as well.

Case	h_m	ν_m	ρ_m	h_w
1	-50%	0%	0%	0 cm
2	+50%	0%	0%	0 cm
3	0%	-75%	0%	0 cm
4	0%	+75%	0%	0 cm
5	0%	0%	-10%	0 cm
6	0%	0%	+10%	0 cm
7	0%	0%	0%	-25 cm
8	0%	0%	0%	+25 cm

Table 4.1: Input parameters for sensitivity cases.

Varying mud density

To assess the effect of a different density, the reference case was run after implementing a lower and a higher density (see Case 5 and 6 in table 4.1). The difference in density, ρ_m, does not invoke large differences in damping (figure 4.7). Only for very thin mud layers a considerable difference can be seen in the amount of damping that will occur for a either a lower or a higher density. This is the case when the input parameters are assumed to be uncorrelated. It is highly unlikely, however, that this assumption is valid. The most obvious correlation can be found between the mud density, ρ_m, and the viscosity, ν_m. Generally, when a lower density is observed, a lower viscosity is expected as well (Kranenburg, 1994), and thus a lower amount of damping is expected.

Varying water level

To test the influence of a different water level on the damping, the reference case has been run for a lowered and heightened water level surface (see Case 7 and 8 in table 4.1). For a fixed mud layer thickness, h_m, the change in damping due to a varying water level resembles the change in damping due to a change in mud layer thickness in case of a fixed water level (figure 4.8). The change in water depth implemented in these cases amounts to $\pm$25% at SW and $\pm$40% at LW. The effect of a change in water depth is much larger for a larger water depth over mud layer thickness ratio h_w/h_m; up to about 15% for the viscosity in the reference case.

4.2.4. Step 4: Frequency Dependency

In previous steps, a simple sinusoidal wave was used. This is, however, an oversimplification of reality. As shown by Kranenburg et al. (2011), the wave damping is spectrally distributed and dependent on frequency. For the same mud characteristics and significant wave height as the reference case, the damping is calculated for a range of monochromatic waves with an increasing mean wave period T_{m01} (figure 4.9). The most effective damping is found around a frequency of 0.45 Hz. Different combinations of mud layer thickness, h_m, and viscosity, ν_m, that yield the same damping at $T_{m01} = 2.3$ s do not yield the same damping for other frequencies (figure 4.9). For higher frequencies, a smaller mud layer thickness in combination with a lower viscosity yields a higher damping rate than a thick mud layer with a high viscosity. For frequencies larger than about 0.8 Hz, the effect of shoaling becomes larger than the damping by the viscous mud layer ($k_i < 0$ rad/m). When looking at spectral distributions of wave energy, it means that certain combinations of mud parameters affect the spectrum more effectively at different frequencies than others. Hence, the outcomes of the sensitivity analysis in section 4.2.3 are expected to differ as well for spectral wave input compared to a monochromatic forcing.

Therefore, part of the sensitivity analysis from section 4.2.3 was carried out again using the variance density spectrum measured at SW at 2018-12-07 23:19:28 as wave input (figure 4.2). The damping is less in case of this spectral input in comparison with the simple sinusoidal wave (figure 4.10). The frequency of this monochromatic wave is close to the frequency associated with optimum damping (for the range of mud characteristics that are being considered here; figure 4.9). In the spectrum, however, the

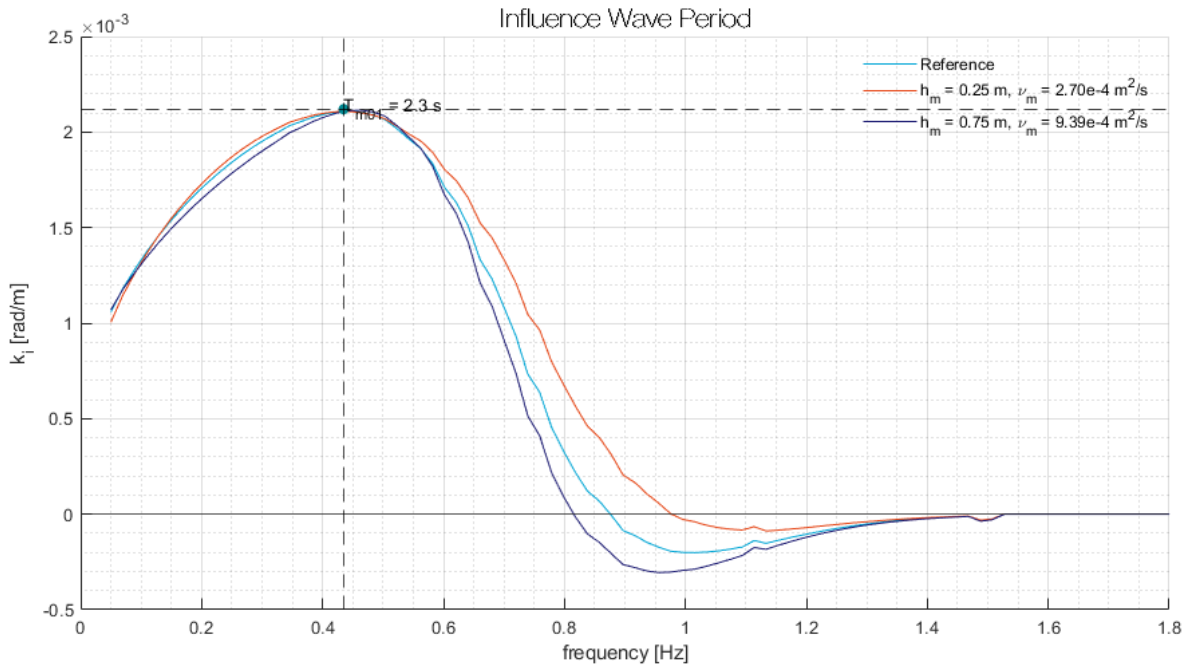

Figure 4.9: Influence of frequency on the relative amount of damping k_i.

frequencies for which significant energy is present range from 0 to about 1 Hz, with the peak located at about the optimum damping frequency. Therefore, although the peak is damped in the same manner as the monochromatic wave, a large part of the spectrum is damped to a lesser rate, hence the energy loss in the spectrum is less. This results in a larger H_{m0} at LW and thus a smaller damping over the transect.

To assess the response of the system to an actual sea state in more detail, a comparison was made between the calculated spectrum at LW based on the calibration parameters and the measured spectrum at LW. Whereas the measured spectrum at LW (figure 4.11) has a significant wave height of $H_{m0} = 0.161$ m, the calculated spectrum has a significant wave height of $H_{m0} = 0.168$ m. This indicates that the total variance density in the calculated spectrum is too large in comparison with the measured spectrum; the damping is underestimated. Looking at the spectral shape, the variance density around the peak is overestimated, while the energy in the tail is underestimated. Furthermore, the smaller peak in the measured spectrum around $f = 0.45$ Hz is not accurately reproduced. As the variance density in the tail of the spectrum at SW is lower than at LW, clearly an input of energy is required or a transfer of energy from lower to higher frequencies. As an underestimation of the damping of the spectrum at LW was already expected based on the sensitivity analysis, the calibration has been improved to predict H_{m0} and thus the total variance density in the wave spectrum more accurately. This calibration will in the following be referred to as the *spectral calibration*, whereas the original calibration will be referred to as the *monochromatic calibration*. As the same damping as for the monochromatic case, can only be achieved whilst using a spectral wave input by implementing an increased viscosity, the viscosity determined from the samples by Deltares proved to better fitting for the spectral case. The mud layer thickness that matches the measured damping in combination with this viscosity is $h_m = 0.72$ m. This is more within the range of expectation than $h_m = 0.93$ m as determined in the monochromatic wave case for this viscosity. For these improved calibration parameters, the peak of the spectrum is reproduced better than in case of the monochromatic calibration, although there is still an overestimation at the right side of the peak (figure 4.11). From section 4.2.1 follows that the prediction of the damping could also be achieved without the use of a fluid mud module, using a heightened bottom friction factor instead. Although this friction factor is too high to be a physically sound representation of reality, it is included in this analysis to assess whether using a fluid mud module is a significant improvement over just using bottom friction. As the calibration of this friction factor was based on monochromatic wave input, the total energy in the spectrum is overestimated in this case as well (figure 4.11). The results show resemblance to the monochromatic calibration. Using the default friction factor underestimates

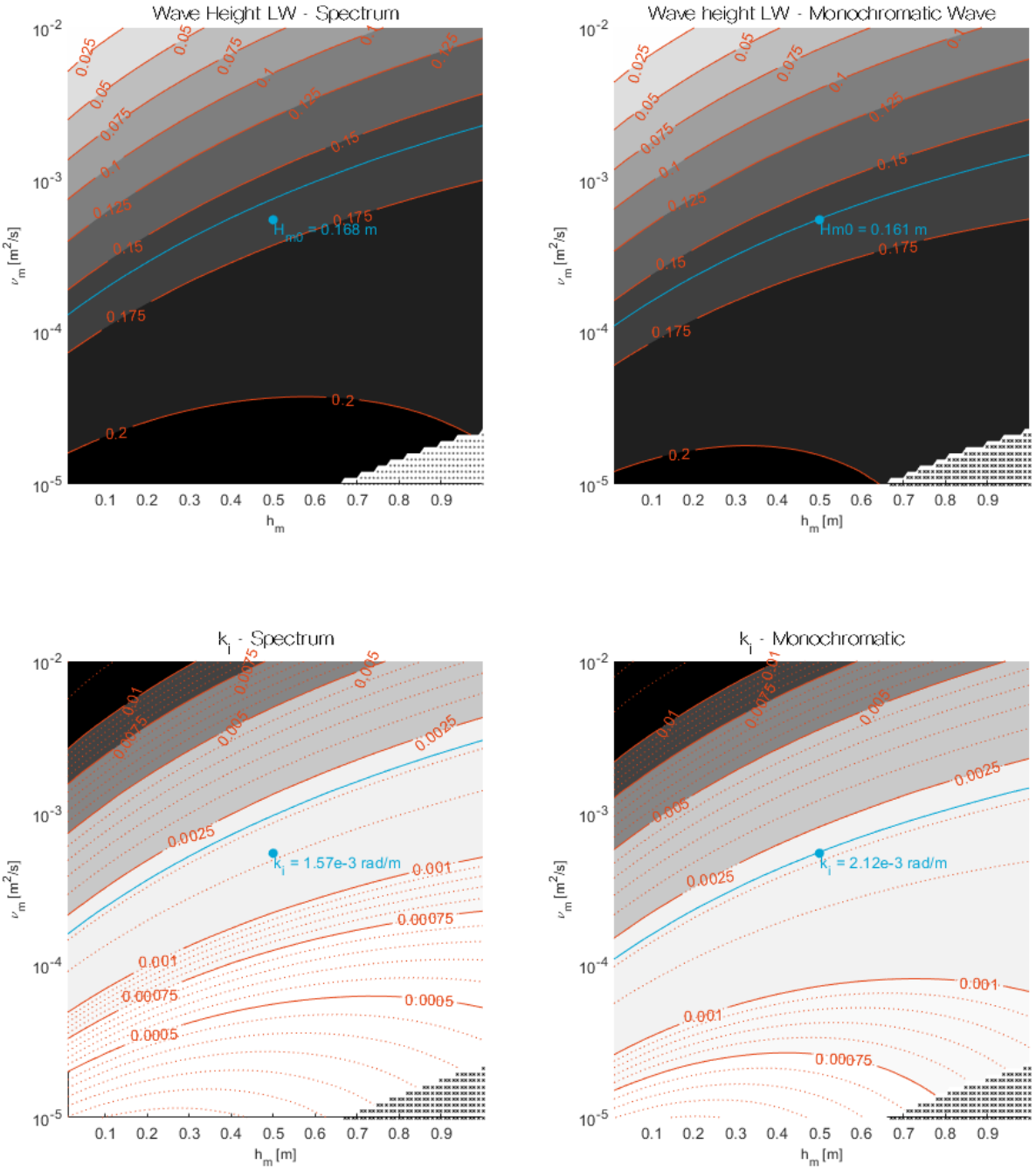

Figure 4.10: Result of the sensitivity runs of the SWAN-Mud model for a spectral wave input and and a monochromatic wave input, for ρ_m =1200 kg/m^3. The upper panels show the wave height at LW, the lower panels show the imaginary part of the wave number k_i. The left panels show the results for the spectral forcing and the right panels for the monochromatic. In all plots the cyan line denotes all possible combinations of h_m and ν_m that give H_{m0} = 0.161 m and k_i = 2.12×10^{-3} respectively. The dot indicates the reference case (h_m = 0.5 m and ν_m = 5.47×10^{-4} m^2/s). Crosses denote combinations where SWAN-Mud would not give a physically sound outcome.

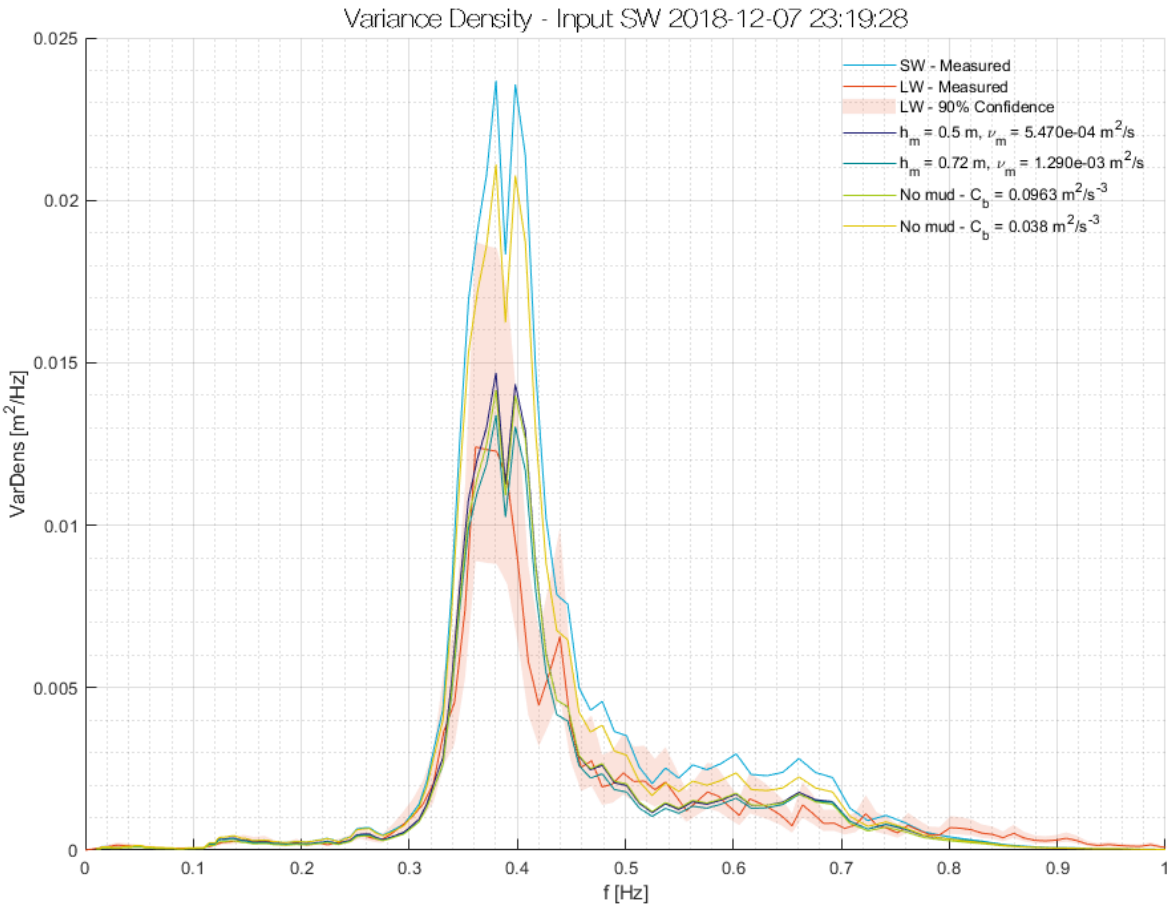

Figure 4.11: Variance density spectra obtained from SWAN-Mud using spectral wave input. The upper panel shows these spectra, the lower panel shows the damping per frequency with respect to the input spectra for each model run. The shaded red area in the upper panel is the 90% confidence interval with which the measured wave spectrum is determined.

the damping significantly (figure 4.11).

To quantify the quality of the reproduction of the spectrum for the different calibration settings, two parameters are introduced; the **R**oot **M**ean **S**quared **E**rror (4.1) and the **S**kill **S**core (4.2). Both these parameters are based on the dissipation of variance density per frequency bin of the considered spectra. The skill score is relative to the calibrated model without mud, where a skill of 0 indicates equal performance, a skill <0 worse performance and a skill of 1 perfect performance (no difference with measurements). The performance of the monochromatic calibration and the model using only bottom stress is nearly equal (table 4.2). The model calibrated for spectral dissipation performs better than both other methods (indicated by a correctly predicted H_{m0}, a smaller RMSE and a larger SS with respect to the case without mud).

$$\text{RMSE} = \sqrt{\frac{1}{N}\sum_{i=1}^{N}[D_{\text{model}}(f_i) - D_{\text{obs}}(f_i)]^2} \tag{4.1}$$

$$\text{SS} = 1 - \frac{\sqrt{\frac{1}{N}\sum_{i=1}^{N}[D_{\text{model}}(f_i) - D_{\text{obs}(f_i)}]^2}}{\sqrt{\frac{1}{N}\sum_{i=1}^{N}[D_{\text{obs}}(f_i) - D_{\text{obs}}(f_i)]^2}} \tag{4.2}$$

with:

$$D_{\text{model}}(f) = E_{\text{SW}}(f) - E_{\text{model}}(f)$$
$$D_{\text{obs}}(f) = E_{\text{SW}}(f) - E_{\text{obs}}(f)$$

	h_m [m]	ν_m [m^2/s]	C_b [m^2/s^{-3}]	$H_{s,\text{LW}}$ [m]	RMSE [10^{-3} m^2/Hz]	SS [-]
monochromatic calibration	0.50	5.47×10^{-4}	-	0.1677	0.6420	0.09
spectral calibration	0.72	1.29×10^{-3}	-	0.1610	0.5190	0.26
no mud	-	-	0.0963	0.1697	0.7024	0.00

Table 4.2: Quality of the model predictions.

To assess whether the dependency of damping on frequency (figure 4.9) is visible in the attenuation of the spectrum as well, k_i was calculated as a measure for the relative damping per frequency bin. To minimise the influence of abnormalities in the individual spectra on the outcome of this analysis, SWAN-Mud has been run for the spectra between 2018-12-07 15:30:00 and 2018-12-08 00:00:00. These variance density spectra represent the same sea state as the reference case and were averaged before calculating the relative damping. The measured k_i resembles the dependency on the frequency (as calculated earlier based on a series of monochromatic waves; figure 4.9) well. The monochromatic calibration and the spectral calibration follow this trend in the measured damping (figure 4.12), with the spectral calibration representing the actual measurements more closely. In both cases, the damping in the tail, f >0.75 Hz, is overestimated. The dependency on frequency is less well modelled when the mud module is switched off. The lower frequencies, f <0.3 Hz, show discrepancies between the measured and modelled damping. As some of the observed mean frequencies are lower than this threshold (figure 3.7), this could have a serious effect on the modelled attenuation of these sea states.

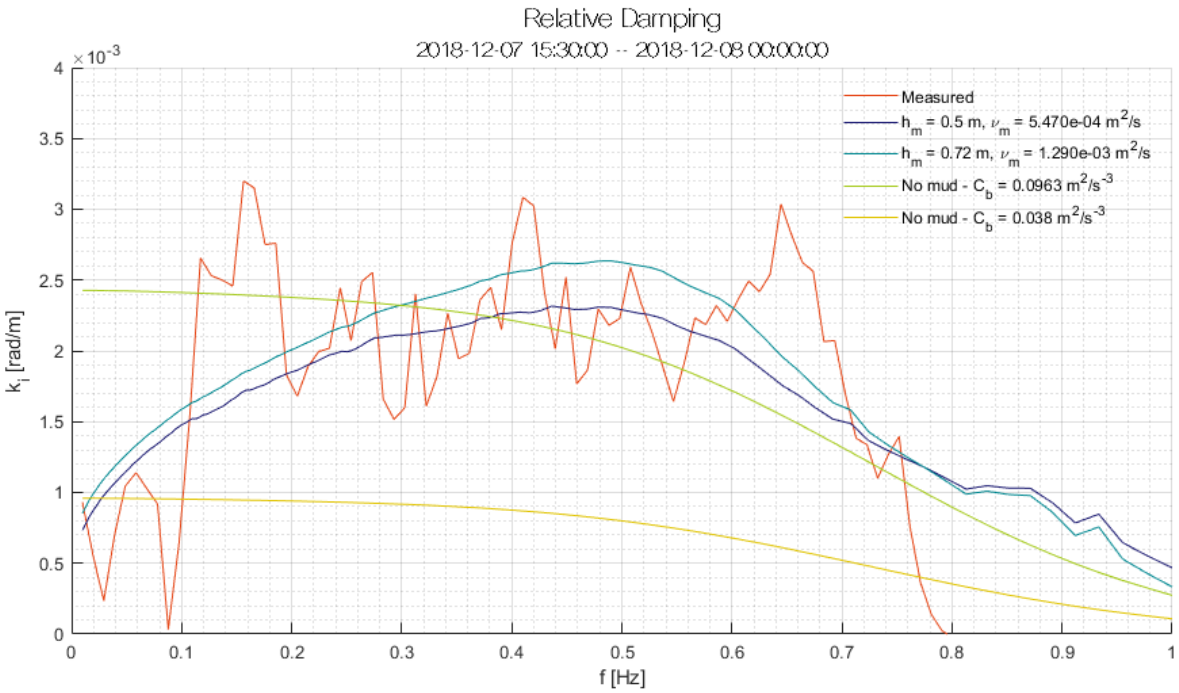

Figure 4.12: Relative damping per frequency bin in the variance density spectra in terms of k_i. These curves represent the average relative damping over the period between 2018-12-07 15:30:00 to 2018-12-08 00:00:00.

4.2.5. Step 5: Validation

In the current configuration, the model schematisation was only applied to the reference case (section 4.2). To test the validity of the model, the measurements of the field campaign at Surodadi from 2018-12-05 18:46:24 until 2018-12-08 03:58:56 was used (figure 4.13). A sequence of stationary runs has been done for this particular time series for the monochromatic calibration (h_m = 0.5 m and ν_m = 5.47×10^{-4} m^2/s), the spectral calibration (h_m = 0.72 m and ν_m = 1.29×10^{-3} m^2/s) and in case no mud is present (C_b =0.0963 m^2/s^{-3}). For these simulations, a monochromatic wave is used as input at SW.

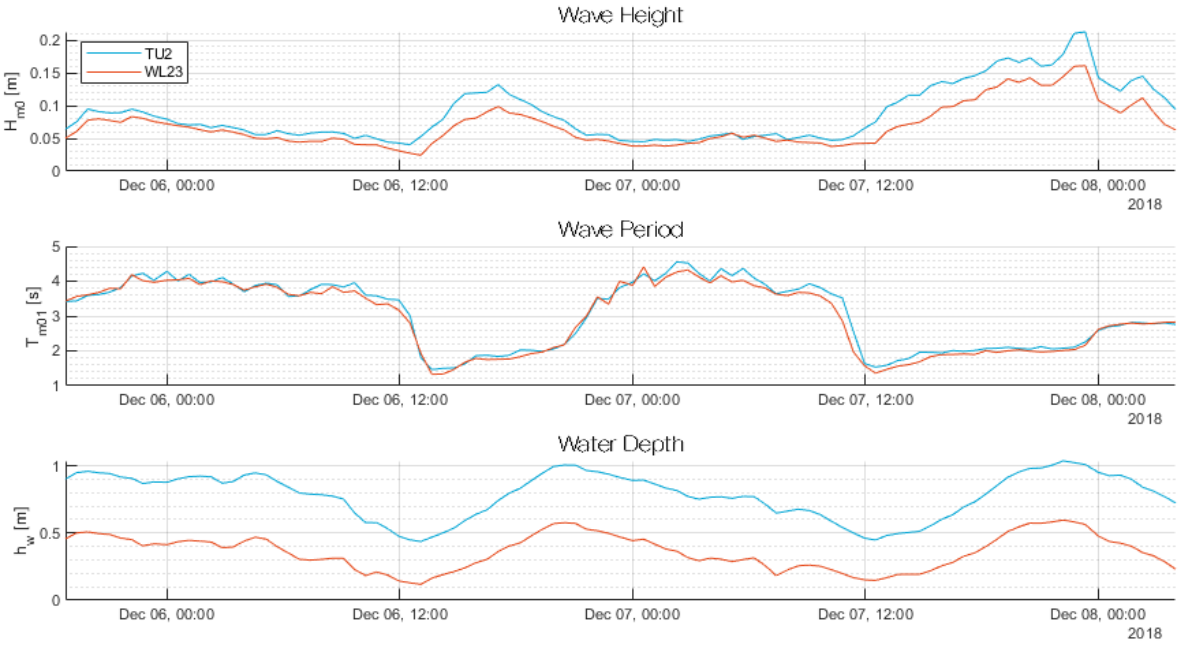

Figure 4.13: Data from Surodadi, 2018-12-05 18:46:24 to 2018-12-08 03:58:56, used as input for the validation of the model schematisation.

The performance was assessed based on the **R**oot **M**ean **S**quared **E**rror (4.3), the **bias** (4.4), the correlation coefficient (**R**) (4.5), the **S**catter **I**ndex (4.6) and the **S**kill **S**core (4.7). A smaller RMSE indicates a better performance; the total error made with regard to the measurements is smaller. The bias indicates the tendency to over- (positive bias) or under-prediction (negative bias). The correlation coefficient R establishes how well the trend in the relationship between the observed and modelled quantities is being reproduced. Ideally, this relationship should be linear. A value of 1 for R means that, although there might be a difference between the measured and modelled data, this difference is merely an offset. A value close to 0 would indicate that the relationship between the modelled and the observed data is highly none linear and the processes on which the model is based are not able to capture the behaviour of the system well. The Scatter Index is the RMSE normalised with the mean error. A lower SI therefore indicates a better performance. The Skill Score indicates the performance of the model in reference to a baseline prediction, which in this case is the model without mud. An SS of 0 indicates that the performance is the same as the baseline, SS>0 that the performance is better and SS<0 that the performance is worse. SS=1 indicates perfect performance, in other words the prediction is equal to the measurements. These assessment parameters will be determined based on the absolute dissipation (of wave height, $X = D = H_{SW} - H_{LW}$) and on the imaginary part of the wave number, which is taken here as a measure for the relative wave damping ($X = k_i$). X_{model} is the model prediction by SWAN-Mud, X_{obs} is the observation and X_{ref} is the reference prediction, for which the non-mud simulation with C_b =0.0968 m^2/s^{-3} is taken.

$$\text{RMSE} = \sqrt{\frac{1}{N}\sum_{i=1}^{N}[X_{\text{model}}(t_i) - X_{\text{obs}}(t_i)]^2} \tag{4.3}$$

$$\text{bias} = \frac{1}{N}\sum_{i=1}^{N} X_{\text{model}}(t_i) - X_{\text{obs}}(t_i) \tag{4.4}$$

$$\text{R} = \frac{\sum_{i=1}^{N}[X_{\text{model}}(t_i) - \overline{X_{\text{model}}}][X_{\text{obs}}(t_i) - \overline{X_{\text{obs}}}]}{[X_{\text{model}}(t_i) - \overline{X_{\text{model}}}]^2[X_{\text{obs}}(t_i) - \overline{X_{\text{obs}}}]^2} \tag{4.5}$$

$$\text{SI} = \frac{\sqrt{\frac{1}{N}\sum_{i=1}^{N}[X_{\text{model}}(t_i) - X_{\text{obs}}(t_i)]^2}}{\frac{1}{N}\sum_{i=1}^{N} X_{\text{obs}}(t_i)} \tag{4.6}$$

$$\text{SS} = 1 - \frac{\sqrt{\frac{1}{N}\sum_{i=1}^{N}[X_{\text{model}}(t_i) - X_{\text{obs}}(t_i)]^2}}{\sqrt{\frac{1}{N}\sum_{i=1}^{N}[X_{\text{ref}}(t_i) - X_{\text{obs}}(t_i)]^2}} \tag{4.7}$$

The performance of both mud simulations is similar, with the spectral calibration overestimating the damping slightly more than the monochromatic calibration (figure 4.15). This is indicated by a higher value for the bias (table 4.3) for both the absolute and the relative wave damping (figure 4.14). As these values are positive, the models generally overestimate the damping. Both the Scatter Index and the Skill Score indicate the monochromatic calibration better predicts the wave damping, absolute and relative. The non-mud model is clearly not able to reproduce the behaviour of the mud system as well as the models using a fluid mud module. The large difference between measured and predicted values (which occur despite the fact that the modelled damping at the calibration point matches the observed damping) again indicates that bottom friction is unlikely to be the mechanism responsible for the dissipation of wave energy at muddy coasts.

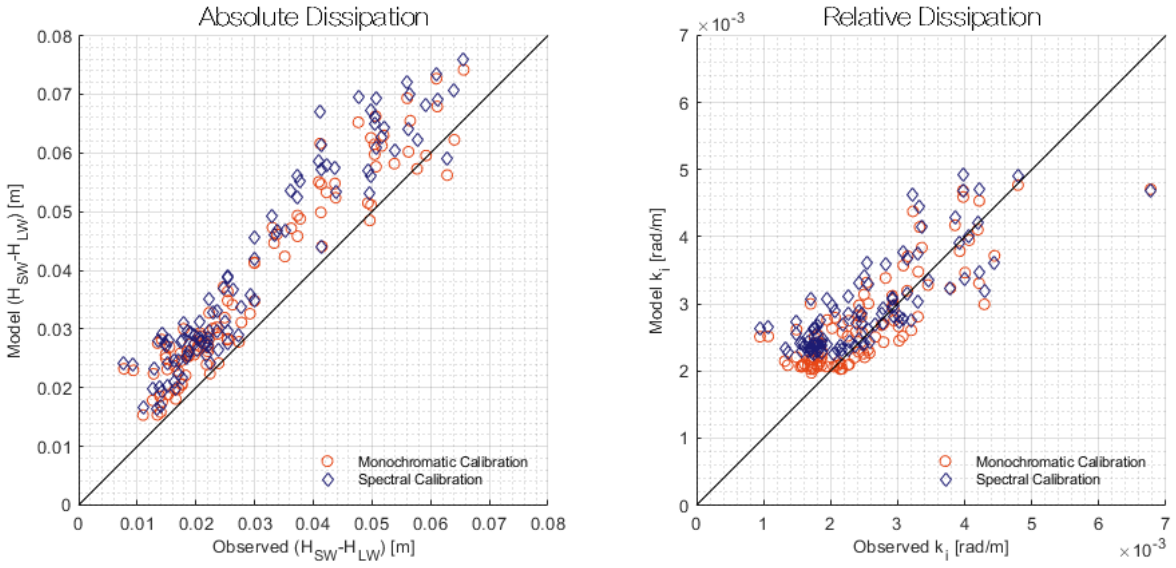

Figure 4.14: Comparison of the modelled dissipation with the observed observation for the monochromatic validation. The solid line shows perfect agreement with the measurements (SI = 0).

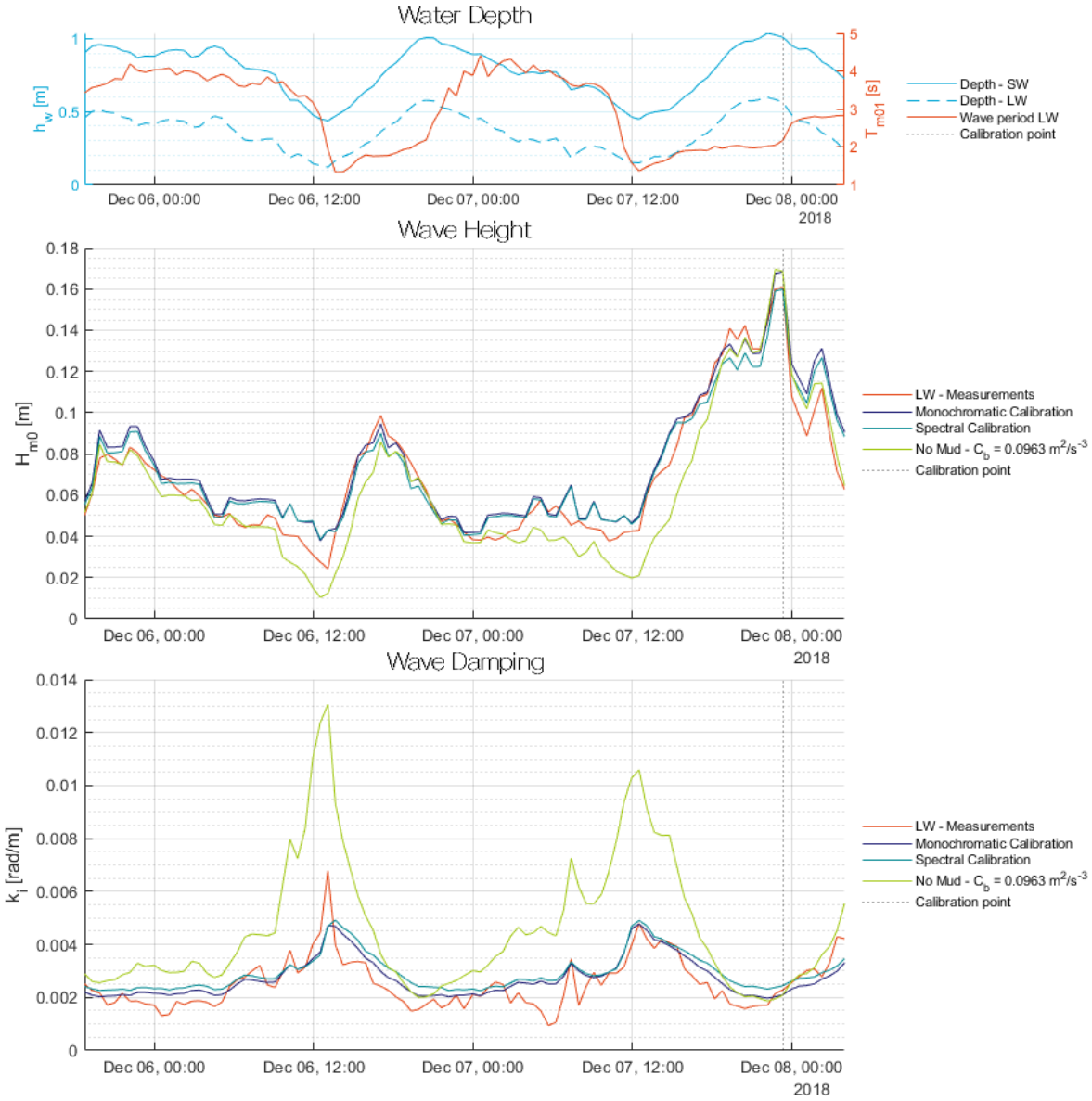

Figure 4.15: Results of the validation runs using a monochromatic waves. The top panel shows the water depth at the left axis and the wave period at LW at the right axis. The middle and lower panel show the time series for the wave height and k_i respectively.

	h_m	ν_m	C_b	RMSE D $\times 10^{-2}$	RMSE k_i $\times 10^{-3}$	bias D $\times 10^{-2}$	bias k_i $\times 10^{-3}$	R D	R k_i	SI D	SI k_i	SS D	SS k_i
monochromatic calibration	0.50	5.47×10^{-4}	-	0.87	0.57	0.73	0.21	0.96	0.83	0.29	0.23	0.64	0.79
spectral calibration	0.72	1.29×10^{-3}	-	1.11	0.70	0.97	0.40	0.96	0.80	0.36	0.27	0.54	0.74
no mud	-	-	0.0963	2.37	2.72	2.05	2.04	0.85	0.81	0.78	1.08	0	0

Table 4.3: Quality of model predictions for a monochromatic time series of waves.

For the same time frame, measured variance density spectra are available for both SW and LW. The data from SW has been used as the wave input for a series of stationary runs, after which the results are compared to the spectra measured at LW (figure 4.17 and 4.18). The models that are using the fluid mud module show more resemblance with the measurements than the model without mud. Some noticeable differences with the measurements occur within the 0.6-0.8 Hz frequency band (right panels figure 4.19). The models generally overestimate the damping for these frequencies. If peaks occur around 2 Hz, the damping of these peaks is generally overestimated as well (left panels figure 4.19). These observations have also been made in section 4.2.4. The performance of the model is assessed according to the same parameters ((4.3) to (4.7)) as the monochromatic wave simulation (table 4.4). Both models using the mud module perform considerably better compared to the case without a mud layer. The SI-values suggest that the monochromatic calibration outperforms the spectral calibration. The monochromatic calibration shows a tendency to underestimate of the damping (bias<0), while the spectral calibration shows a tendency toward overestimation (bias>0).

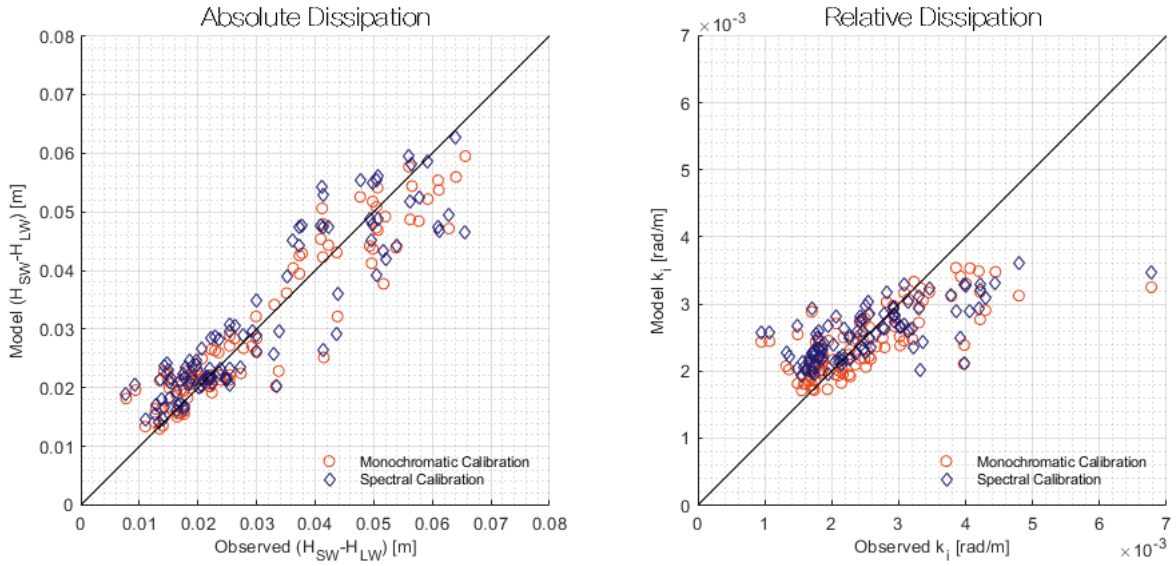

Figure 4.16: Comparison of the modelled dissipation with the observed observation for the time series of wave spectra. The solid line shows perfect agreement with the measurements (SI = 0).

	h_m	ν_m	C_b	RMSE D $\times 10^{-2}$	RMSE k_i $\times 10^{-3}$	bias D $\times 10^{-2}$	bias k_i $\times 10^{-3}$	R D	R k_i	SI D	SI k_i	SS D	SS k_i
monochromatic calibration	0.50	5.47×10^{-4}	-	0.54	0.67	-0.04	-0.09	0.94	0.75	0.18	0.26	0.65	0.74
spectral calibration	0.72	1.29×10^{-3}	-	0.65	0.72	0.09	0.02	0.91	0.71	0.21	0.28	0.57	0.72
no mud	-	-	0.0963	1.53	2.56	1.28	1.92	0.90	0.80	0.50	1.01	0	0

Table 4.4: Quality of model predictions of a time series of energy density spectra.

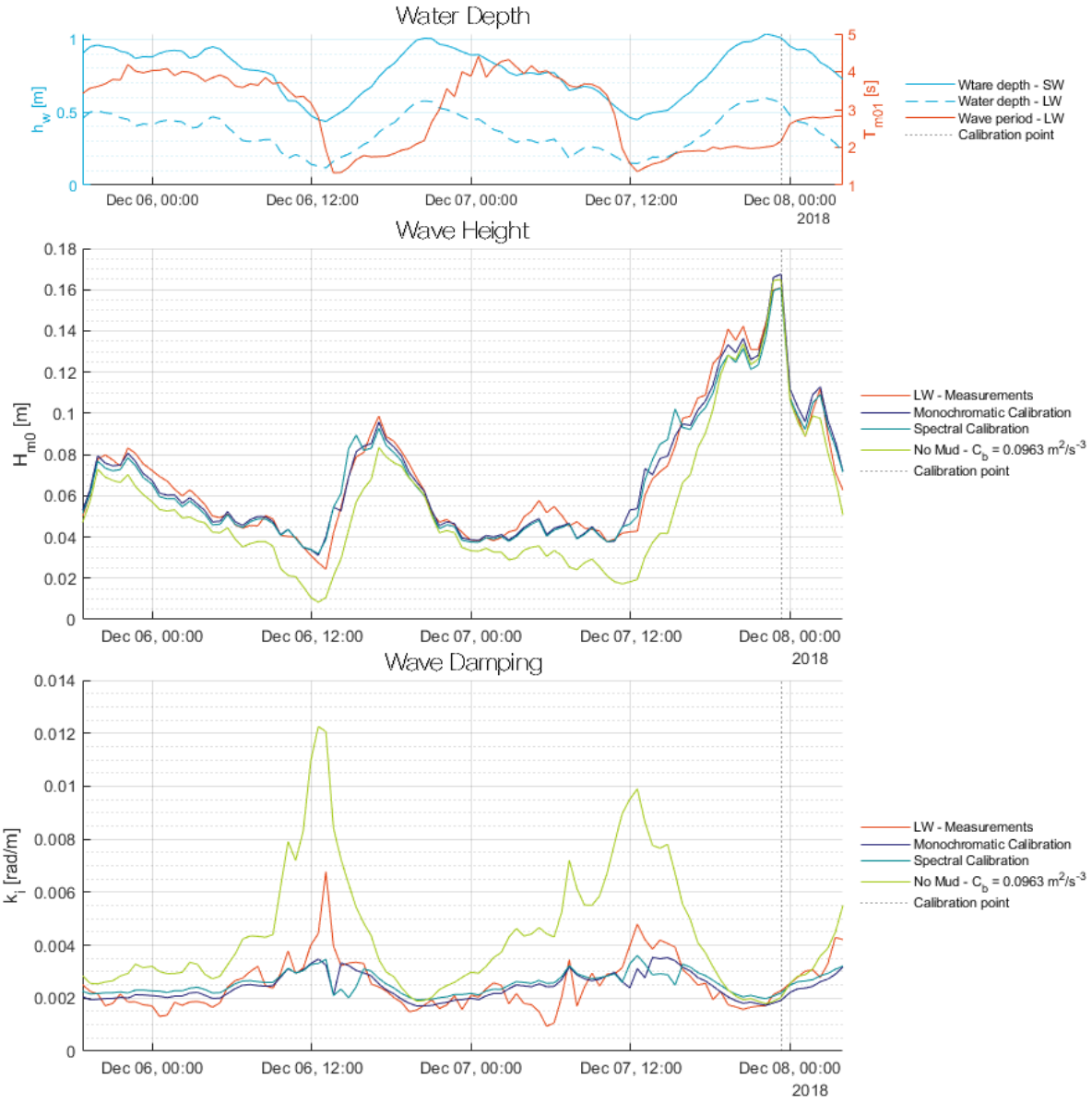

Figure 4.17: Results of the validation runs using a series wave spectra. The top panel shows the water depth at the left axis and the wave period at LW at the right axis. The middle and lower panel show the time series for the wave height and k_i respectively.

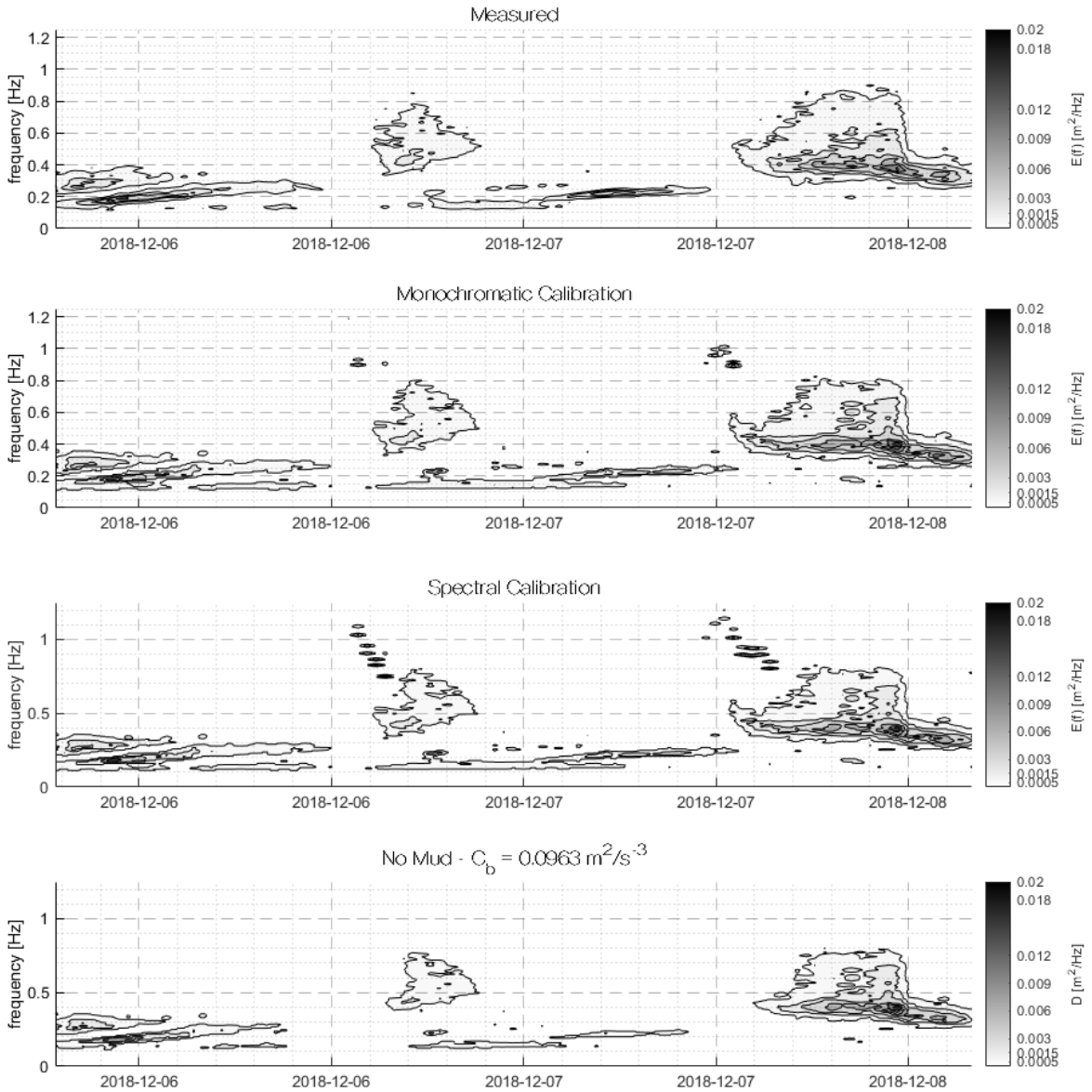

Figure 4.18: Evolution per frequency of the variance density spectra for the validation runs using a series wave spectra. The top panel shows the measurements at LW. The two middle panels show the model results for the simulations that use a fluid mud module. The lower panel shows the spectral evolution without mud, but with an implemented bottom friction.

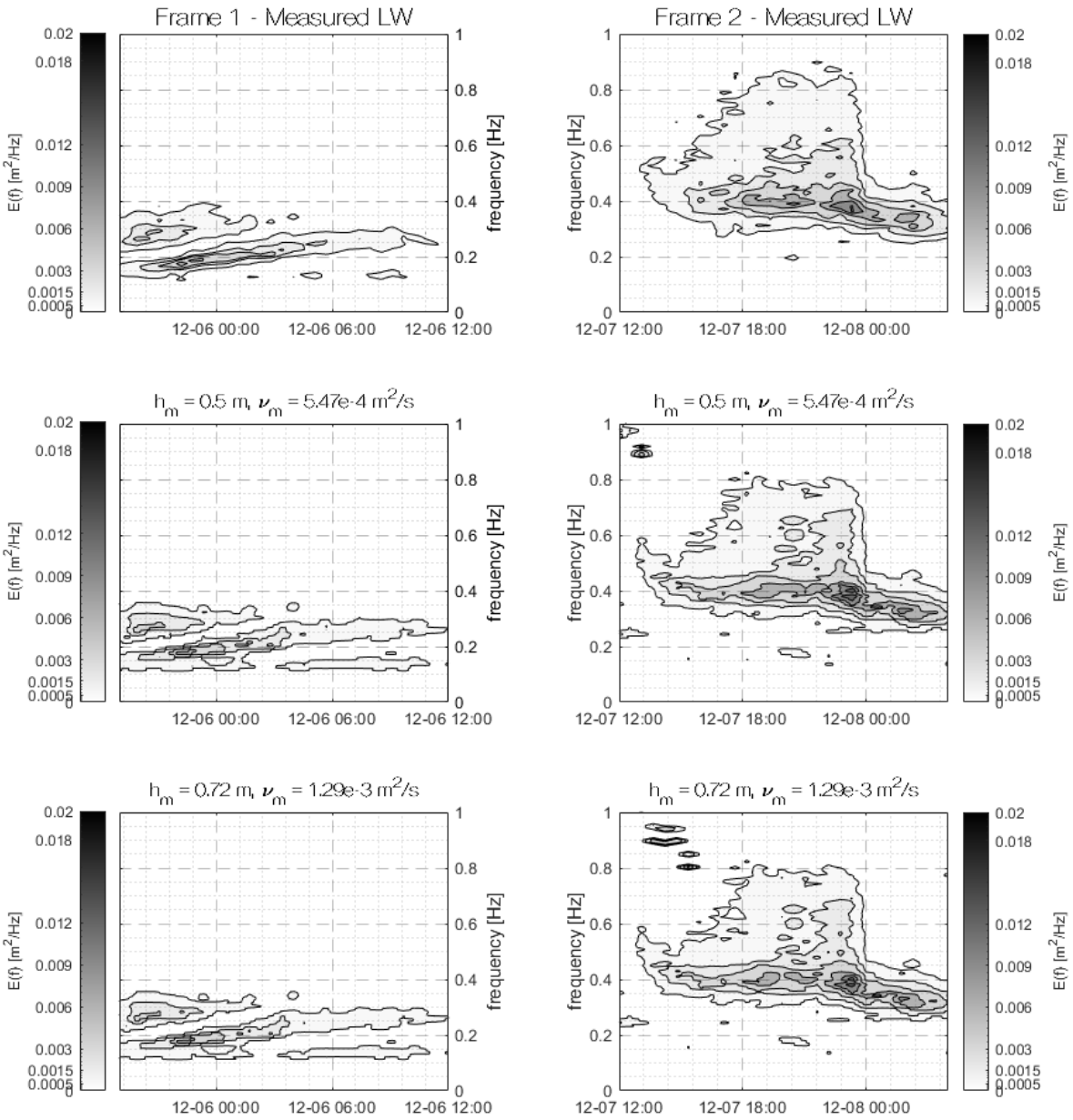

Figure 4.19: Evolution per frequency of the variance density spectra for the validation runs, zoomed in on the same frames as in section 3.3.3. The top panel shows the measurements at LW. The two lower panels show the model results for the simulations that use a fluid mud module.

4.2.6. Conclusion

As already shown by Kranenburg et al. (2011), the performance of the models is largely influenced by the implemented viscosity and mud layer thickness. As different parameter combinations that yield the same overall damping can effect different parts of a spectrum to a larger or lesser extent, it is important to get a good estimation for these mud characteristics from field measurements. The wave period seems to be an important influence on the amount of damping that occurs and so does the water depth.

With respect to the validation, it can clearly be concluded that it is preferable to use a fluid mud module instead of an adapted value for the bottom friction. The larger the difference in wave height for which the bottom friction was calibrated, the larger the error gets. Between the models that do use a fluid mud module, the monochromatic calibration performs best for both the monochromatic wave input and wave input by variance density spectra. Although the spectral calibration predicts the shape of the individual spectrum better at the calibration point, due to the large influence of frequency and water depth on the damping of the spectrum, the performance is different for other points in the time series. The monochromatic calibration provides a more consistent performance. Between using spectral wave input and monochromatic wave input, the models using spectral wave input perform slightly better. The monochromatic input, however, is easier to implement and results in faster calculations. Therefore, this is used in combination with the monochromatic calibration in the following parts of this thesis.

4.3. Response Fluid Mud layer to Wave Forcing

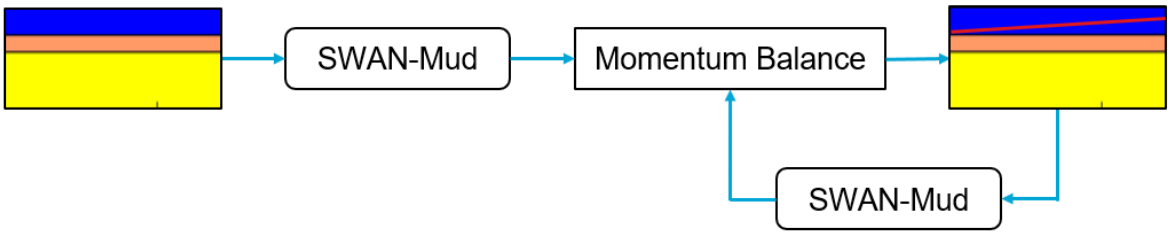

Figure 4.20: Iteration algorithm to calculate the slope of the interface of the fluid mud layer, combining SWAN-Mud with either the Simple Balance Model (section 4.3.1) or the Two-Layer Model (section 4.3.2).

The momentum balances (2.44) and (2.45) have been combined with SWAN-Mud and the previously validated schematisation to assess the conditions under which a gradient in the interface level could exist and to compare the slopes found during the field campaign with the expected slopes based on the measured wave characteristics. The flowchart in figure 4.20 illustrates this simple model. During the first iteration, SWAN-Mud is forced with a monochromatic wave in stationary mode, using the same assumptions as described in section 4.1. It is worthwhile to note that all breaking processes have been turned off. Deviating from section 4.1, the bottom is assumed to be flat and the thickness of the mud layer on top of this bottom constant. The mud characteristics are equal to the monochromatic calibration in sections 4.2.4 and 4.2.5. The results of this simulation give the change in radiation stress over the domain. Instead of using the expressions in section 2.3.3, the gradient in radiation stress can be extracted from SWAN-Mud directly. This, however, is the wave force in the water layer, $-\frac{\partial S_{xx,w}}{\partial x}$, based on the energy of to the surface wave. To be able to implement this wave force in the momentum balances (2.44) and (2.45), the wave force in the mud layer $-\frac{\partial S_{xx,m}}{\partial x}$ needs to be calculated as well. This can be done using the ratio between the surface wave amplitude, a, and internal wave amplitude, b, (equation (4.8)), which is a measure for the ration between the wave energy of the surface waves, E, and the wave energy in the mud layer, E_m.

$$\frac{\partial S_{xx,m}}{\partial x} = \frac{\rho_m b^2}{\rho_w a^2} \frac{\partial S_{xx,w}}{\partial x} \tag{4.8}$$

with $\frac{b}{a}$ defined according to Kranenburg (2008) as:

$$\xi = \xi_0 e^{i(ki-\omega t)} = be^{\phi} e^{i(ki-\omega t)}$$
$$\frac{b}{a} = \text{mod}\left[\frac{\xi_0}{a}\right] = \text{mod}\left[\cosh(kh_{w0}) - \frac{\sinh(kh_{w0})gk}{\omega^2}\right] \tag{4.9}$$

Two approaches are taken to determine the slope of the fluid mud interface. For the first approach (section 4.3.1), it is assumed that the slope of the water surface is negligibly small in comparison with the slope of the fluid mud interface (Rodriguez, 1997; Rodriguez and Mehta, 1998). The momentum balances (2.44) and (2.45) then reduce to (4.10), which is a direct balance between the gradient in radiation stress in the mud layer and the pressure gradient due to the slope of the interface.

$$\frac{g\Delta\rho}{\rho_m}\frac{\partial\overline{\xi}}{\partial x} + \frac{1}{\rho_m h_m}\frac{\partial S_{xx,m}}{\partial x} = 0 \tag{4.10}$$

In the second approach (section 4.3.2), the slope of the free surface is not neglected and the momentum balances (2.44) and (2.45) have been used without further simplifications. The calculated slope is implemented in the input files of SWAN-Mud. The mud thickness and thus interface level at $x = 0$ m is taken from the previous run (and thus constant over all runs) and the slope is implemented starting from this point in positive x-direction. This updated bottom forms the input for a new SWAN-Mud simulation. The slope of the free surface (in case of the second approach) is included in SWAN-Mud in the same manner. This process is repeated until the solution has converged, thus giving the slope under which the system would be in equilibrium.

4.3.1. Including Fluid Mud: Simple Balance Model

The slope resulting from the SWAN-Mud calculations is dependent on the wave characteristics (significant wave height and mean wave period), the ratio between water depth and mud layer thickness and the characteristics of the mud (viscosity and density). These parameters determine the ratio between the surface wave amplitude and the internal wave amplitude, $\frac{b}{a}$, and the gradient in the radiation stress of the system, $\frac{\partial S_{xx}}{\partial x}$, and thus determine the final equilibrium slope (momentum balance (4.8)). The response of the model was tested for different combinations of these parameters. The reference case is a system with a water depth of 1.0 m and a mud layer with a thickness of 0.5 m, forced by a wave with $H_{m0} = 0.5$ m and a wave period $T_{m01} = 5$ s. The viscosity of the mud layer in the reference case is $\nu_m = 5.47\times10^{-4}$ m^2/s and the density 1200 kg/m^3. The decrease in radiation stress over the transect is not linear and therefore the horizontal gradient will not be constant over the transect. Following balance (4.8), the forced equilibrium slope will not be constant over the transect. To be able to effectively compare the results of different simulations, a indicative slope is adopted, $(\overline{\xi}_{\text{SW}} - \overline{\xi}_{\text{LW}})/L$.

In general, forcing by larger waves (larger H_{m0}) results in a larger slope of the fluid mud interface (figure 4.21). For a fixed wave height, however, there is an optimum wave period T_{m0} that results in the largest slope. For the system as assessed here, this means that the largest slopes will occur for waves with a period of 2.5-4 s. When applying a constant wave forcing, but changing the schematisation of the system (changing h_w and h_m, to simulate for example the effect of tide and the difference in mud thickness over the seasons), a combination of a thin mud layer with a small water depth gives the largest slope (figure 4.22). This is according to expectation, because a thinner mud layer leads to a stronger damping of waves (section 4.2.3) and because a smaller water depths leads to a more efficient transfer of energy to the fluid mud layer; the orbital velocities near the interface will be larger than in case of a larger water depth. For a fixed water depth, there is an optimum mud thickness that results in the largest slope, hence the ratio h_m/h_w is an important parameter. The importance of the parameter h_m again becomes apparent when the mud characteristics are changed (figure 4.23). For a fixed viscosity, there is an optimum mud layer thickness for which the largest set-up occurs and for this schematisation and wave forcing the optimum lies around 0.4-0.5 m. The wave height over the water depth is an important indicator for the magnitude of the orbital motion at the interface and thus for the effectiveness of the energy transfer to the fluid mud layer. As expected, a large ratio leads to the largest slope of the interface (figure 4.24). It should, however, be noted that there is an upper limit to

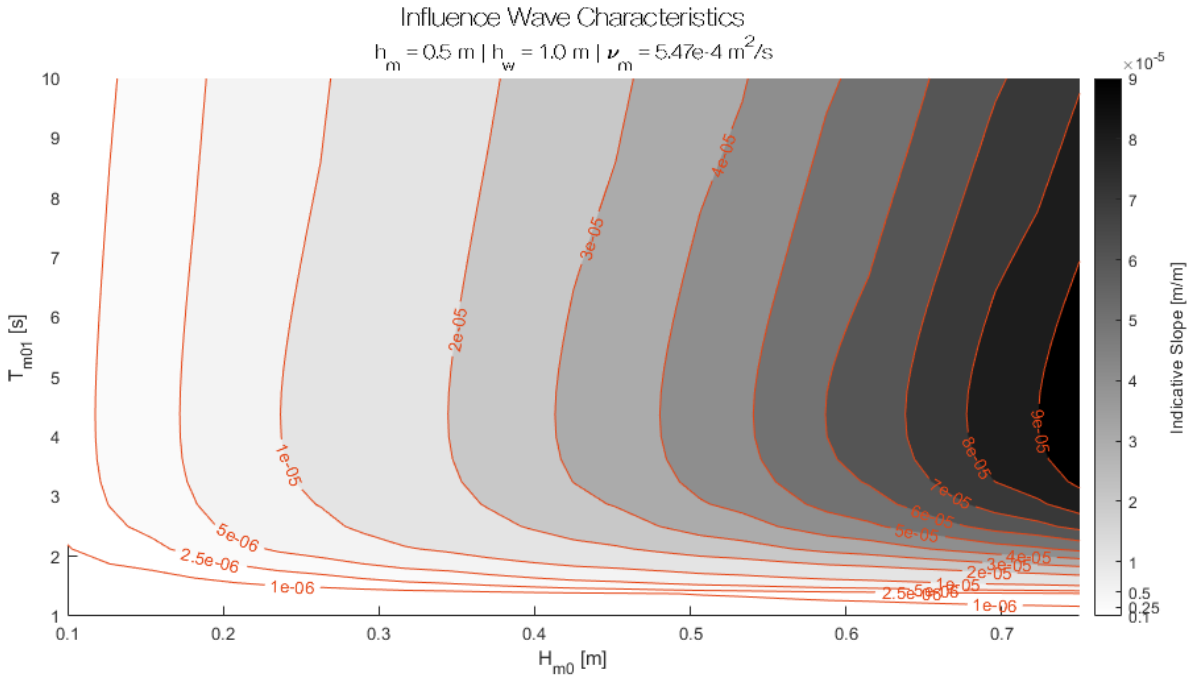

Figure 4.21: Indicative slope as calculated by the Simple Balance Model as a function of the wave parameters H_{m0} and T_m01. Other parameters have been kept constant as displayed at the top of the figure. The ticks of the colorbar are equal to the values of the isolines in the graph.

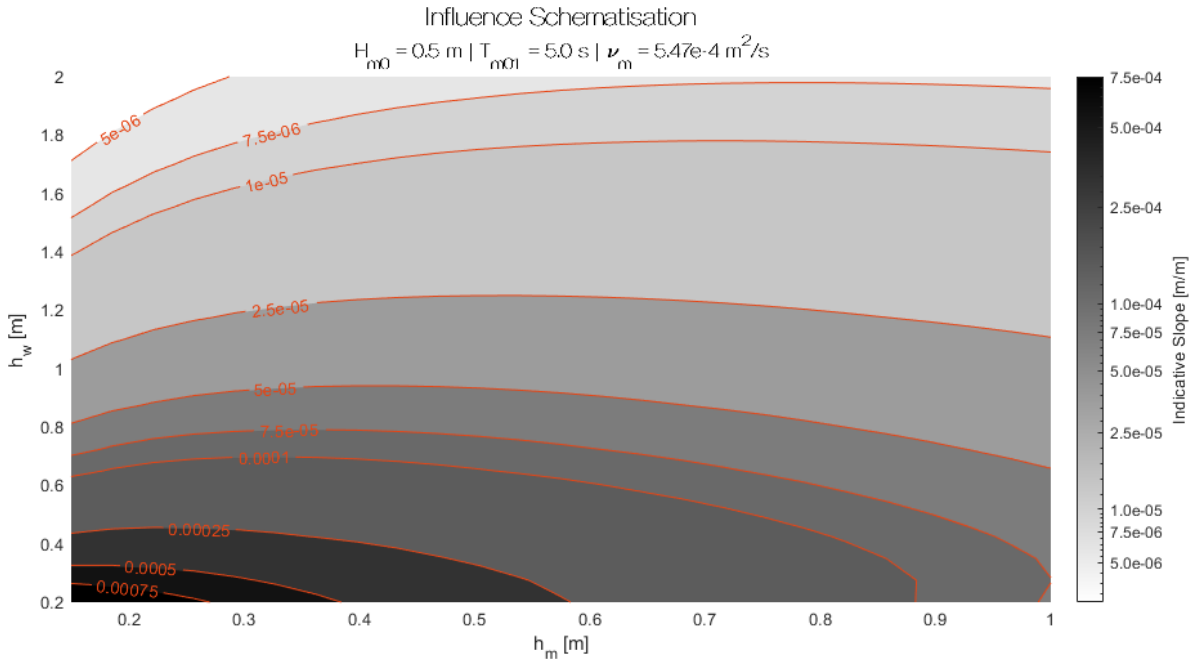

Figure 4.22: Indicative slope as calculated by the Simple Balance Model as a function of changes to the model schematisation via the parameters h_m and h_w. Other parameters have been kept constant as displayed at the top of the figure. The ticks of the colorbar are equal to the values of the isolines in the graph.

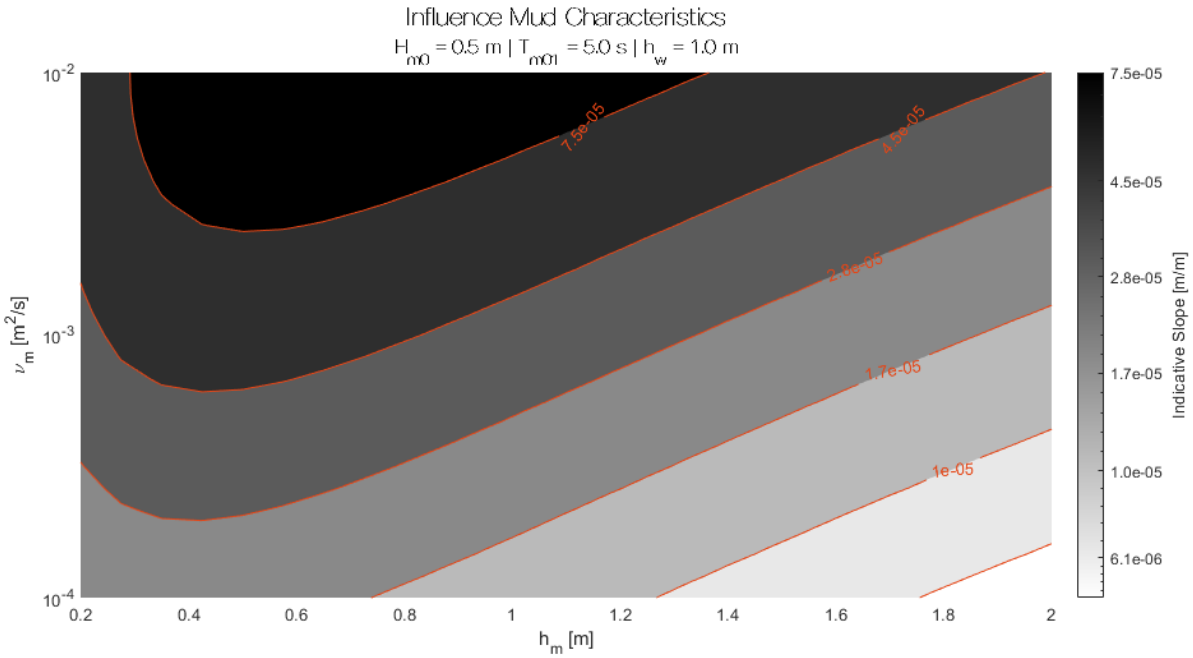

Figure 4.23: Indicative slope as calculated by the Simple Balance Model as a function of the mud characteristic via h_m and ν_m. Other parameters have been kept constant as displayed at the top of the figure. The ticks of the colorbar are equal to the values of the isolines in the graph.

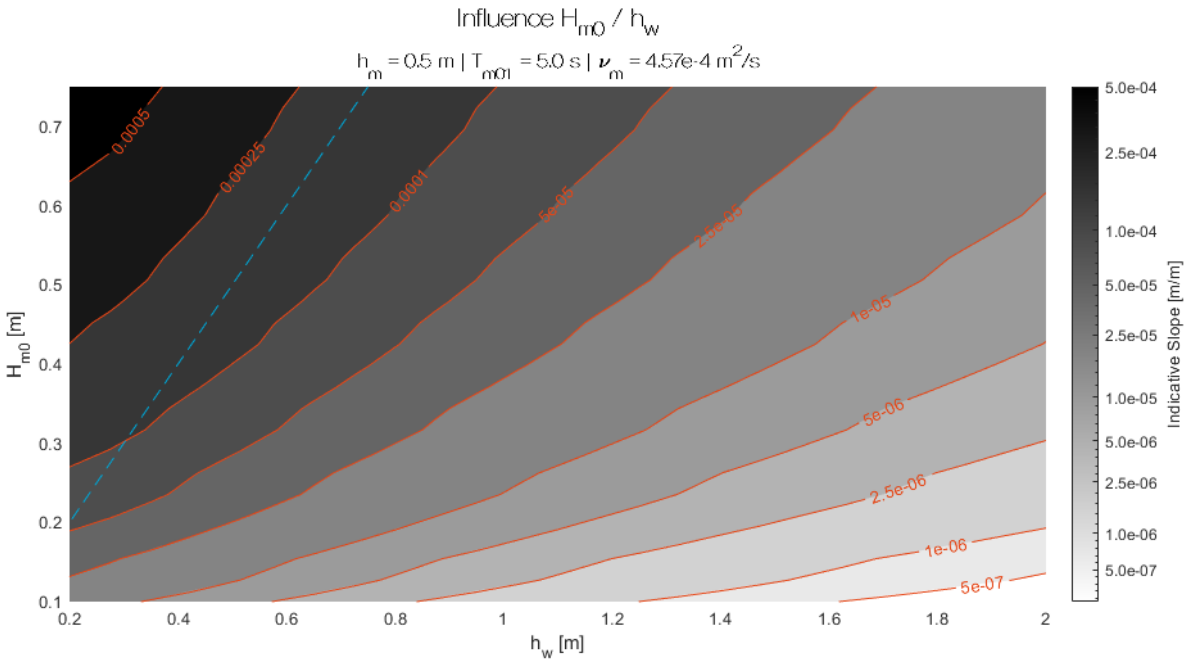

Figure 4.24: Indicative slope as calculated by the Simple Balance Model as a function of the wave height H_{m0} and and water depth h_w. Other parameters have been kept constant as displayed at the top of the figure. The dashed cyan line indicates $H_{m0}/h_w = 0$, left of which breaking is expected to occur. The ticks of the colorbar are equal to the values of the isolines in the graph.

this ratio, $H_{m0}/h_w < 1$, above which waves will start to break. As breaking waves are seldom observed in the study area, it is assumed that combinations of wave height and water depth above this ratio do not occur.

When applying this model to the reference case of section 4.1 using the monochromatic calibration parameters (assuming a horizontal bed here with a constant water depth on top of 0.76 m, calibrated to give the same wave damping as measured in the field), the maximum indicative slope that can be supported by the wave forcing is 1.23×10^{-5}. As described in section 3.3.5, an indication of the slope in the field can be calculated from the measured bathymetry. This results in a measured slope of 1.83×10^{-3}. It can be concluded that the combination of parameters measured in the field is not likely to be the direct cause of this observed slope.

Based on the performed analysis it is possible to determine a set of parameters that is more likely to achieve the measured slope. The wave height is increased to 0.75 m and for the mean wave period the matching optimum is chosen, $T_{m01} = 4.0$ s. Also based on this wave height, the optimum mud layer thickness is chosen, $h_m =$ 0.4 m. The viscosity is set to $\nu_m = 10^{-2}$ m^2/s. The water depth is set to 0.3 m. A simulation with these parameters results in an equilibrium slope of 1.70×10^{-3}, which is very close to the measured slope. The ratio between H_{m0} over h_w, however, is then larger than 1, which means that waves will have broken already before reaching the transect and thus such a ratio will never exist. When a more reasonable value for the water depth is chosen, $h_w = 0.75$ m, the equilibrium slope becomes 8.7×10^{-4}. It can thus be concluded that, for the measured slope in the field to be sustained, much larger waves are needed than were measured during the field campaign as well as a much larger viscosity (2 orders of magnitude).

4.3.2. Including Fluid Mud: Two-Layer Model

As this model makes use of both momentum balances (2.44) and (2.45), these balances are repeated here in (4.11) and (4.12) for convenience. A closer inspection of these equations reveals, that the term in (4.12) representing the effect of the free surface slope will generally be negative ($\partial\overline{\zeta}/\partial x > 0$ and $(1 - \rho_m/\Delta\rho) < 0$) and will thus reduce the gradient in the mud layer that is forced by the gradient in radiation stress within the layer. To achieve positive gradients in the interface level, the second term in balance (4.12) should be larger than the first term. Rewriting the momentum balances to (4.13), under the assumption that $S_x x, w$ (as retrieved from SWAN-Mud) is the radiation stress gradient that forces the water layer, a criterion (4.14) can be found assuring a positive gradient of the mud-water interface in shoreward direction, assuming that $\partial S_{xx,m}/\partial x < 0$.

$$\frac{\partial\overline{\zeta}}{\partial x} = -\frac{1}{g\rho_w h_{w0}}\frac{\partial S_{xx,w}}{\partial x} \tag{4.11}$$

$$\frac{\partial\overline{\xi}}{\partial x} = \left(1 - \frac{\rho_m}{\Delta\rho}\right)\frac{\partial\overline{\zeta}}{\partial x} - \frac{1}{g\rho_m h_{m0}}\frac{\partial S_{xx,m}}{\partial x} \tag{4.12}$$

substituting (4.11) in (4.12), using (4.8):

$$\frac{\partial\overline{\xi}}{\partial x} = -\left[\frac{1 - \rho_m/\Delta\rho}{g\rho_w h_w}\frac{\rho_w a^2}{\rho_m b^2} + \frac{1}{g\rho_m h_{m0}}\right]\frac{\partial S_{xx,m}}{\partial x} \tag{4.13}$$

$$\frac{\partial\overline{\xi}}{\partial x} > 0, \text{ if: } \left[\frac{1 - \rho_m/\Delta\rho}{g\rho_w h_w}\frac{\rho_w a^2}{\rho_m b^2} + \frac{1}{g\rho_m h_{m0}}\right] > 0 \tag{4.14}$$

The positivity criterion has been determined for the same ranges of parameters as used in section 4.3.1, however, the input values are based on 1 iteration of SWAN-Mud. This positivity criterion is negative for all modelled combinations of parameters (figures 4.25 to 4.28), hence no positive slope can exist in landward direction. This is further illustrated by the ratio between the interface and the surface slope (equation (4.15), slightly rewritten from equations (4.11) and (4.12)). Generally, the amplitude of the surface wave is much larger than the amplitude of the internal wave ($a \gg b$). Also, the thickness of the mud layer is of the same order of magnitude as the water depth, so that $h_m \approx h_w$, and the density

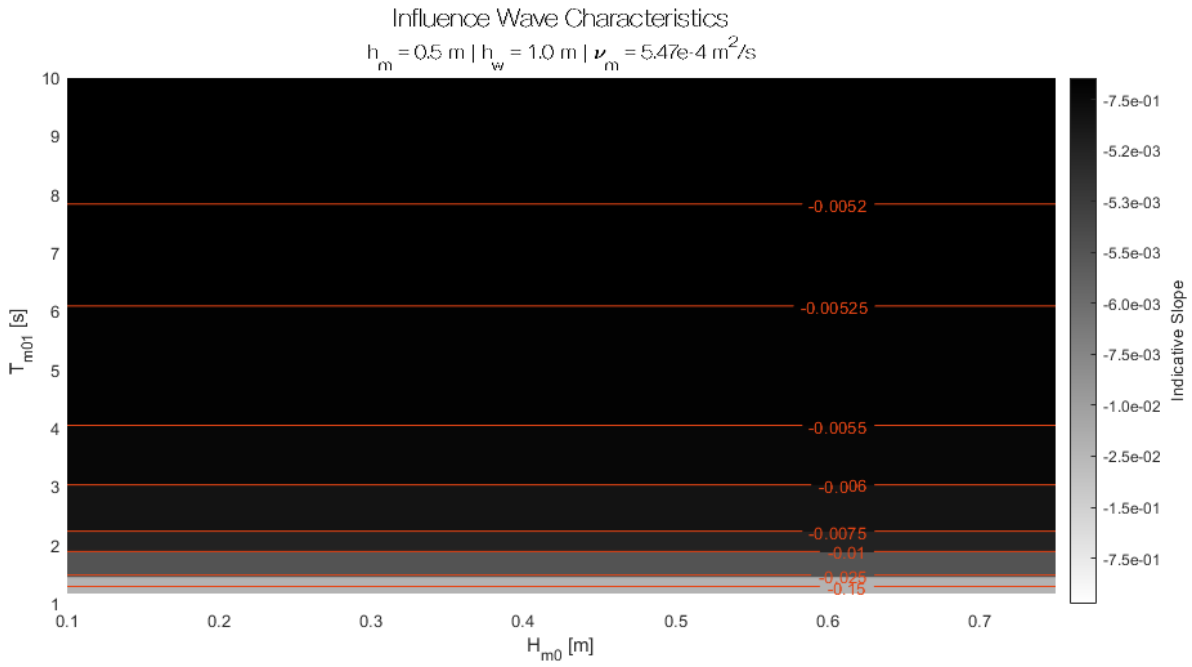

Figure 4.25: Positivity Criterion as calculated for the Two-Layer Model as a function of the wave parameters H_{m0} and T_m01. Other parameters have been kept constant as displayed at the top of the figure. The ticks on the colorbar are equal to the values of the isolines in the graph.

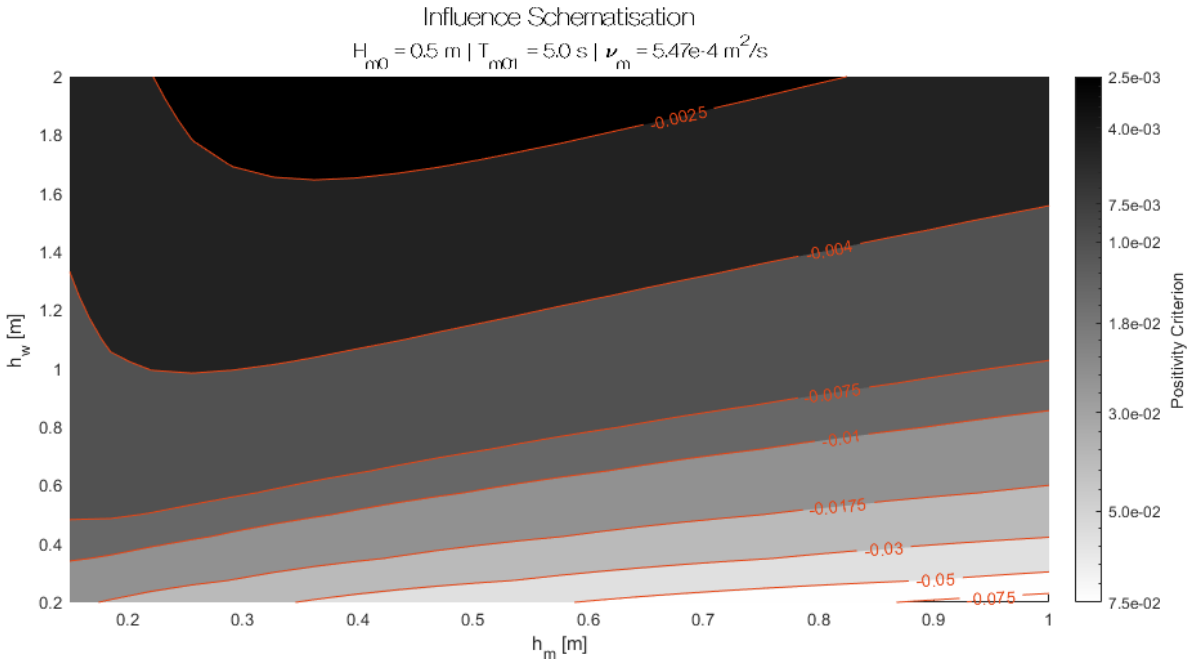

Figure 4.26: Positivity Criterion as calculated for the Two-Layer Model as a function of changes to the model schematisation via the parameters h_m and h_w. Other parameters have been kept constant as displayed at the top of the figure. The ticks on the colorbar are equal to the values of the isolines in the graph.

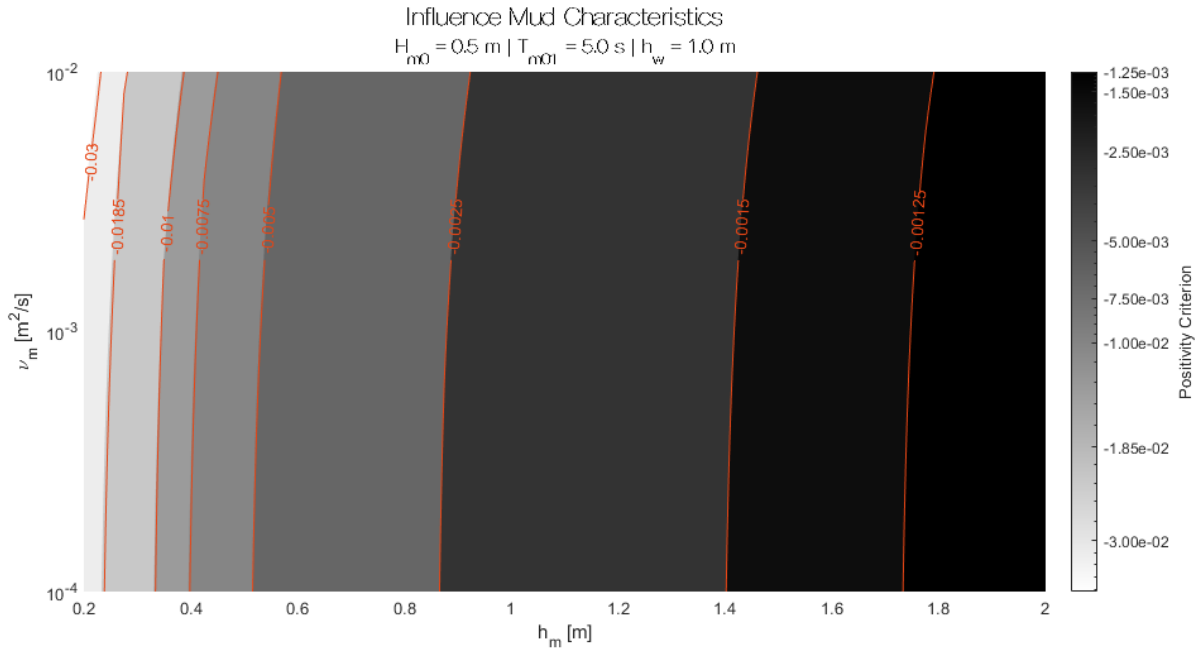

Figure 4.27: Positivity Criterion as calculated for the Two-Layer Model as a function of the mud characteristic via h_m and ν_m. Other parameters have been kept constant as displayed at the top of the figure. The ticks on the colorbar are equal to the values of the isolines in the graph.

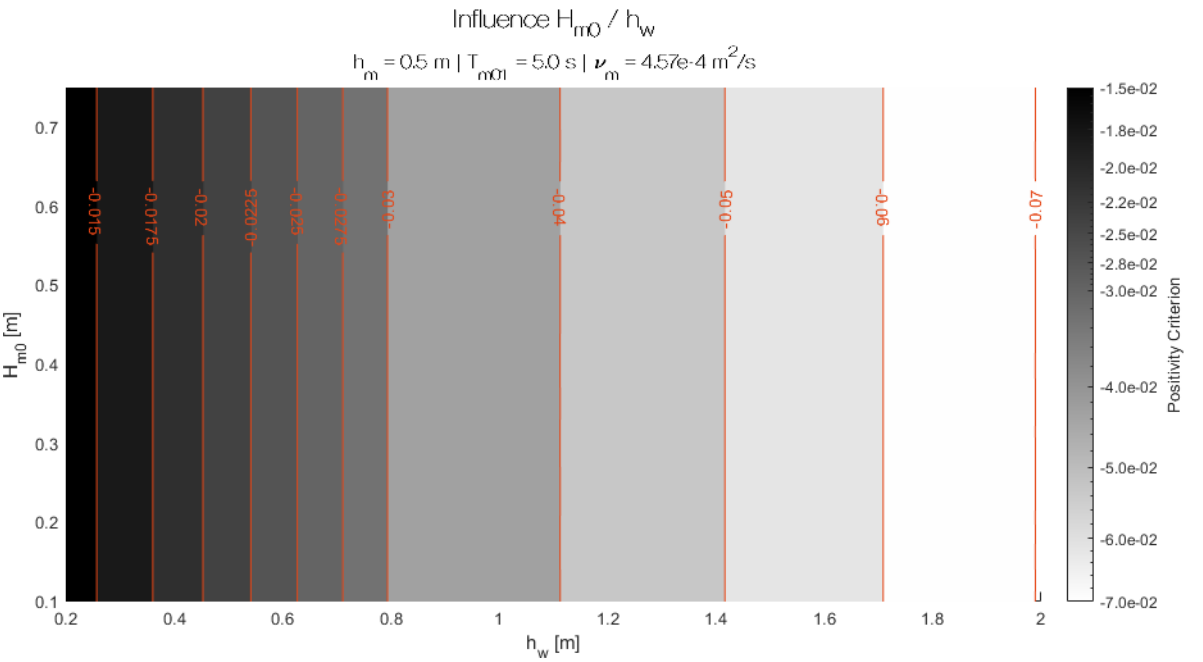

Figure 4.28: Positivity Criterion as calculated for the Two-Layer Model as a function of the wave height H_{m0} and and water depth h_w. Other parameters have been kept constant as displayed at the top of the figure. The ticks on the colorbar are equal to the values of the isolines in the graph.

of the mud layer is generally much larger than the difference between the mud layer density and the water layer ($\rho_m \gg \Delta\rho$). Hence, the ratio between the slope of the interface and the slope of the free surface predicts the same negative interface slopes at equilibrium. This implies that a sloping interface as observed in the field can only exist if the set-up of free surface is not maintained. In other words, the water has to flow away along the coastal boundary instead of piling up against it. This would induce a return current, much like, for example, rip currents along a sandy beach.

$$\frac{\partial\bar{\xi}/\partial x}{\partial\bar{\zeta}/\partial x} = 1 = \frac{\rho_m}{\Delta\rho}\left(1 - \frac{h_w}{h_m}\frac{b^2}{a^2}\right) \tag{4.15}$$

4.4. Application to Storm Conditions at Surodadi

As mentioned in chapter 3, the set-up of the mud layer is thought to be highly dependent on storm conditions, which occur during the north-western monsoon. Therefore, the calibrated SWAN-Mud model (section 4.2.5) was used to assess the response of the system to storm conditions. The Simple Balance Model (section 4.3.1) was used to calculate the indicative slope that can be sustained by the wave forcing.

4.4.1. Input Data

During the 2018 field campaign of BioManCO, no data was collected that resembles north-western monsoon conditions (chapter 3). During the 2017 field campaign, however, the NW monsoon started earlier in the year and therefore storm conditions were measured during that campaign. This data has not been collected at Surodadi (for an elaboration on the data, see Van Domburg (2018)) and therefore this data cannot be used directly in the model for Surodadi. As the measured transect during the 2017 campaign was at another location and the transect was set up differently, only the data from the seaward-most measurement station has been used. The storm with the highest waves has been selected from the dataset (2017-11-30 19:31:58 to 2017-12-02 11:06:19) and this data has been used as input for the SWAN-Mud model (figure 4.29). The depth at SW has been corrected with -0.5 m, so that the water depth is more comparable to the water depth measured during the 2018 campaign at Surodadi. As waves larger than the water depth are expected to have broken before reaching the transect, their wave heights have been corrected to the maximum value they can attain after breaking;

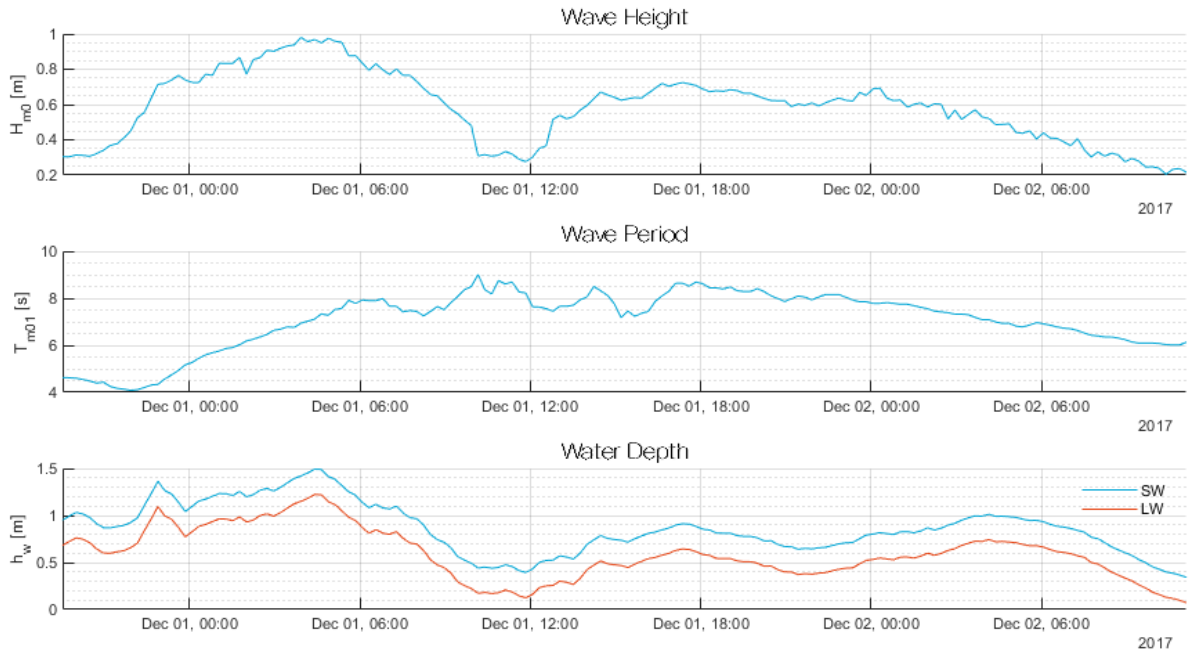

Figure 4.29: Measured storm conditions during the 2017 BioManCO field campaign (2017-11-30 19:31:58 to 2017-12-02 11:06:19) adapted for implementation in the SWAN-Mud model for Surodadi.

the water depth. The bathymetry was determined using the measured slope (1.83×10^{-3}, section 3.2.5) and the water depth from the storm data whilst assuming a constant free surface level. For the SWAN-Mud model, the monochromatic calibration values are used and the chosen wave forcing is a series of monochromatic waves.

4.4.2. Results

The storm is characterised by a strong increase in wave height (from 0.31 m to 0.97 m) and wave period (from 4 s to 8-9 s), indicating a transition from local wind waves to offshore, storm generated swell. For the purpose of calculating the damping by the viscous mud layer, a shoaling correction was applied to the incoming waves. The absolute damping of the waves over the transect is twice as high as during the SE monsoon and the sea breeze, although wave heights in the NW monsoon are generally larger than twice the characteristic wave heights during the SE monsoon and the sea breeze. The relative damping, however, expressed in terms of k_i, is of the same order of magnitude and shows peaks at the lowest water depths (figure 4.30). An explanation for the smaller damping can be sought in the effect

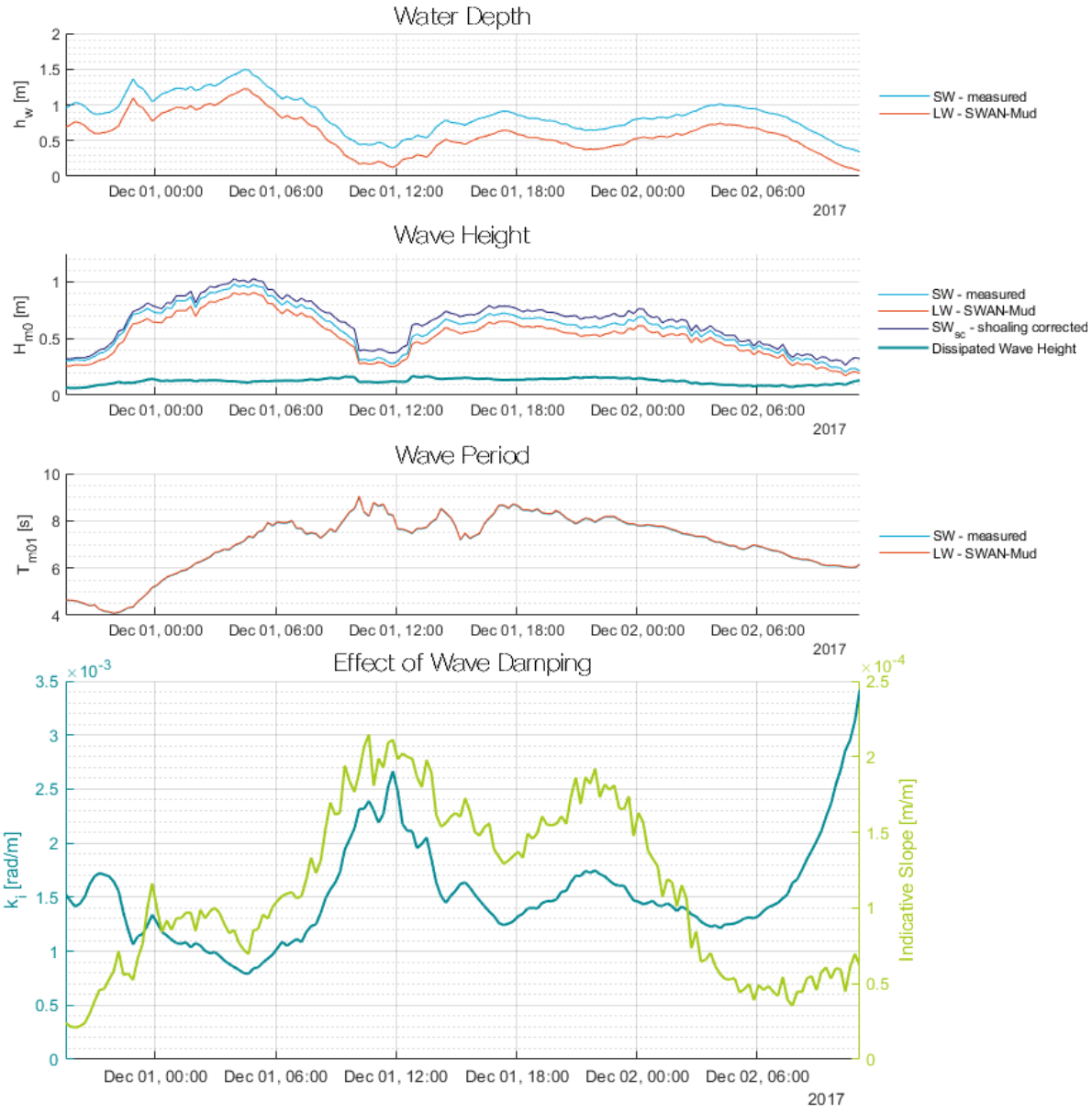

Figure 4.30: Results of the SWAN-Mud simulation and the Simple Balance Model for the conditions measured during a north-western monsoon storm.

of the wave period. In section 4.2.4 it was already shown that there is an optimum wave period T_{m01} for which the damping is most effective (figure 4.9. As the wave periods during the SE monsoon and the sea breeze were much closer to this optimum, a higher relative damping can be expected during those conditions. The indicative slope due to the wave forcing exhibits the same pattern as the relative damping k_i; a strong dependence on the water depth. The influence of the wave period is apparent as well; higher slope values occur for larger wave periods. It can be concluded that wave height is not the most important parameter determining the potential slope of the fluid mud interface. Even for the highest waves in this dataset, the indicative slope is at least one order of magnitude smaller than the slope found at Surodadi during the field campaign, 1.83×10^{-3} (which was measured during the calm season), indicating that the effect of the reduction in radiation stress in cross-shore direction contributes, but is not the only factor determining the slope observed in the field.

5

Discussion

The input for the modelling work is based on measurements that were carried out in a challenging environment, which consequently results in a number of uncertainties. In this chapter, these uncertainties within the collected dataset and their influence on the outcomes of this research are discussed. During the modelling stage, some important assumptions were made and these assumptions and their consequences are elaborated upon as well. The implications that the model results have on the hypotheses as proposed in section 2.4 are presented in the last part of this chapter.

5.1. Validity of measurements

Most of the analysis of the hydrodynamics was based on the data collected by the wave gauges. As further discussed in appendix C, there seems to be an error in the water level determined from the wave gauge measurements, especially for LW. The source of these errors has not been fully identified, although most problems seem to occur around low water. At this point, the calculated water level is lower than measured in the field (via an alternative measuring method). A crude correction method was implemented for these errors, but, as the source of the errors is not fully understood, a large uncertainty in these measured water levels remains. As the wave attenuation is strongly dependent on the water depth (Rogers and Holland, 2009), and the highest dissipation occurs with the lowest water depths (where the errors in the measurements are most apparent), the estimation of the damping is affected by the uncertainty in the water depth as well. The errors are estimated to have a maximum of 20 cm. From the sensitivity analysis, it is estimated that for the mud thickness implemented in SWAN-Mud (h_m =0.5 m), the deviation in the damping is about 4 percent points. For an incoming wave of H_{m0} =0.21 m at SW, this would mean an error in the calculated wave height at LW of about 0.008 m.

Large uncertainties are present as well in the measured bathymetry. The mud layer thickness following from these measurements is only correct in terms of order of magnitude. Also, the experiments performed by Deltares to determine the viscosity were carried out on a very limited number of samples and the exact location of acquisition of these samples is unknown. Additionally, due to the applied method during the measurements, a relationship between viscosity and density could not be determined from these samples. Therefore, the viscosity and the density of the mud layer at Surodadi cannot be estimated accurately. As indicated by Kranenburg et al. (2011), but also by Rogers and Holland (2009) and Traykovski et al. (2015), this uncertainty in the viscosity will have a significant impact on the model results, as well as the uncertainty in the fluid mud layer thickness. According to Rogers and Holland (2009), also the spatial distribution of the mud is an important factor. Although it is shown that different combinations of viscosity and mud layer thickness, whilst achieving the same amount of damping for a certain characteristic frequency, have different effects on other frequencies in the wave energy spectra, SWAN-Mud still manages to reproduce the observations in the field convincingly. Therefore, despite the large uncertainties in the mud characteristics, it is expected that predictions made by the model for storm events are still accurate. Because the effect of wave damping is assessed in this thesis over the length of the transect and not at different locations within the transect, the use of a constant mud layer thickness seems justified; the spatial variability of the mud layer thickness is accounted for in the

calibration. The uncertainty in the density of the mud is less important, according to Traykovski et al. (2015). The same follows from the sensitivity assessment in this thesis.

The measurements on which the observed slope of the mud-water interface is based are expected to be accurate. However, the calculation of this slope is based on the assumption that there is no horizontal gradient in the free surface level. If such a free surface slope was to be present during the measurements, it would be expected to have an upper limit of 0.0015 m. This would mean a reduction of the slope of the interface of 1.0×10^{-5}. In comparison with the measured slope of the interface, 1.83×10^{-3}, this is considered to be negligible. As little research has been done in field situations, it is difficult to assess how this value compares to other locations.

5.2. Validity of models

For each of the models used in this thesis, several assumptions were made. These assumptions determine the outcome of the model, so the choices made regarding these assumptions are far from arbitrary. Furthermore, some of the used models were developed within this research and therefore their validity is discussed as well.

5.2.1. SWAN-Mud

For the schematisation as implemented in SWAN-Mud, several simplifications were made, the most important of which are stated here and will be elaborated upon in the following sections.

- A 1D domain was used and waves were assumed to travel in the direction of the transect.
- All other processes (wave breaking, wind, refraction, bottom dissipation, white capping, non-linear wave-wave interactions) except dissipation by fluid mud were turned off.
- The characteristics of the mud layer were assumed to be constant over the transect.
- The viscosity was assumed to be constant (i.e. is not effected by changes in shear rate and thus acts as a Newtonian fluid).

1D Domain

The choice for a 1D domain excludes all 2D influences on the modelling results that might be present in the field. As these effects, like refraction, are generally assumed to be small (Van Prooijen et al., 2017), this choice seems justified. The consequence is that waves are assumed to propagate in the direction of the transect as well. When setting out the transect in the field, the dominant wave direction was estimated by eye. Therefore, the orientation of the transect might significantly differ from this dominant wave direction. The waves will then travel through the transect under an angle. This makes the model set-up in SWAN-Mud a less accurate representation of the field conditions. Although, based on the measured wind directions, the waves are expected to be in the direction of the transect and otherwise only under a slight angle, the measurements cannot confirm this as spatial information has not been collected. In future, this could be assessed using a third measurement pole or using ADVs for the entire duration of the field campaign to obtain directional spectra.

Selected Processes

As the interaction between waves and fluid mud is not well understood, it was decided to switch off all other processes in SWAN-Mud and focus on the dissipation by fluid mud only. For some processes, this is justified. Breaking, for example, is not expected to occur to a large extent within the transect, especially not for the wave conditions to which the model was calibrated and validated. Bottom dissipation was assumed to be negligible compared to the viscous dissipation. The effect of non-linear wave-wave interactions, white capping and wind were tested whilst calibrating the model to spectral input. The use of wind, white capping and quadruplet wave-wave interactions is coupled in SWAN-Mud. By including wind into the model, reproduction of the high frequency tail was better than models without wind. However, the implemented wind velocity to achieve this result was about twice as high as the measured wind velocity at the station at Semarang. As the prediction of the largest part of the spectrum did not improve significantly (only the tail), and because the simulations became noticeably slower to run, it was decided not to include wind. The triad wave-wave interactions resulted in a unrealistic increase of energy in the higher frequency range and was therefore discarded as well.

Constant Characteristics of the Mud Layer

As already stated in section 5.1, the mud layer thickness was assumed to be constant over the transect. This has an influence on the energy propagation over the transect; at locations with a thinner mud layer, there will be more damping of waves and hence less wave energy. This, in turn, will have an effect on the gradients in radiation stress over the transect and thus the slope that locally can be sustained by the wave action. However, because the model is calibrated for the damping averaged over the length of the transect, this assumption does not change the outcome of the predictions. The same holds for the density and the viscosity of the mud. Furthermore, both of these characteristics were assumed to be constant over the thickness of the layer as well. Generally, it is expected that the viscosity and density will increase with depth. As this distribution over depth will also vary over the transect, it is very difficult to include these parameters properly into a model and predict the damping accurately at each location along the transect. Again, because the model is calibrated for the damping over the length of the transect, the effects of these inaccuracies will be limited.

Implemented viscosity

The level of viscosity used in the monochromatic calibration as well as the level of viscosity determined from the samples is smaller than found in most literature describing field conditions at other locations in the world (Rogers and Holland, 2009; Traykovski et al., 2015; Winterwerp et al., 2007). However, these viscosities were generally linked to higher densities. When considering that the viscosity decreases with a decreasing bulk density (Kranenburg, 1994), the values used in this research actually compare quite well to literature. In SWAN-Mud, the fluid mud layer is treated as a highly viscous, Newtonian fluid. Therefore, the effect of the shear rate in the mud layer induced by the waves is not accounted for. This is valid for high shear rates, but as mud actually behaves like a Bingham fluid, this is not valid for low shear rates (Hsu et al., 2013). As the measurements during the field campaign were done under low energetic conditions, the shear rates can be expected to be low as well. A constant viscosity will therefore not be able to describe the behaviour of the system correctly, especially because the calibration was done on low energetic conditions as well. A more elaborate data set of field measurements is needed to verify this. Hsu et al. (2013) also suggest that an enhanced constant bottom shear stress can be used to model wave attenuation on a large scale. However, this only works when the measured damping rate and the bottom shear stress are well correlated, which is not the case for low-energetic wave conditions. Therefore, such a parametrisation cannot be used for the wave conditions measured at Surodadi for which the model is calibrated and validated. This is coherent with the results of this thesis.

5.2.2. Simple Balance Model

This simple algorithm assumes an equilibrium between a cross-shore, shore supported pressure gradient in the mud layer (hence, a set-up of the interface) and the radiation stress gradient caused by the damping of waves. It should be noted that it is likely that, in the field, equilibrium has not yet been reached as wave conditions change constantly. As stated in the hypotheses as well (section 2.4), the mud behaves like a non-Newtonian fluid, hence there might be a lag between forcing and response, or, because of a yield stress, no response at all. It was expected that the slopes in the field would be smaller than would follow from these calculations. This, however, was not the case; the slope, when measured, was larger than the calculated slopes. The observed slope can only by calculated by the model if a severely increased viscosity and relatively large waves are implemented. This either indicates that other processes play a role as well in creating and sustaining these slopes, or that the radiation stress is not accurately estimated by using the ratio between the surface and the internal wave amplitudes. With sufficient laboratory or field measurements of velocity distributions in the mud layer, an indication of the order of magnitude of the radiation stress could be given, for example using the expressions derived in section 2.3.3. These values could be used to validate the approach taken to determine the radiation stress gradient within the Simple Balance Model. Furthermore, given the significant differences in results with the Two-Layer Model, it may be concluded that neglecting the influence of the slope in the water layer may not be justified and the schematisation as presented in the Simple Balance Model is actually too simple. The validity of this model cannot be checked without a series of laboratory or field measurements.

5.2.3. Two-Layer Model

In the Two-Layer Model, the Simple Balance Model has been extended by assuming that the cross-shore gradient of the free surface level does not necessarily have to be negligible. This introduces an extra term in the momentum equation of the mud layer. This model is not able to reproduce the slope observed in the field. The influence of the gradient in the free surface is too large and only negative slopes result for the interface level. It may, therefore, be concluded that a positive slope of the interface as observed in Demak may only occur over limited longshore distances. This allows water to flow away transversely. In that case, the gradient of the free surface level would not exist and the Simple Balance Model could be used to predict the slope of the interface. Another explanation can be sought in the determination of the radiation stress in the mud layer.

5.3. Implications of model results for hypotheses

In the following sections, the implications of the model results for the hypotheses are presented. These implications are based on the Simple Balance Model, assuming that this model describes the relevant processes accurately.

5.3.1. Hypothesis 1: Viscous mud layer

The slopes predicted by the Simple Balance Model are significantly smaller than the observed slope during the measurement campaign. Taking into account the uncertainties in the measurements and the fact that the change in slope over the time between the measurements is considered to be small (section 3.2.5), an instantaneous response of the slope to prevailing wave conditions as presented by this hypothesis is highly unlikely.

5.3.2. Hypothesis 2: Plasto-viscous mud layer

As the slope of the mud layer is not expected to change significantly over the assessed deployment period and the wave conditions during this period can be considered to be calm, the sustained slope could be explained by the yield stress of the mud. Based on the yield stress calculated from the mud samples, whilst assuming a constant thickness of 0.5 m over the transect, a simple balance between gravity and yield stress (equation (5.1)) gives, in theory, a slope of 3.8×10^{-3}. This slope is within the same order of magnitude as the slope measured during the measurement campaign and could be sustained without the presence of a radiation stress gradient.

$$\frac{\partial \bar{\xi}}{\partial x} = \frac{\tau_y}{g\Delta\rho\overline{h_m}} \tag{5.1}$$

When this same yield stress has to be overcome by the wave force generated by the damping of the surface waves, the indicative slope (calculated by the Simple Balance Model) can be used as an indicator whether initiation of motion within the layer will be the case or not. A value for the slope smaller than 3.8×10^{-3} indicates that the wave force is not sufficient to overcome the yield stress. As this is the case for the wave conditions during the deployment at Surodadi, this explains the little change measured in the slope over this period. This conclusion is further supported by the data of the mud floaters.

5.3.3. Hypothesis 3: Plasto-viscous mud layer and strength development

Without more extensive measurements, it is difficult to draw any conclusions on the validity of this hypothesis. Considering that the measurement campaign took place at the end of the calm season, a build-up of large slopes over this season is not expected. Assuming this hypothesis is true, the measured slope must be a remainder of the last storm season. For the next storm season, two possible outcomes are predicted. The first possibility is the destruction of the slope of last season due to erosion by a major storm or a decrease in bulk density and/or viscosity and thus in yield stress. A new fluid mud layer will form and the slope will be rebuild. The second possibility is the continuation of the build-up of the slope formed during the last storm season, eventually leading to a build out of the coast in the form of mud flats. When these mud flats have reached a certain level, species of mangroves will be able to colonise the mud flats, fixating the build-out of the shoreline.

The second possibility, however, is not supported by the calculated slopes by the Simple Balance Model for the storm season.Based on these values, the storm will not be able to overcome the yield stress and will hence not push up the layer, on the assumption that the fluid mud will be mobilised over the entire depth of the mud layer. The yield stress, however, is not constant over the depth of the mud layer, but increases with depth. It might therefore be that the waves are able to set the upper part of the mud layer in motion. As this is a smaller volume of mud to push up in a slope, the waves will be able to sustain a larger slope as well. Furthermore, a thinner slope means a higher rate of damping. Therefore, the gradient in radiation stress is larger and thus the wave force that is sustaining the slope is larger as well.

6

Conclusion & Recommendations

The objective of this thesis is to assess wave damping as the driving mechanism of a set-up of the fluid mud layer at the coast of Demak and to identify under what conditions such a set-up can exist. Using the results of the associated field campaign and the consecutive modelling of the wave-mud interaction, the main findings are presented here, under the relevant research questions (leading to a final conclusion) and recommendations for further research.

6.1. Characteristic hydrodynamics on a timescale of days/weeks

The hydrodynamics are characterised by a strong daily pattern. This pattern is observed clearly in the wind data and can be attributed to the south-eastern monsoon and the sea breeze. The waves during the sea breeze are locally generated and are therefore shorter. An increase in wave input into the system can be observed during the sea breeze over the full range of relevant frequencies. The waves during the sea breeze are generally higher than the waves during the south-eastern monsoon. Although the south-eastern monsoon is directed seaward, the predominant waves are travelling shoreward. These waves are swell waves generated during the sea breeze period. The significant wave height shows a sharp increase at the start of the sea breeze and a much more gentle transition towards the south-eastern monsoon. The same sharp transition can be observed in the mean wave period at the start of the sea breeze, as well as a gradual increase over the transition to the south-eastern monsoon. These characteristics are valid for the calm season. The behaviour of the system changes when the storm season starts and the north-western monsoon starts to prevail. No data was collected on this period during the field campaign.

6.2. Effect of the fluid mud layer on waves

A strong attenuation can be observed over the fluid mud layer that is located at the measurement locations. This dissipation of wave energy in the viscous mud layer varies largely with the wave period as well as with the water depth; most relative dissipation is observed during low tide. In general, a larger wave height means a higher damping rate, but this is not the most important factor. The amount of damping is strongly influenced by the viscosity of the mud layer and the thickness of the mud layer, the influence of the density, however, is very small. A thin mud layer with a high viscosity will yield a much higher attenuation of the surface waves than a thick mud layer with a small viscosity.

The attenuation can be modelled sufficiently well with SWAN-Mud. Using a simple monochromatic wave forcing gives comparable results to using the full sea state (by means of a spectrum). The reproduction of the damping of the sea states leaves room for improvement, especially for frequencies further away from the peak frequency. Different combinations of mud characteristics have different results at various wave frequencies. It is therefore important to determine these characteristics with sufficient accuracy in the area that is modelled.

6.3. Expected dynamics of the fluid mud layer on a timescale of days/weeks

The transfer of energy from the water layer to the mud layer is determined by the internal wave motion on the interface. The ratio between the amplitudes of the internal wave and the surface wave is an important parameter and so is the phase lag between these waves. Based on the model results, it is expected that a set-up of the mud layer only occurs when the forcing by waves is higher than the yield stress of the mud layer. It is also expected that the waves that are able to cause stresses above this threshold will occur more often in the storm season than during the calm season (in which the measurements for this thesis were done). Due to the shear-thinning behaviour of the mud, the mud layer will strengthen over time under wave forcing and will be able to sustain larger slopes as the time progresses.

The proposed model formulation to calculate this set-up has not given convincing results as of yet. The calculated slopes are too little in comparison with the measured slope in the field. Too few field measurements are available to verify the results of this model. As it is based on an equilibrium between a pressure gradient (caused by a slope in the mud layer) and the radiation stress gradient, it assumes an instantaneous response of the layer to a change in wave conditions. This, however, is unlikely, as mud behaves like a Bingham fluid. A more likely scenario is thus the presence of a lag in the response of the layer due to the viscous properties of the mud. Another consequence of these rheological properties is that the forcing needs to overcome a certain threshold (the yield stress) to be able to set the layer in motion. Therefore, only part of the waves is able to contribute to the formation of the slope. The slope does not necessarily have to be sustained by the gradient in radiation stress. The yield stress is able to balance the pressure gradient caused by the slope in the mud layer as well. This explains the observed slopes in the field. Because of the lag in response and the yield stress of the mud, the interface level (and the slope thereof) is not expected to change much over a timescale of days to weeks under the calm conditions measured during the field campaign.

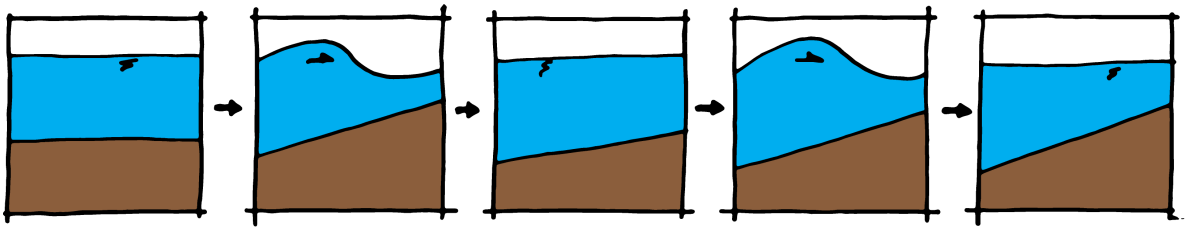

Figure 6.1: Expected behaviour of the fluid mud layer. The mud layer strengthens over the season, the yield strength increases. Therefore, the slopes that can be sustained by the yield stress will become larger over time. Whenever the wave forcing is smaller than the yield stress, that slope will not change.

6.4. Long-term wave effects on fluid mud dynamics on timescales of months/years

The long term development of the system is very strongly dependent on the development of the yield strength in the mud layer. The yield stress is expected to increase over time. Therefore, near a coastal boundary, the slope of in the interface in shoreward direction becomes larger in time. This requires a transport of mud in shoreward direction over the storm season, supplying the coast. Eventually, on the seasonal timescale, this supply of sediment can lead to a build-out of the shoreline in the form of mud flats. Under certain conditions (see, for example, Van Domburg (2018)), these mud flats can then be colonised by mangrove species, fixating the build-out of the shoreline.

6.5. Final Conclusion

In theory, the damping of waves due to a dissipative fluid mud layer can generate a cross-shore gradient in the interface between water and mud. With the current models, however, it is not possible to reproduce the order of magnitude of the gradient as derived from field data. It is therefore expected that the non-Newtonian character of the mud plays an important role in the interface dynamics and it is

plausible that the behaviour of the interface is more complex than just a balance between a radiation stress gradient and a pressure gradient. Up until now, this non-Newtonian behaviour (and in particular the yield stress) has not been included yet in any models calculating wave damping or the slope of the mud layer. Including at least the yield stress would mean a large step forward; it would provide a mechanism to sustain the slopes, formed by the wave action, in calmer periods.

6.6. Broader Perspective

As discussed in section 1.1.4, the current solution to solve the erosion problem at the coast of Demak is the construction of hybrid dams to capture sediment and to restore the coastal profile. As shown, however, in this thesis, it is plausible that the observed slope of the interface of the fluid mud layer is wave driven, indicating transport of sediment within this layer towards the coast. Building a hybrid dam would disrupt this process. Essentially, the hybrid dam would form the coastal boundary against which the mud will be pushed up. Consequently, the water and sediment will pass less easily through these dams if more mud is being pushed up over time. Therefore, the efficiency of the dams will decrease over time. Although accretion will occur in front of the dams, these new mud flats will stay disconnected from land behind the dams. As waves partly reflect on these structures and flow along the dams has been observed (Borsje, 2017), the mud accumulating in front of these dams might even be eroded and transported elsewhere. As follows from the results of the Two-Layer Model, a set-up of the interface may only exist when a set-up of the free surface is not present. In that case, water will flow away transversely. In the case of a hybrid dam acting as a coastal boundary, this would mean that a complicated flow structure might exist in front of this dam. This, in turn, may have an effect on the effectiveness of the dam in capturing sediment. As shown by Borsje (2017), the flow structures observed in field experiments are not well understood nor modelled with sufficient accuracy. The development of the slope of the interface is expected to be linked to a seasonal or even yearly timescale. This is the same timescale as for the sedimentation behind the hybrid dams and the effects of these processes may thus interfere.

6.7. Recommendations

The following recommendations can be made on the basis of the executed fieldwork and the use of SWAN-Mud to reproduce this fieldwork;

- The use of the specific echosounders as applied in this research for the purpose of measuring the internal wave characteristics is strongly discouraged. The memory capacity of especially the AA400 is too small to measure internal waves at a sufficiently small sampling frequency for a sufficiently long period of time. These instruments are better suited for long term monitoring of the mud interface. A proper investigation into the settings for muddy substrates is required before deploying these in muddy environments. Such a long term deployment, however, would be very useful to gain insight into the development of the slope in the mud layer throughout the year and over the different seasons.

- Apart from the measurements of Jaramillo et al. (2009) and Traykovski et al. (2015) in Florida, not much data has been collected on internal waves in the field. A measurement campaign, as carried out by Traykovski et al. (2015), would be a major advantage for the research into the behaviour of the muddy coasts of Indonesia. During this campaign, the lutocline as well as the consolidated bed level were measured for an extended period of time at a high sampling frequency (2 Hz) using acoustic backscatter profilers. Furthermore, velocities within the mud layer were measured using a series of single beam pulse-coherent acoustic Doppler profilers. With these measurements, not only could the velocity profiles over depth be mapped in time, but also wave spectra for the mud layer could be generated and be compared to spectra of the wave motion at the free water surface. For this particular thesis, these kinds of measurements could have been useful as well, as the radiation stresses in the mud layer could have been calculated directly from the measurements and the proposed models could have been validated. Although preferably in the field, these measurements could also be carried out in a flume.

- A more realistic implementation of the bathymetry and mud layer thickness could improve the model performances. This will account for the spatial distribution of the damping better, remov-

ing one variable from the problem. The likely viscosity range can then be predicted with more certainty. One way to acquire this data would be by using a double band acoustic backscatter profiler along the transect, as described in the previous bullet point. This instrument could, for example, be mounted to a small fishing boat and be linked with GPS measurements and an acceleration sensor (to compensate the measurements for the movement of the boat). When implemented more often, this will also provide information on the rate of change in the spatial distribution of the mud.

- A more accurate and extensive measurement of the viscosity, density and yield stress is desirable. It would be especially beneficial to be able to make the connection between density and viscosity.
- As the wave damping is highly dependent on wave frequency and the models are not predicting the measured energy density well for certain frequency bands, it might be worthwhile to investigate where these differences originate from.
- If any of the balance models are to be used in further research, they should be thoroughly validated. Also, the validity of neglecting certain terms in the momentum balances should be looked at more thoroughly. A series of lab experiments investigating the movement of the mud under different wave conditions and for different combinations of mud characteristics would be useful for this.
- An interesting further development of SWAN-Mud could be to couple this wave model and its fluid mud module with Delft3D. In this way, the mud layer dynamics due to waves can be linked to flow and changes in morphology.

Bibliography

Badan Meteorologi Klimatologi Dan Geofisika. AWS Monitoring Semarang, 2018. URL http://202.90.199.132/aws-new/monitoring/3000000014.

R. M. Borsje. Assessing current patterns behind hybrid dams: Demak, Indonesia. Additional graduation work, Delft University of Technology, Delft, 2017.

M. A. Foda, J. R. Hunt, and H.-T. Chou. A nonlinear model for fluidization of marine mud by waves. *Journal of Geophysical Research*, 98(C4):7039–7047, 1993.

H. G. Gade. Effects of a nonrigid, impermeable bottom on plane surface waves in shallow water. *Journal of Marine Research*, 16(2), 1958.

Google. [Satellite images of Java and the Demak coastal area], 2017. URL https://www.google.nl/maps/@-6.8709896,110.7709058,575893m/data=!3m1!1e3.

W. Y. Hsu, H. H. Hwung, T. J. Hsu, A. Torres-Freyermuth, and R.Y. Yang. An experimental and numerical investigation on wave-mud interactions. *Journal of Geophysical Research: Oceans*, 118:1126–1141, 2013.

S. Jaramillo, A. Sheremet, M. A. Allison, A. H. Reed, and K. T. Holland. Wave-mud interactions over the muddy Atchafalaya subaqueous clinoform, Louisiana, United States: Wave-supported sediment transport. *Journal of Geophysical Research*, 114(C04002), 2009.

G. H. T. Kimble. Tropical land and sea breezes. *Bulletin of the American Meteorological Society*, 27 (3):99–113, 1946.

C. Kranenburg. The fractal structure of cohesive sediment aggregates. *Estuarine, Coastal and Shelf Science*, 39:451–460, 11 1994. doi: 10.1016/S0272-7714(06)80002-8.

W. M. Kranenburg. Modelling wave damping by fluid mud: Derivation of a dispersion equation and an energy dissipation term and implementation into SWAN. Master's thesis, Delft University of Technology, Delft, 2008.

W. M. Kranenburg, J. C. Winterwerp, G. J. de Boer, J. M. Cornelisse, and M. Zijlema. SWAN-Mud: Engineering model for mud-induced wave damping. *Journal of Hydraulic Engineering*, 137(9):959–975, 2011.

M. S. Longuet-Higgins. Longshore currents generated by obliquely incident sea waves: 1. *Journal of Geophysical Research*, 75(33):6778–6789, 1970.

M. S. Longuet-Higgins and R. W. Stewart. Radiation stresses in water waves; a physical discussion, with applications. *Deep-Sea Research*, 11:529–562, 1964.

W. H. McAnally, C. Friedrichs, D. Hamilton, E. Hayter, P. Shrestha, H. Rodriguez, A. Sheremet, and A. Teeter. Management of fluid mud in estuaries, bays and lakes I: Present state of understanding character and behaviour. *Journal of Hydraulic Engineering*, 133(1):9–22, 2007.

A. J. Mehta, S.-C. Lee, and Y. Li. Fluid mud and water waves: A brief review of interactive processes and simple modelling approaches. Technical report, U.S. Army Corps of Engineers, Gainesville, Florida, July 1994.

U. Motohiko and T. Shintani. Transformation, attenuation, setup and undertow of internal waves on a gentle slope. *Journal of Waterway, Port, Coastal and Ocean Engineering*, 132(6):477–486, 2006.

T. J. F. van Domburg. Identifying windows of opportunity for mangrove establishment on a mud coast. Master's thesis, Delft University of Technology, Delft, 2018.

B. C. van Prooijen, D. S. van Maren, C. Chassagne, and J. C. Winterwerp. CIE4308: Fine sediment dynamics. Lecture notes, 2017.

P. J. de Wit. *Liquefaction of cohesive sediments caused by waves*. PhD thesis, Delft University of Technology, 1995.

H. N. Rodriguez. *A mechanism for non-breaking wave-induced transport of fluid mud at open coasts*. PhD thesis, University of Florida, May 1997.

H. N. Rodriguez and A. J. Mehta. Considerations on wave-induced fluid mud streaming at open coasts. In K. S. Black, D. M. Paterson, and A. Cramp, editors, *Sedimentary Processes in the Intertidal Zone*, Special Publication 139, pages 177–186. Geological Society, London, 1998.

W. E. Rogers and K. T. Holland. A study of dissipation of wind-waves by mud at Cassino Beach, Brazil: Prediction and inversion. *Continental Shelf Research*, 29:676–690, 2009.

M. A. Ross and A. J. Mehta. On the mechanics of the lutocline and fluid mud. *Journal of Coastal Research*, 1989.

A. Sheremet and G. W. Stone. Observations of nearshore wave dissipation over muddy sea beds. *Journal of Geophysical Research*, 108(C11), 2003.

A. Sheremet, S. Jaramillo, S.-F. Su, M. A. Allison, and K. T. Holland. Wave-mud interaction over the muddy Atchafalaya subaqueous clinoform, Louisiana, United States: Wave processes. *Journal of Geophysical Research*, 116(C06005), 2012.

B. P. Smits. Morphodynamic optimisation study of the design of semi-permeable dams for rehabilitation of a mangrove-mud coast: A case study of the Building-with-Nature project in Demak, Indonesia. Master's thesis, Delft University of Technology, 2016.

S. A. J. Tas. private communications, 2018.

F. Tonneijck, J. C. Winterwerp, B. van Weesenbeeck, R. Bosma, D. Debrot, Y. R. Noor, and T. Wilms. Building with Nature Indonesia - Securing eroding delta coastlines. Design and Engineering Plan, Ecoshape, 2015.

P. Traykovski, J. Throwbridge, and G. Kineke. Mechanisms of surface wave energy dissipation over a high-concentration sediment suspension. *Journal of Geophysical Research*, 120:1638–1681, 2015.

G. Vledder, M. Zijlema, and L. Holthuijsen. Revisiting the JONSWAP bottom friction formulation. *Coastal Engineering Proceedings*, 1(32), 2011.

J. C. Winterwerp, R. F. de Graaff, J. Groeneweg, and A. P. Luijendijk. Modelling of wave damping at guyana mud coast. *Coastal Engineering*, 54:249–261, 2007.

J. C. Winterwerp, G. J. de Boer, G. Greeuw, and D. S. van Maren. Mud-induced wave-damping and wave-induced liquefaction. *Coastal Engineering*, 64:102–112, 2012.

J. C. Winterwerp, P. L. A. Erftemeijer, N. Suryadiputra, P. van Eijk, and L. Zhang. Defining eco-morphodynamic requirements for rehabilitating eroding mangrove-mud coasts. *Wetlands*, 33:515–526, 2013.

J. C. Winterwerp, B. van Wesenbeeck, J. van Dalfsen, F. Tonneijck, A. Astra, S. Verschure, and P. van Eijk. A sustainable solution for massive coastal erosion in Central Java: towards regional scale application of Hybrid Engineering. Discussion paper, Deltares and Wetlands International, 2014.

J. C. Winterwerp, D. S. van Maren, T. van Kessel, C. Chassagne, and B. C. van Prooijen. *Fine sediments in the marine environment – from fundamentals to modeling*. World Scientific, 2019.

J.C. Winterwerp. private communications, 2018.

List of Symbols

$\Delta\rho$	difference in density between the water and mud layer	[kg/m^3]
$\dot{\gamma}_s$	shear rate	[Hz]
γ	relative density difference	[-]
γ_s	shear strain	[rad]
$\hat{p}_w$	complex amplitude of the pressure in the water layer	[Pa]
ν_m	viscosity of mud	[m^2/s]
ω	angular wave frequency	[rad/s]
$\overline{P}$	The total work done per unit area during a wave period T	[J/m^2]
ϕ	phase difference between the surface wave and the internal wave	[rad]
ρ	density (in case of a single layer system)	[kg/m^3]
ρ_m	density of mud	[kg/m^3]
ρ_w	density of water	[kg/m^3]
τ	shear stress	[N/m^2]
τ_y	yield shear stress	[N/m^2]
$\tau_{B,x}$	bottom shear stress in x-direction	[N/m^2]
$\tau_{i,x}$	shear stress on the interface in x-direction	[N/m^2]
$\tau_{W,x}$	wind shear stress in x-direction	[N/m^2]
θ	mean wave direction, nautical convention	[°]
ξ	displacement of the free surface	[m]
ξ_0	complex amplitude of the displacement of the interface	[m]
ζ	displacement of the free surface	[m]
a	amplitude of the displacement of the free surface	[m]
b	amplitude of the displacement of the interface	[m]
C_b	JONSWAP bottom fritcion coefficient	[m^2/s^{-3}]
c_g	group velocity	[m/s]
c_θ	turning rate in time of the wave energy over directions	[°/s]
E	total wave energy per unit area	[J/m^2]
f	(temporal) wave frequency	[Hz]
G	shear modulus	[Pa]
g	gravitational acceleration	[m/s^2]

G'	elastic shear storage modulus	[Pa]
G''	viscous shear loss modulus	[Pa]
h_m	instantanious distance from the consolidated bottom to the interface	[m]
h_w	instantanious distance from the interface to the free surface	[m]
h_{LW}	water depth at LandWard measurement pole	[m]
h_{SW}	water depth at SeaWard measurement pole	[m]
H_{m0}	significant wave height based on the zero moment of the variance density spectrum	[m]
h_{m0}	distance from the consolidated bottom to the interface at still water conditions, also referred to as 'mud layer thickness'	[m]
$H_{s,\text{LW}}$	significant wave height at LandWard measurement pole	[m]
$H_{s,\text{SW}}$	significant wave height at SeaWard measurement pole	[m]
H_s	see H_{m0}	[m]
h_{w0}	distance from the interface to the free surface at still water conditions, also referred to as 'water depth'	[m]
i	imaginary unit $\sqrt{-1}$	[-]
K	consistency index in the Herschel-Bulkley model	[N s^n /m^2]
k	complex wave number	[rad/m]
k_i	imaginary part of the complex wave number, also referred to as 'relative damping'	[rad/m]
k_r	real part of the complex wave number	[rad/m]
L	length of measurement transect	[m]
n	flow index in the Herschel-Bulkley model	[]
p	total pressure in case of a single layer system	[Pa]
p_0	pressure without the presence of waves	[Pa]
p_m	total pressure in the (lower) mud layer	[Pa]
p_w	total pressure in the (upper) water layer	[Pa]
p_{wave}	dynamic wave pressure (due to the orbital motion of waves)	[Pa]
S_{mud}	sink term of mud-induced dissipation	[J/m^2/s]
S_{tot}	total source and sink term in wave energy balance	[J/m^2/s]
$S_{xx,m}$	radiation stess in the (lower) mud layer in x-direction	[N/m]
$S_{xx,w}$	radiation stess in the (upper) water layer in x-direction	[N/m]
S_{xx}	total radiation stess in x-direction	[N/m]
t	time	[s]
T_{m01}	mean absolute wave period	[s]
U	depth averaged flow velocity in x-direction in case of a single layer system	[m/s]
u	orbital velocity in the in x-direction in case of a single layer system	[m/s]

U_m	depth averaged flow velocity in x-direction over the (lower) mud layer	[m/s]
u_m	orbital velocity in the (lower) mud layer in z-direction	[m/s]
U_w	depth averaged flow velocity in x-direction over the (upper) water layer	[m/s]
u_w	orbital velocity in the (upper) water layer in x-direction	[m/s]
w	orbital velocity in the in z-direction in case of a single layer system	[m/s]
w_m	orbital velocity in the (lower) mud layer in z-direction	[m/s]
w_w	orbital velocity in the (upper) water layer in x-direction	[m/s]
x	horizontal coordinate in direction of the transect, positive shorewards	[m]
y	horizontal coordinate, perpendicular to x	[m]
z	vertical coordinate, positive upwards	[m]

A

Derivation of the Radiation Stress for a Two Layer System

In section 2.3.3 an expression for the radiation stress in a two-layer system has been derived following the approach of Longuet-Higgins and Stewart (1964) and Motohiko and Shintani (2006). In this derivation, the schematisation was used as presented in figure 2.4. The general expression for the radiation stress can be separated into a contribution of the water layer and of the mud layer (equation (A.1)), which each can be subdivided in terms caused by different processes (terms (A.4) to (A.10)). Most of these terms can be readily derived as shown in section 2.3.3, expect for the terms (A.6), (A.7) and (A.10) (shown in cyan). The derivation of these terms is less intuitive and therefore presented in fullness in this appendix.

$$S_{xx,tot} = \overline{\int_{h_{m0}+\xi}^{h_{toto}+\zeta} (\rho u_w^2 + p_w) dz} - \int_{h_{m0}}^{h_{toto}} p_0 dz + \overline{\int_{0}^{h_{m0}+\xi} (\rho u_m^2 + p_m) dz} - \int_{h_{m0}}^{0} p_0 dz \tag{A.1}$$

separated per layer:

$$S_{xx,w} = \overline{\int_{h_{m0}+\xi}^{h_{toto}+\zeta} (\rho u_w^2 + p_w) dz} - \int_{h_{m0}}^{h_{toto}} p_0 dz = S_{xx,w}^{(1)} + S_{xx,w}^{(2)} + S_{xx,w}^{(3)} + S_{xx,w}^{(4)} \tag{A.2}$$

$$S_{xx,m} = \overline{\int_{0}^{h_{m0}+\xi} (\rho u_m^2 + p_m) dz} - \int_{h_{m0}}^{0} p_0 dz = S_{xx,m}^{(1)} + S_{xx,m}^{(2)} + S_{xx,m}^{(3)} \tag{A.3}$$

contributions to the radiation stress in the water layer:

$$S_{xx,w}^{(1)} = \overline{\int_{h_{m0}+\xi}^{h_{toto}+\zeta} \rho_w u_w^2 dz} = \int_{h_{m0}}^{h_{toto}} \rho_w \overline{u_w^2} dz \tag{A.4}$$

$$S_{xx,w}^{(2)} = \overline{\int_{h_{m0}}^{h_{toto}} p - p_0 dz} = \int_{h_{m0}}^{h_{toto}} \overline{p} - p_0 dz = \int_{h_{m0}}^{h_{toto}} -\rho \overline{w_w^2} dz \tag{A.5}$$

$$S_{xx,w}^{(3)} = \overline{\int_{h_{toto}}^{h_{toto}+\zeta} p dz} = \frac{1}{2} \rho g \overline{\zeta^2} \tag{A.6}$$

$$S_{xx,w}^{(4)} = -\overline{\int_{h_{m0}}^{h_{m0}+\xi} p dz} = -\overline{p_{\text{wave}} \xi} - \frac{1}{2} \rho_w g \overline{\xi^2} \tag{A.7}$$

contributions to the radiation stress in the mud layer:

$$S_{xx,m}^{(1)} = \overline{\int_0^{h_{m0}+\xi} \rho_m u_m^2 dz} = \int_0^{h_{m0}} \rho_m \overline{u_m^2} dz \tag{A.8}$$

$$S_{xx,m}^{(2)} = \overline{\int_0^{h_{m0}} p - p_0 dz} = \int_0^{h_{m0}} \overline{p} - p_0 dz = \int_{H_0}^{h_{m0}} -\rho \overline{w_m^2} dz \tag{A.9}$$

$$S_{xx,m}^{(3)} = \overline{\int_{h_{m0}}^{h_{m0}+\xi} p dz} = \overline{p_{\text{wave}}\xi} + \frac{1}{2}\rho_m g \overline{\xi^2} \tag{A.10}$$

The extra term $S_{xx,w}^{(4)}$ (A.7) is necessary because of the shift of the lower limit in the first term of (A.5) from the variable $h_{m0} + \xi$ to the constant h_{m0} for the ease of evaluating this integral. Because of this shift, the influence of the internal wave is not taken into account any more. The same holds for the extra term $S_{xx,m}^{(3)}$ (A.10). In this case, the upper limit in the first term of (A.3) was shifted from $h_{m0} + \xi$ to h_{m0} and the limit of the integral was reduced. The extra term $S_{xx,w}^{(3)}$ accounts for the effect of the free surface wave, as the upper limit of the integral in (A.5) was reduced from the variable $h_{tot0} + \zeta$ to the constant h_{tot0}. The derivation of these terms is performed in two steps. First, no wave motion is considered, only the influence of a change of the water level ζ and a change of the the mud layer thickness ξ. These changes are functions of time and are not in phase. Secondly, the dynamic wave pressure is considered.

In case the wave motion is neglected, the integral $\overline{\int_0^{h_{tot0}+\zeta} p dz}$ and thus the total wave pressure can be determined by equation A.11. Retaining only the non-zero terms after averaging over a wave period, the contributions in A.14 remain. The first two terms are applicable to the water layer and contribute to the terms $S_{xx,w}^{(3)}$ (A.6) and $S_{xx,w}^{(4)}$ (A.7) respectively. The third term is applicable to the mud layer and contributes to $S_{xx,m}^{(3)}$ (A.10).

$$\overline{\int_0^{h_{tot0}+\zeta} p dz} = \overline{\frac{1}{2}\rho_w g\big(h_{w0} + \zeta - \xi)^2 + \rho_w g(h_{w0} + \zeta - \xi)(h_{m0} + \xi) + \frac{1}{2}\rho_m g(h_{m0} + \xi)^2} \tag{A.11}$$

$$= \overline{\frac{1}{2}\rho_w g(h_{m0}^2 + 2h_{m0}\zeta - 2h_{w0}\xi - 2\zeta\xi + \zeta^2 + \xi^2)} + \overline{\rho_w g(h_{w0}h_{m0} + h_{m0}\xi + \zeta h_{m0} + \zeta\xi - \xi h_{m0}\xi)} + \overline{\frac{1}{2}\rho_m(h_{m0}^2 + 2h_{m0}\xi\xi^2)} \tag{A.12}$$

$$= \frac{1}{2}\rho_w g(-2\overline{\zeta\xi} + \overline{\zeta^2} + \overline{\xi^2}) + \rho_w g(\overline{\zeta\xi} - \overline{\xi^2}) + \frac{1}{2}\rho_m g\overline{\xi^2} \tag{A.13}$$

$$= \frac{1}{2}\rho_w g\overline{\zeta^2} - \frac{1}{2}\rho_w g\overline{\xi^2} + \frac{1}{2}\rho_m g\overline{\xi^2} \tag{A.14}$$

The dynamic wave pressures are for the largest part accounted for in the terms $S_{xx,w}^{(2)}$ (A.5) and $S_{xx,m}^{(2)}$ (A.9). The fluctuation of the interface, however, was not taken into account here. Assuming that the variation of the dynamic wave pressure is negligibly small over the distance of interface displacement (h_{m0} to $h_{m0} + \xi$), the dynamic wave pressures are assumed to be constant over depth and equal to the dynamic wave pressure at the interface. The resulting dynamic wave pressure integrated over the interface displacement is then $\overline{\int_{h_{m0}}^{h_{m0}+\xi} p_{\text{wave}} dz} = \overline{p_{\text{wave}}\xi}$ and is contributing negatively to $S_{xx,w}^{(4)}$ (A.7) and positively to $S_{xx,m}^{(3)}$ (A.10).

B

Deployment Schedule

As described in section 3.1, two locations have been selected for the measurements described in section 3.2. The schedule of the deployment of the different instruments at the locations near Surodadi and Bedono Bay is presented in figure B.1. A number of remarks need to be made regarding this schedule;

- The schedule as presented in figure B.1 was not determined in advance of the field campaign; the final locations for the measurements have been decided upon based on information gathered in the field and, furthermore, the schedule needed to be as flexible as possible, as the situation in the field changes from day to day;
- The deployment 10-14 November was a test deployment to get a first indication of which settings were to be used for the echosounders;
- 16-21 November was the first deployment with all instruments installed along a transect. The echosounder EA400 did not measure correctly;
- During the deployment 29 November - 3 December the seaward pole has been displaced, presumably by a fisherman. This means that part of the measurements from this pole are not useable for analysis;
- The duration of the last deployment at Surodadi was longer than the previous ones, as it was thought that the echologgers were now correctly configured. During this deployment, the battery level of the echologger EA400 was not high enough to complete the full deployment. Both echologgers were taken out halfway the deployment to read out the data and clear the memory. It was decided that it would be beneficial to increase the sampling frequency of the AA400 to be able to acquire more accurate data (resulting in the settings displayed in table 3.1). As the memory of the AA400 was only large enough for the instrument to be deployed for half a day using these adapted settings, the instrument was taken out in the morning and placed back in the afternoon during the last 3 days of the deployment.
- As already mentioned in section 3.2.3, as the ADVs were also used at other measurement locations of the BionManCO field campaign 2019, these instruments could only be deployed the last 1.5 days of the last deployment at Surodadi.

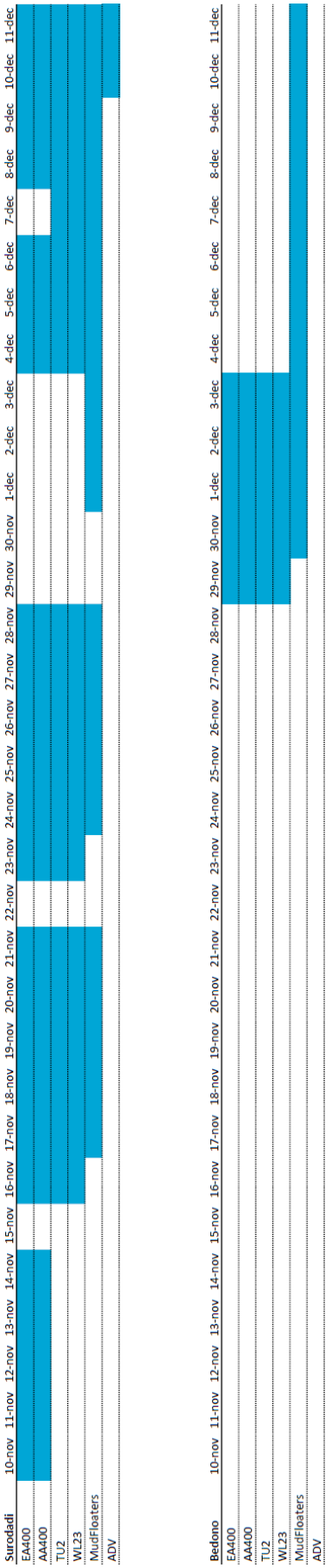

Figure B.1: Allocation of instruments between measurement locations Surodadi and Bedono Bay. **TU2** denotes the wave gauge at SW. **WL23** denotes the wave gauge at LW. **EA400** and **AA400** denote the echosounders.

C

Wave Gauges

This appendix elaborates on the calibration of the wave gauges used in the field campaign as described in section 3.2.1, as well as on the processing algorithm for the collected data.

C.1. Calibration Instruments

The type of deployed wave gauges in this field campaign was designed by the manufacturer to add a certain offset to the measured pressure levels. As the sensors cannot measure pressures close to 0 bar accurately, this offset prevents the loss of data. Before analysing the data, the offset has to be corrected, as otherwise the water depth determined from the sensor data will deviate strongly from the actual water depth in the field. This offset however differs per instrument and was not known before the field campaign. It was assumed that this offset is constant over time. Also, whilst configuring the instruments, the internal clocks had to be set by hand. This means that there is always a small time difference between the deployed instruments.

To correct for both principles, a correction deployment was conducted during the fieldwork. Both instruments were attached to a pole (figure C.1), after which this pole has been placed under water at a

Figure C.1: Waveloggers mounted for calibration. The pole to which the instruments were attached was placed on the bottom for 5 min. The water depth during this period is known. To synchronise the internal clocks of the instruments, the pole was submerged 3 times in a fast sequence.

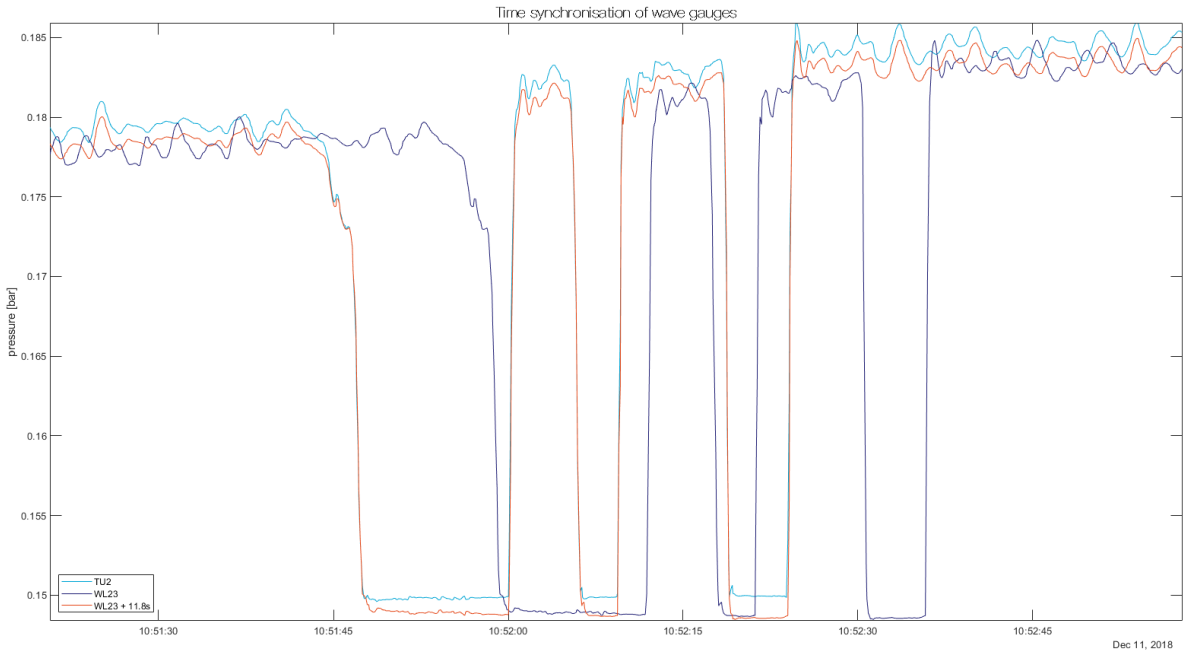

Figure C.2: Time synchronisation of the wave gauges. Instrument SW is displayed in cyan, instrument LW before time synchronisation in blue and after synchronisation (-11.8 s) in red. It must be noted, that the magnitude of the pressure of LW in this figure is artificially raised for illustrational purposes.

known height for about 5 min. This part of the signal can be used to correct for the pressure offset. To be able to synchronise the instruments, the pole was submerged 3 times in a fast sequence.

C.1.1. Time synchronisation

To synchronise the signals of the wave gauges in time, the signal of LW was fitted to SW to match up the 3 peaks in pressure. This meant a shift of the pressure signal of LW with 11.8 s (figure C.2).

C.1.2. Air pressure

Before correcting for the pressure offset (section C.1.3), the air pressure during the measurements has to be accounted for as well. The wave gauges measure the total pressure, which includes the mean air pressure and, more specifically, the variations in air pressure. The method described in section C.1.3 does account for the first, but not for the latter.

The air pressure at the measurement locations was measured by a CTD mounted at a fixed location in the base camp of the field campaign. This CTD measured the air pressure every 10 min. Before reducing the pressure signals of the wave gauges with the air pressure, the data from the CTD was smoothed with a moving average filter using four surrounding points (figure C.3).

C.1.3. Pressure offset

For both instruments the mean of the signal during the time the instruments were submerged (11 December 2018 10:54:00 - 10:59:30) was corrected to 0 bar. For SW this meant adding 0.8253 bar to the signal, for LW 0.9435 bar, still under the assumption of constant offset in time. Subsequently, the water depth measured in the field during the calibration period (converted to bars) was added to both signals, 0.316 m.

C.2. Post-Processing

The wave gauges return a time series of the pressure measured at the sensor elevation of the instrument. For the analysis of the wave climate and, in a later stage, the damping of the waves, this pressure signal needs to be converted to a time series of water surface elevation and, preferably, a

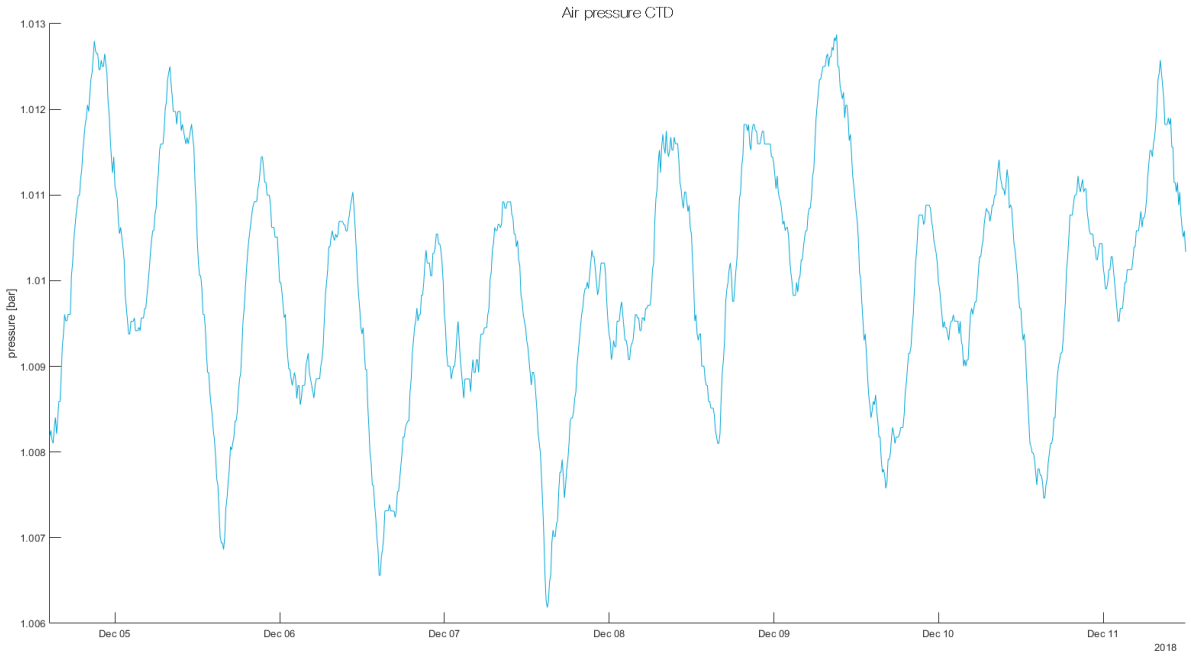

Figure C.3: Air pressure measured by a CTD at the base station of the field campaign, during the 2019-12-04 deployment at Surodadi.

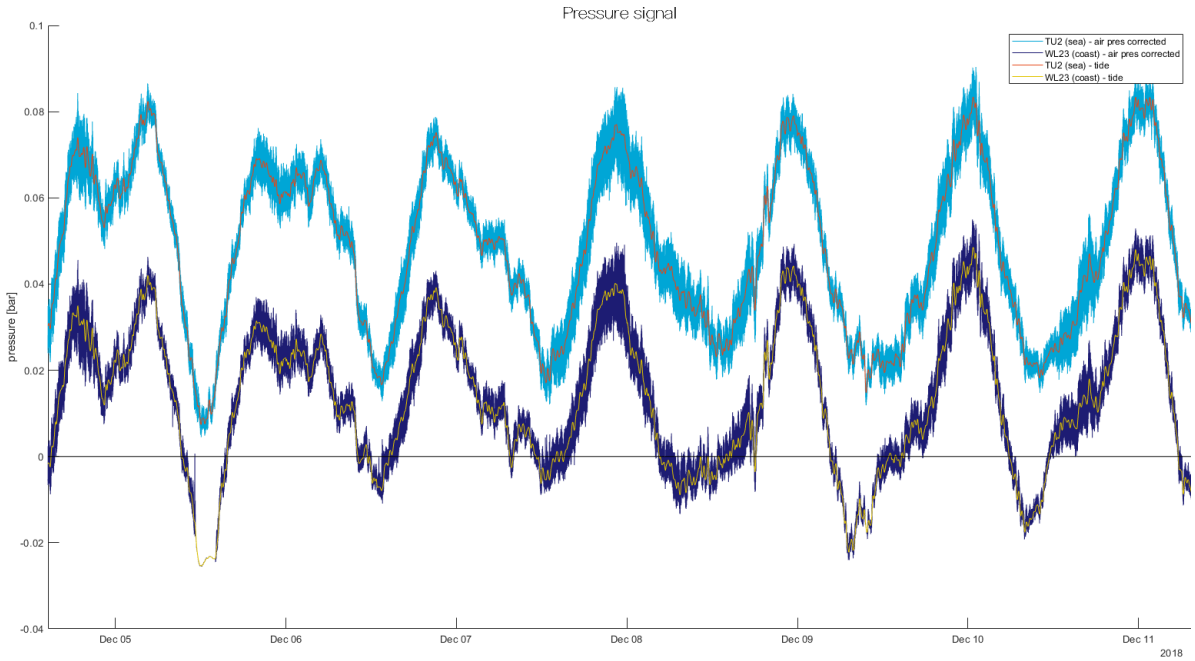

Figure C.4: Pressure measured by instruments SW and LW after correction for air pressure and pressure offset.

variance density spectrum of this same quantity. This section gives an overview of the algorithm used for this purpose.

C.2.1. Spectra

For every 2048 s interval (approximately 35 min) of the pressure signal, a variance density spectrum was calculated using the measured pressure at the level of the sensor. This variance density spectrum does not describe the variation of the water surface however, but the variation of the pressure at the level of the sensor. According to linear wave theory, the dynamic pressures caused by waves attenuate exponentially with depth. Hence, the obtained spectra from the pressure signal have to be transformed in order to represent the variation of the free surface elevation properly. This transformation matrix has been presented in (C.1).

$$T_\eta = \min\left(\frac{\cosh kz_{\text{surface}}}{\cosh kz_{\text{sensor}}}, 10\right) \tag{C.1}$$

with:

k : wavenumber [rad/m]
z_{sensor} : distance of sensor to bed [m]
z_{surface} : distance of surface elevation to bed [m]

The transformation matrix presented in (C.1) also includes a cut-off function. For the higher frequencies in the spectrum, the perturbations become lower than the sensor sensitivity. Hence, the variance density for these frequencies should become small. However, the depth attenuation increases with frequency, causing the transformation matrix to increase exponentially with frequency. The resulting spectrum will therefore blow up to infinity for the higher frequencies. Therefore, a cut-off was implemented in the transformation function, preventing the false growth of the noise at the higher frequencies. (figure C.5).

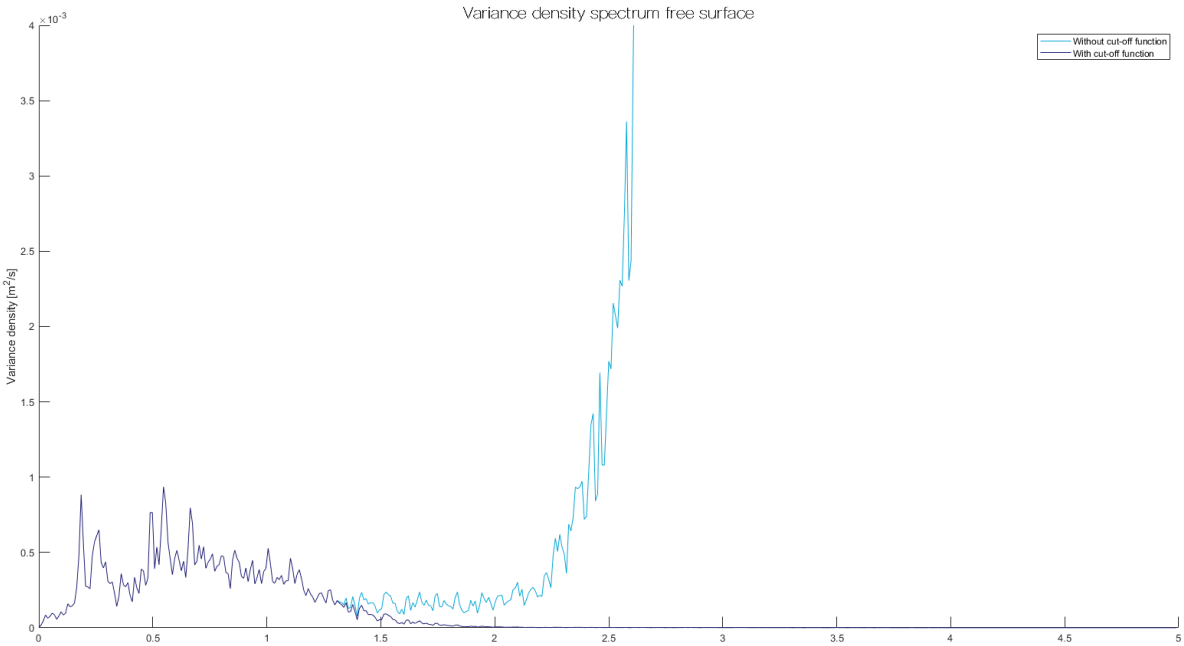

Figure C.5: Variance density spectrum for the free surface. In dark blue, the resulting spectrum is displayed in case a cut-off function is used, in cyan when this is not the case. It is clear that for higher frequencies the variance density blows-up to infinity in case a cut-off function has not been implemented.

The spectra determined from the data give expected values for the variance of the amplitude of the surface elevation for the considered frequency intervals. In case all data points in this segment of 2048 s were used, the estimate of the variance per frequency interval was only based on one realisation of the amplitude. The resulting spectrum is called the *raw spectrum*. The use of this spectrum would be acceptable if the error in the spectrum was small enough. This is generally not the case, as it is based on one realisation of a random variable. Therefore quasi-ensemble averaging was used. Each segment of 2048 s wa cut into 20 equal pieces. It was assumed that the wave conditions within these 2048 s are stationary. For each of these pieces, a variance density spectrum was determined. These estimates were then averaged to give the variance density spectrum for the full 2048 s interval. The error was therefore reduced by a factor $\sqrt{20}$, which makes the relative error with respect to the raw spectrum 22.4%. This error reduction is at the expense of the spectral resolution, which was 20 times as large as the spectral resolution of the raw spectrum. From the quasi-ensemble averaged spectra, the significant wave height H_{m0} (equation (C.2)) and the wave period T_{m01} (equation (C.3)) could be determined, which characterise the sea-states at the locations of the measurement poles.

$$H_{m_0} = 4\sqrt{m_0} \tag{C.2}$$

$$T_{m_{01}} = \frac{m_0}{m_1} \tag{C.3}$$

with:

$$m_n = \int_0^\infty f^n E(f) df$$

f : frequency [Hz]

$E(f)$: variance density [m^2/Hz] as a function of frequency

C.2.2. Shoaling Prediction

When comparing the variance density spectra at both measurement poles to assess the damping over the transect, the shoaling of waves between the two poles has to be taken into account; the waves are expected to grow over the distance between the poles due to the effect of a decreasing water depth. Therefore, the spectra obtained from the data of the seaward pole need to be corrected for this shoaling, as the damping over the distance between the poles will otherwise be underestimated. This correction can be done using a simple energy balance as shown in equation (C.4), which assumes no dissipation along the transect. In this equation, E_{SW} is the wave energy as measured at the seaward measurement pole, $E_{\text{SW,sc}}$ the estimated wave energy including shoaling, $c_{g,\text{SW}}$ is the group celerity of the waves at the seaward pole and $c_{g,\text{LW}}$ is the group celerity of the waves at the landward pole.

$$\frac{\partial E c_g}{\partial x} = 0$$

$$E_{\text{SW}}\, c_{g,\text{SW}} = E_{\text{SW,sc}}\, c_{g,\text{LW}} \tag{C.4}$$

This balance can be solved for every frequency interval in the energy density spectrum at the seaward pole, effectively converting it to the theoretical situation at the landward pole if shoaling would be the only process playing a role. The difference between the corrected spectrum and the measured spectrum will then give the dissipation over the transect.

$$\frac{H_{\text{SW}}}{h_{\text{LW}}} < 1 \tag{C.5}$$

It was assumed that this reduction in wave energy is caused by the transfer of energy to the fluid mud layer in which it is viscously dissipated. Another mechanism that could cause the dissipation of wave energy, however, is the breaking of waves. As the observed wave height is close to the water depth for a part of the dataset, it could mean that these waves are breaking due to depth. Therefore, these stretches of time were filtered out of the dataset using the rule shown in equation (C.5). This prescribes

a conservative ratio between the wave height at the seaward measurement pole (H_{SW}) and the water depth of the landward pole (h_{LW}) above which the data is filtered out. In this way, it is ensured that the dissipation analysed is not caused by the breaking of waves.

C.3. Measurements Errors

When looking at the pressure signal of LW during deployment 2019-12-04 at Surodadi, after correcting for air pressure and offset (figure C.4), it becomes apparent that during some stretches of time the pressure is less than zero. Also, when looking at the water depth during this deployment (figure C.7), it can be seen that at some moments in time the measured water depth is lower than the sensor elevation of the instrument. This is physically impossible, as the instrument can only measure water pressure when it is submerged. A possible cause of these irregularities would be a non-constant pressure offset. As only one calibration measurement was done, it is impossible to correct for an offset that is not constant. Therefore, it was chosen to still use the measurements of this instrument, but to remove all points below the sensor elevation.

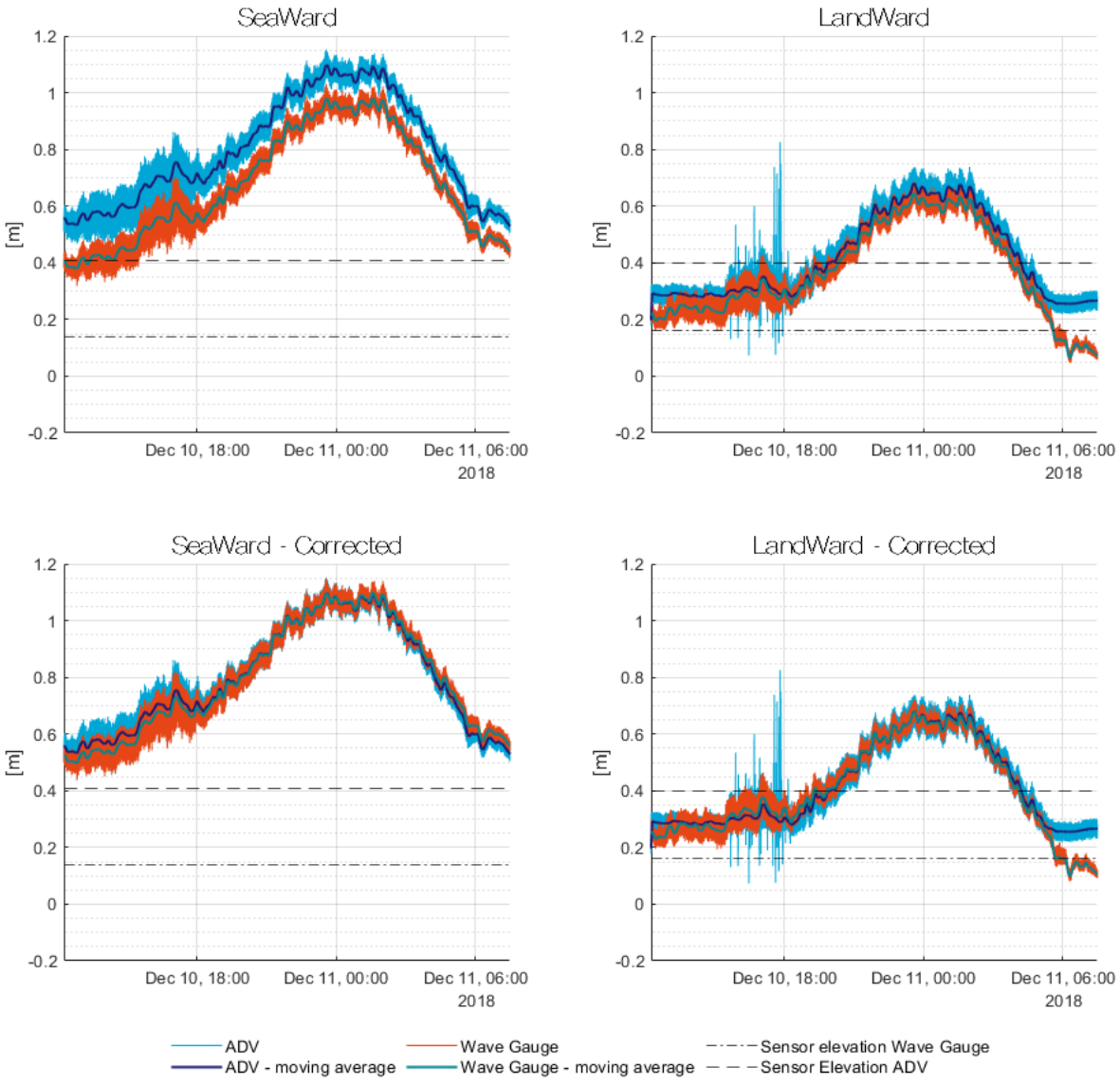

Figure C.6: Water depth measured by ADVs and wave gauges before and after correcting for the difference between the two kind of instruments.

In figure C.7 a discrepancy can be seen between the water levels manually measured at the measurement poles and the depth calculated from the wave gauge data. As this difference is of the same order of magnitude for all cases, a constant value was added to each signal to account for these differences. This value was determined from the pressure sensors in the ADVs. A similar calibration as described in section C.1 was performed on the data acquired by these sensors. This resulted in a time series of the water depth, which was compared to the time series of water depths determined from the wave gauges. The ADV data was more in line with the manually acquired water depths. Based on the comparison between the ADV data and wave gauge data, it was chosen to add 0.1185 m to the water level signal of the wave gauge at SW and 0.0342 m to the signal of the wave gauge at LW (figure C.6).

Another indication of measurement errors is the difference between the water levels at SW and LW during this deployment. As can be seen in figure C.7, the amplitude of this difference is in the order of 10 cm. Over a transect of 150 m, this value is too high to be justified by a set-up in the water level. The difference between the measured water levels, however, seems to fluctuate with the tide, which either indicates a set-up for which no apparent cause has been identify or an error in the measurements dependent on the water depth.

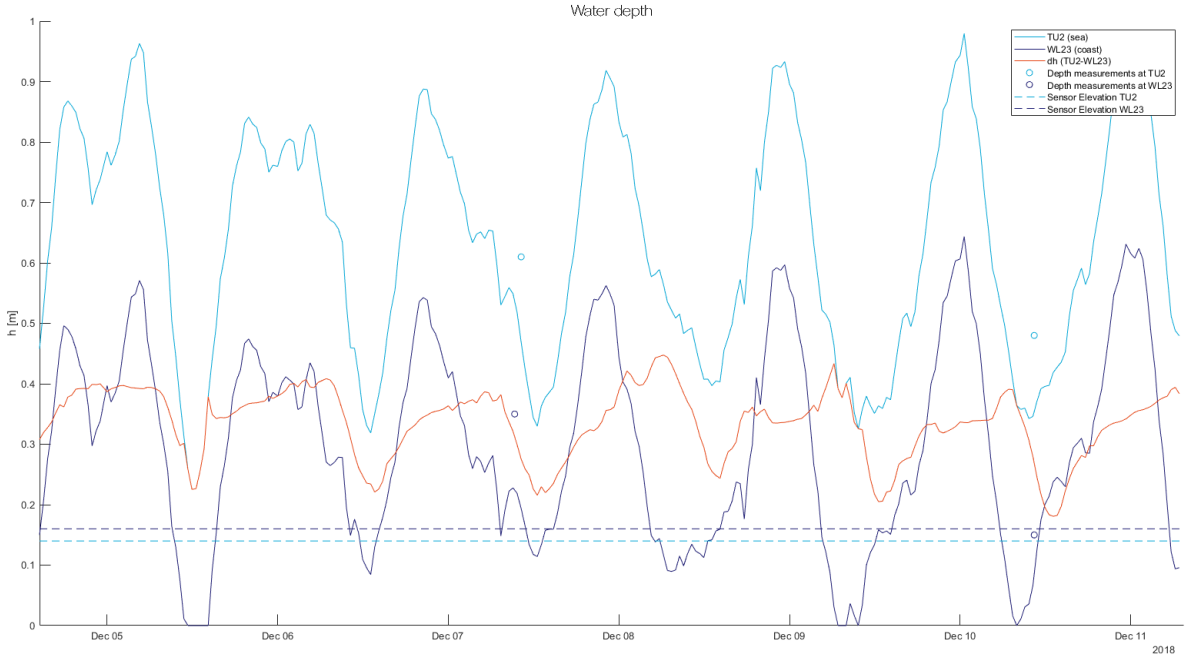

Figure C.7: Water depth calculated from the wave gauge data. The dashed lines represent the sensor elevation above the bed, the depths manually measured at the measurement poles are indicated with open circles. The red line indicate the difference in water level between the locations of the measurement poles.

D

Echosounders

The echosounders were deployed with the purpose of measuring the internal wave on the fluid mud interface, so that field conditions could be compared to the current modelling efforts. The data acquired by both instruments, however, has proven not to be useable for this purpose for multiple reasons. These reasons are explained in case of the EA400 in section D.1 and in case of the AA400 in section D.2.

D.1. EA400

Although the EA400 has the superiority over the AA400 and the acquired data (backscatter profiles) is much better suited for post-processing, due to human errors, this data cannot be used for the purpose it was acquired for. As mentioned in appendix B, the batteries in the EA400 ran out halfway through the deployment. This makes comparison with the AA400 and thus the assessment of the transformation of the internal waves difficult during most of the time of the deployment. More importantly, the sampling frequency set on the instrument appeared not to be the desired one. This was 0.1 Hz instead of 10 Hz. As the Nyquist frequency was therefore reduced from 5 Hz to 0.05 Hz, only long wave motions could be measured, which is not within the scope of this study. The data acquired by the EA400 has therefore not been further evaluated.

D.2. AA400

As explained in appendix B, the AA400 measured discontinuously throughout the deployment at Surodadi. The level of the interface is determined internally using a threshold for the measured backscatter based on the applied user settings (table 3.1). The resulting signal is very noisy and has been cleaned up by replacing the outliers by estimates based on cubic splines, using standard functions in MatLab (figure D.1). Although some, especially longer, wave forms can be observed, the quality of the data is not good enough to make a useful assessment of the internal wave motions. Also, the data was sampled at 1 Hz. This is too large to properly capture the wave motion of interest for this research. Furthermore, the corresponding Nyquist frequency became 0.5 Hz, meaning it that the full wave spectrum cannot be captured (compare with the free surface wave spectra in chapter 3; the frequencies with significantly large energy range from 0-1 Hz).

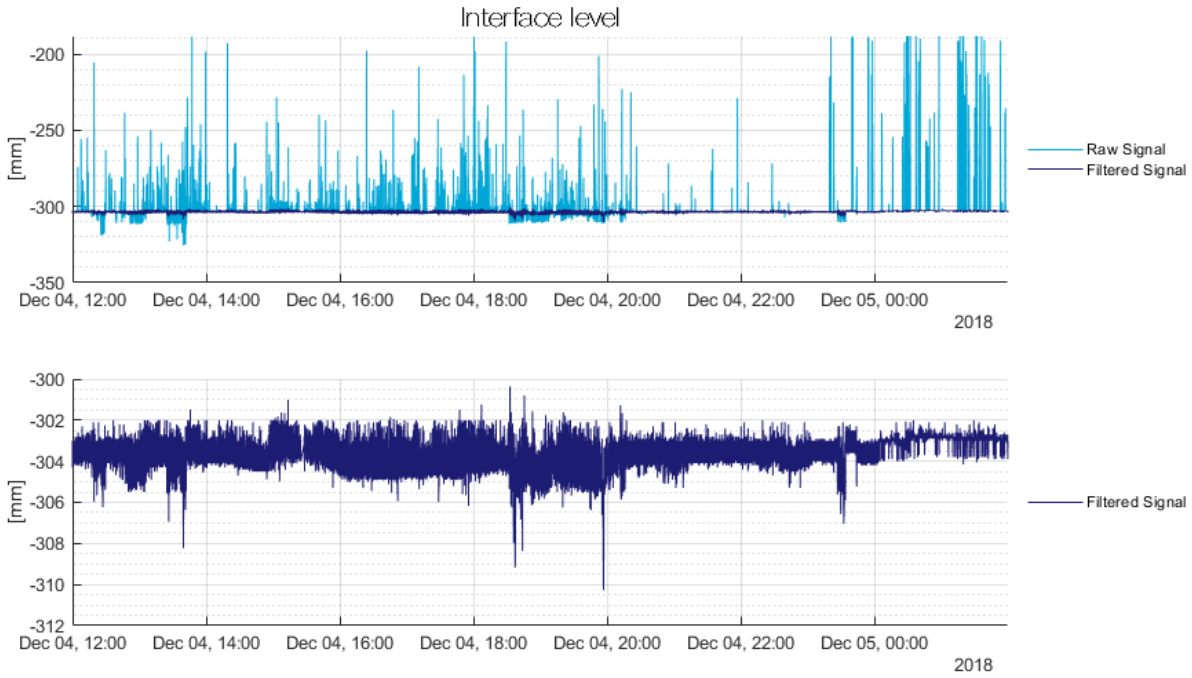

Figure D.1: Example of data acquired by the AA400. The upper panel shows the data before and after filtering, the lower panel is an enlarged view of the filtered data.